Single Photon Interferometry and Quantum Astrophysics

by

Genady Pilyavsky

A Dissertation Presented in Partial Fulfillment
of the Requirements for the Degree
Doctor of Philosophy

Approved November 2018 by the
Graduate Supervisory Committee:

Philip Mauskopf, Chair
Christopher Groppi
Nathaniel Butler
Judd Bowman
Paul Scowen

ARIZONA STATE UNIVERSITY

December 2018

ABSTRACT

This thesis contains an overview, as well as the history of optical interferometers. A new approach to interferometric measurements of stars is proposed and explored. Modern updates to the classic techniques are described along with some theoretical derivations showing why the method of single photon counting shows significant promise relative to the currently used amplitude interferometry.

Description of a modular intensity interferometer system using commercially available single-photon detectors is given. Calculations on the sensitivity and uv-plane coverage using these modules mounted on existing telescopes on Kitt Peak, Arizona is presented. Determining fundamental stellar properties is essential for testing models of stellar evolution as well as for deriving physical properties of transiting exoplanets. The proposed method shows great promise in measuring the angular size of stars. Simulations indicate that it is possible to measure stellar diameters of bright stars with AB magnitude $\leq$6 with a precision of $\geq$5% in a single night of observation.

Additionally, a description is given of a custom time-to-digital converter designed to time tag individual photons from multiple single-photon detectors with high count rate, continuous data logging, and low systematics. The instrument utilizes a tapped-delay line approach on an FPGA chip which allows for sub-clock resolution of $<$100 ps. The TDC is implemented on a Re-configurable Open Architecture Computing Hardware Revision 2 (ROACH2) board which allows for continuous data streaming and time tagging of up to 20 million events per second. The functioning prototype is currently set-up to work with up to ten independent channels. Laboratory characterization of the system, including RF, pick up and mitigation, as well as measurement of in-lab photon correlations from an incoherent light source (artificial star), are presented. Additional improvements to the TDC will also be discussed, such as improving the data transfer rate by a factor of 10 via an SDP+ Mezzanine card and

PCIe 2SFP+ 10 Gb card, as well as scaling to 64 independent channels.

Furthermore, a modified nulling interferometer with image inversion is proposed, for direct imaging of exoplanets below the canonical Rayleigh resolution limit. Image inversion interferometry relies on splitting incoming radiation from a source, either spatially rotating or reflecting the electric field from one arm of the interferometer before recombining the signals and detecting the resulting images in the two output ports with an array of high-speed single-photon detectors. Sources of incoming radiation that have cylindrical symmetry and are centered on the rotation axis will cancel in one of the output ports and add in the other output port. The ability to suppress light from a host star, as well as the ability to resolve past the Rayleigh limit, enables sensitive detection of exoplanets from a stable environment without the need for a coronagraph. The expected number of photons and the corresponding variance in the measurement for different initial contrast ratios are shown, with some first-order theoretical instrumental errors.

Lastly, preliminary results from a sizeable photometric survey are presented. This survey is used to derive bolometric flux alongside from angular size measurements and the effective stellar temperatures.

Acknowledgment

I like to think of this section as an extended author list, as multiple people throughout my life have contributed in one way or another, to the completion of this thesis. For the sake of organization, and in order to minimize the unavoidable omission of individuals, I will attempt to go in the quasi-chronological order.

None of this would have been possible without the love, support and encouragement from my family. I am grateful for bedtime stories of aliens and stars that first sparked my interest in the cosmos. Your persistent emphasis on education had led me on this path. By design or by accident, you have shaped me into the person that I am, a perfect being and one of the most humble, modest individuals on this Earth.

Post-undergraduate work and mentorship under Stephen Kane and Gerard T. van Belle convinced me to not only pursue a Ph.D. but that I may succeed. Thank you, Natalie Hinkel, for becoming my big sister, encouraging me to attend Arizona State University, and guiding me along the way. Caleb Wheeler, you have tough me plenty of valuable lessons, including the importance of putting things back, and putting things in boxes.

Thanks go out to my committee members, Judd Bowman, Nathaniel Butler, Paul Scowen, Christopher Groppi, and my advisor Philip Mauskopf. Judd, thank you for putting up with me rambling incoherently about ad-hoc ideas and Nat for proposing though provoking questions that would change my perception of the physics behind this thesis. Paul, on numerous occasions, your accessibility has steered me in the right direction and allowed me to carry forth with my project. Chirs, you wisdom assisted me in learning how research functions outside of my tiny dark room laboratory; the beer also helped. Phil, thank you for allowing me to pursue tangential ideas which often lead nowhere. While a product may not exist, the knowledge acquired during

the journey has become more valuable than success. I would also like to apologize for forcing you to spend ridiculous amounts of time correcting my spelilng and bad the grammer.

To the professors with whom I had the pleasure of taking a class, both in the School of Earth and Space Exploration, as well as the School of Electrical, Computer, and Energy Engineering, thank you. I will never be able to adequately convey the joy I experience applying the knowledge shared in the classroom, to real-world problems. Special thanks to Danielle Bliss whose classes and advising dissipated my fear of complex mathematics.

Thank you, Sam Gordon. The time spent devising weird ideas with you was pure joy. I am hopeful that in the near future we will finally figure out a way to talk to dolphins and translate dreams to video. Adrian Sinclair, thank you for mentoring me during my stay at ASU. Matthew Underhill, our morning coffee time will be forever cherished. If I had just half of your work ethic, I would have graduated in half the time. Jonathan Hoh, Cassandra Whitton, Edward Buie II, Marko best-DM-ever Neric, Kevin Hubbard, Rick Sarmento and Emily Lunde, our Tuesday Vine outing help to break up the monotony and aided in preserving my sanity.

Lastly, thank you Jordyn Fani for putting up with me for the last decade. Your love, support, and assurance helped me become a scientist and a well-rounded person. I would not have been able to do this without you.

This work has been funded by the NSF (Grant No. 1616906).

TABLE OF CONTENTS

Page

LIST OF TABLES ix

LIST OF FIGURES x

CHAPTER

1 INTRODUCTION 1

1.1 Motivations 1

1.2 Resolution, Coherence, and Interference 4

1.2.1 Spatial Resolution 5

1.2.2 Coherent and incoherent wavefront 7

1.2.3 Interference of light: classical wave formulation 9

1.3 Classical Intensity Interferometry 11

1.4 Modern Amplitude Interferometry 16

2 INTENSITY INTERFEROMETRY AND SINGLE PHOTON TIMING . 22

2.1 Intensity Interferometry with Photomultiplier Tubes 22

2.2 Intensity Interferometry with Single Photon Time Tagging 25

2.3 Choice of Detectors 28

2.4 Higher Order Correlation and Closure Phase 31

2.5 Scalability of the telescope array 33

2.6 UV-plane Exploration Due to Earths Rotation 34

3 PHOTON STATISTICS 37

3.1 Quantum of photon bunching 38

3.2 Photon Occupation Number and Coherence Time 41

3.3 Signal to Noise Ratio of Coherent, and False Positive Photons 42

3.4 Signal to noise from stellar magnitude 45

3.4.1 From Bessel calibration 45

CHAPTER Page

3.4.2 Comparing and Converting η_{occ} to Bessell Calibration for SNR Calculation 46
3.5 Signal to Noise Ratio in Higher Order Correlations 50
4 FROM THE STARS TO DATA 52
4.1 Viable Targets From the Kitt Peak Observatory 53
4.2 UV-plane Coverage from Kitt Peak 57
4.3 Time bin shift 63
4.4 Synchronization of the Decoupled Telescopes 64
4.5 Optimal Telescope Size and the Affects of Seeing 66
4.6 Telescope to SPAD coupling 67
4.7 Readout Electronics 69
5 READOUT ELECTRONICS AND DATA ANALYSIS 73
5.1 Background 73
5.2 Hardware 74
5.2.1 ROACH2 FPGA Board 74
5.2.2 LVTTL to LVDS Z-Dok Board 75
5.3 Firmware 77
5.3.1 Input filter 77
5.3.2 Delay line 79
5.3.3 Bubble filter 81
5.3.4 Encoder 81
5.3.5 Ping Pong Buffer 83
5.4 Software 84
5.5 Post-processing 85

CHAPTER Page

6 LABORATORY TESTS 88
6.1 Timing Precision 88
6.2 Optical Setup 90
6.3 RF Pickup and Modulation 93
6.4 Hammond Box and RF Shielding 96
6.5 Additional Peaks and Troughs 98
7 IMAGE INVERSION SINGLE PHOTON INTERFEROMETRY FOR EXOPLANET CHARACTERIZATION 100
7.1 General Overview 100
7.2 Background 102
7.2.1 Current Imaging Techniques 103
7.2.2 Sub-Rayleigh resolution 104
7.3 Semiclassical Explanation 106
7.3.1 Theoretical limit and total cancellation of the host star light 106
7.3.2 Coherence time and single photon detection 108
7.3.3 Associated Errors 110
7.4 Photon Loss 111
7.5 Contrast Ratio 113
8 FUTURE DEVELOPMENT 116
8.1 Image Inversion Interferometry 116
8.2 Additional signatures in the correlated dataset 118
8.3 Readout electronics for single photon detectors 119
8.3.1 ROACH2 Upgrades 119
8.3.2 Future Readout Electronics 120

CHAPTER Page

8.4 Single Photon Interferometry Array 122

REFERENCES 123

APPENDIX

A TEMPERATURE DERIVATION THROUGH SED FITTING 133

A.1 The PTI Project Overview 134

A.2 Bolometric fluxes 134

A.3 Filters and calibration stars 135

A.4 Photometric analysis 136

A.5 SED Fitting 137

A.6 Preliminary results 137

B FULL TABLE OF REFERENCE STARS USED IN THE PTI GIANTS SURVEY 139

LIST OF TABLES

Table Page

2.1 Variables use in Equation 2.6 36

3.1 Table of calibrated fluxes from $m = 0$ sources. The information within this table was obtained from McGaugh *et al.* 47

3.2 Main sequence spectral types, along with their temperature, absolute magnitude, luminosity and radii. Values obtained from Morgan. 49

4.1 Stars, according to their spectral type (top) and apparent magnitude (bottom), observable from Kitt Peak. 56

4.2 Telescopes on Kitt Peak which were used in the simulations. The latitude, longitude and elevation are presented as an offset from 31.9°, -111° and 2000 meters. 58

4.3 Alkaid (Eta Ursae Majoris) 61

4.4 Commercially Available SPAD units 69

4.5 Commercially Available TDCs Units 70

LIST OF FIGURES

Figure		Page
1.1	Resolving two emitters	6
1.2	Point spread function of fully, partially, and unresolved sources	7
1.3	Coherent and incoherent light sources	9
1.4	Classical Stellar Intensity Interferometer	14
1.5	First stellar correlation measurement of Sirius	15
1.6	Modern amplitude interferometers	18
1.7	Images of resolved stars	21
2.1	Limiting magnitude, based on telescope size, of PMTs and SPADs with filters of varying bandwidth.	29
3.1	Three dimensional parameter space of time, wavelength, and η_{occ}	44
3.2	Comparison of SNR derived with Bessel approximation and η_{occ}.	48
4.1	Limiting magnitude of a conceptual Kitt Peak interferometry array.	55
4.2	UV-plane coverage from conceptual Kitt Peak interferometry array	60
4.3	Simmulated $\Gamma^{(2)}$ of Alkaid, viewed from Kitt Peak	62
4.4	Temporal drift of the $\Gamma^{(2)}$ signal as a function of time, for different telescope pairs.	64
4.5	Scintillation affects based on the telescopes size and focal length	67
4.6	Cross talk in commercial TDC	72
5.1	ROACH2 FPGA board with a custom ZDOK connector	76
5.2	Block diagram of the TDC firmware	78
5.3	Block diagram of the input filter firmware	79
5.4	Block diagram of the CARRY4 delay line	80
5.5	Block diagram of the bubble filter	82

Figure Page

5.6 Cross-correlated signal, before and after data processing and DNL removal 87
6.1 Timing precision of the TDC 90
6.2 Optical bench setup diagram 93
6.3 Laboratory test and background noise 95
6.4 Correlated and uncorrelated datasets 97
6.5 Correlated dataset and expected signal 99
7.1 Conceptual sketch of Image Inversion Interferometry 102
7.2 Conceptual optical setup of a modified Mach-Zehnder Interferometer . . 106
7.3 Expected photon loss 112
7.4 Expected contrast ratio 115
A.1 SED fit 138

Chapter 1

INTRODUCTION

1.1 Motivations

In the ongoing efforts to understand the evolution of the universe, direct observations are necessary to accept, reject, or refine proposed theories. The topic of stellar evolution has no shortage of observables, as there are billions of stars in our galaxy alone, of varying age, size, temperature. To constrain the models of stellar evolution, direct measurements of these primary parameters are needed. Some, such as temperature, can be derived if the angular size of the star, as well as the bolometric flux, is known (See Appendix A). Others, such as age can be derived through spectral measurements and metal abundance Hinkel *et al.* (2014), although it is still a rapidly evolving field with conflicting results. Parameters such as differential rotation and obliquity in stars require measurements and analysis of the stellar diameter at different orientations. However, *the physical size of stars is not a trivial quantity to measure and constrain.*

The physical diameters of stars other than the Sun can be determined using indirect methods such as photometry with spectral fitting (Chelli *et al.*, 2014) and astroseismology (Basu *et al.*, 2010), or direct measurement of angular diameters combined with accurate measurements of distance. Angular resolution on the order of milliarcseconds (mas) to tenths of milliarcseconds is required to resolve nearby stars. While current radio interferometers such as ALMA can achieve resolution of 20-40 mas, the wavelengths at which such observations are carried out are not favorable for stars, which tend to emit most of their photons in the ultraviolet, visible and near

infrared regime of the electromagnetic spectrum.

Optical amplitude interferometers (A-Int) such as CHARA, NPOI, etc. providing measurements for giants (Baines *et al.*, 2010), main sequence A, F, G, K types (Boyajian *et al.*, 2012a,b, 2013) and exoplanet host stars (von Braun *et al.*, 2014; Ligi *et al.*, 2016). These interferometers are based on the Michelson beam-combining interferometer initially used to measure the Earth's relative motion through the "Ether" (Michelson and Morley, 1887), with a null result. This method was first applied to astronomy to measure the diameter of Betelgeuse (Michelson and Pease, 1921).

The classical approach to amplitude and intensity interferometry treat the electrical fields as classical waves, combining the fields and observing correlated changes intensity or amplitude and phase. The new approach is to digitize the fields, to a precision of a single photon, and bring astrophysics into the realm of quantum physics. Modern technological advancements such as single-photon detectors (SPDs) and time to digital converters (TDCs) have made the Intensity Interferometry (I-Int) method once again appealing by offering higher measurement sensitivity with potentially simpler instrumentation.

The SPDs are capable of achieving unprecedented timing resolution on the order of tens of picoseconds and very little instrumentation noise. Single photon avalanche diode (SPAD) detectors are optimized to work in the optical regime (400-1000 nm), whereas superconducting nanowire single-photon detectors (SNSPD) can function from UV to NIR with about a factor of 10 improvement in timing resolution (Bronzi *et al.*, 2016; Cova *et al.*, 1981; Verma *et al.*, 2015; Semenov *et al.*, 2001a; Gol'tsman *et al.*, 2001).

The TDCs enable the arriving photons to be time-stamped, relative to a common reference. The signals can thus be cross-correlated using software post-data acquisition. Therefore, one of the most significant advantages of modern I-Int is that it

does not require telescopes to be physically linked. Lack of optical cables means that additional telescopes in the array do not complicate the setup, the separation between the telescopes can be arbitrarily large, and in turn provide higher angular resolution with longer baselines than what is currently achievable.

A better angular resolution would allow astronomers to expand their understanding of stars. With the higher angular resolution, surface features governed by the convection could be examined. The ability to resolve stellar winds around the stars provides a more in-depth understanding into radiative processes. Rotational velocities, obtained by measuring the obliquity of the star, would allow for removal of Doppler broadening from the stellar spectrum. High precision measurements of the angular size can be used with bolometric flux to determine the effective temperature of these objects (Appendix A).

Unfortunately, current angular resolution limits on what astrophysical bodies astronomers can observe, such as degenerate stars. It should be possible to measure the size of the white dwarfs, which has yet to be directly measured. The diameter of white dwarfs is theorized to be slightly larger than Earths (Shipman, 1979), which would require an optical telescope with a diameter on the order of kilometers. A dedicated telescope array will need to be constructed, because these objects tend to be dim with magnitudes of ~ 12 and fainter.

In principle, the diameter of neutron stars can also be measured but would require angular resolution which can only be obtained with telescopes separated by hundreds to thousands of kilometers. Furthermore, their brightness magnitude at optical wavelengths is $\sim$25 and dimmer and would require 30-meter class telescopes.

Direct measurement of the size of the black hole accretion disk, around Sagittarius A would provide a significant amount of data to deepen our understanding of the event horizon. Although other projects such as the Event Horizon Telescope (EHT) (Ricarte

and Dexter, 2014) are attempting to do this, the wavelengths are in the radio portion (mm) of the spectrum. Since spatial resolution is tied to the observational wavelength, an optical counterpart would be beneficial to examine finer, hotter structure, closer to the event horizon.

1.2 Resolution, Coherence, and Interference

Before moving on much further, it is vital to address the issues which drive the astronomers to build large optical telescopes. While the discussion and derivations are simplified, their purpose is to establish some "classical " understanding of the wave nature of light. The more complex quantum concepts, such as single-photon interference, are discussed in Chapter 3.

Let us begin by envisioning a single sphere in space, illuminating uniformly in every direction, i.e., isotropically, but in the far field such that the waves are planar by the time they arrive to the telescopes. Additionally, let us assume that the light is monochromatic and is of singular polarization. The planar electromagnetic field E can then described as

$$E = ae^{-i(kr-\omega t+\phi)}, \tag{1.1}$$

ranging in value from -a to +a in an oscillatory fashion, containing real and imaginary components. The position vector r represents the location in the x, y, and z coordinate. Constant a is referred to as the modulus, vector k representing the wave number ($k = \frac{2\pi}{\lambda}$) with λ being the wavelength of the wave. The angular frequency for the light is $\omega = 2\pi\nu$ with ν representing the standard frequency component, t variable used as a stand-in for time. The phase of the wave, ϕ, represents the instantaneous position in time of the wave's cycle, and as we will shortly see, is the parameter which enables waves to "interfere" with one another constructively and destructively.

1.2.1 Spatial Resolution

To describe spatial resolution, let us introduce a second object, and place it at some distance R from the first. As shown in Figure 1.1, the two objects on the two-dimensional plane emit light outward; a conical emission is shown as supposed to the actual circular [1] for clarity. As the waves propagate further from the source, their radius of curvature increases to ∞; That is to say that for a constant unit of length perpendicular the direction of propagation, the wavefront changes from an arced to planar. At a certain distance (D) from the two objects, an observer is no longer able to distinguish between the two sources and they are said to be unresolved.

This spatial location is set by the separation between the two sources (R) and their distance (D) to the aperture of radius r, as well as the wavelength:

$$\frac{1.22\lambda}{2r} = \frac{R}{D}. \tag{1.2}$$

This equation is defined as the Rayleigh criterion, and the constant value of 1.22 comes from the derivation of the Airy function, where the first dark spot (minima) occurs; the reasoning behind the dark/light fringes are due to the path-length difference between two incident waves. The constructive fringes occur when the path length difference is equal to a multiple of π. Conversely, the dark fringes are created due to destructive interference, with path-lengths equaling to multiples of $\pi/2$.

The ratio of R to D is called "angular size", which is in units of radian along a single dimension. When the left-hand side of Equation 1.2 is greater than the right-hand side, the objects will be resolved. Inversely, when the right-hand side is greater, the objects will not be resolved, no distinction can be made as the photons emitted from them occupy the same "spatial mode". A three-dimensional case (x, y, and

[1] or spherical, in a three-dimensional case

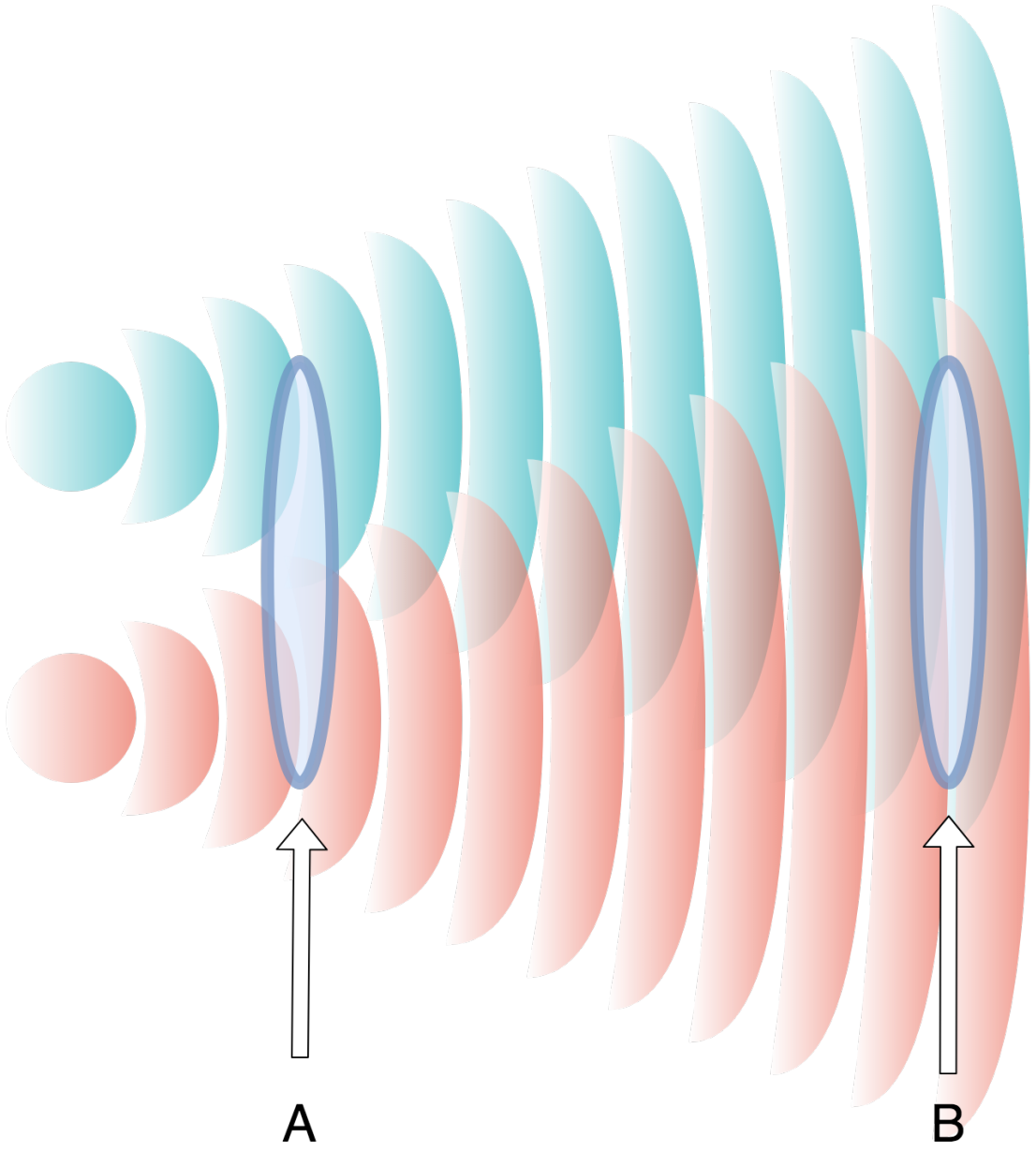

Figure 1.1: Two emitters (aqua and red) produce planer waves (for clarity). At distance "A", the sources are resolved with an aperture (blue). At the distance "B", the sources are no longer resolved by the same size aperture; the two wavefronts are indistinguishable from one another.

brightness) of the two objects in resolved, partially resolved, and unresolved cases are shown in Figure 1.2.

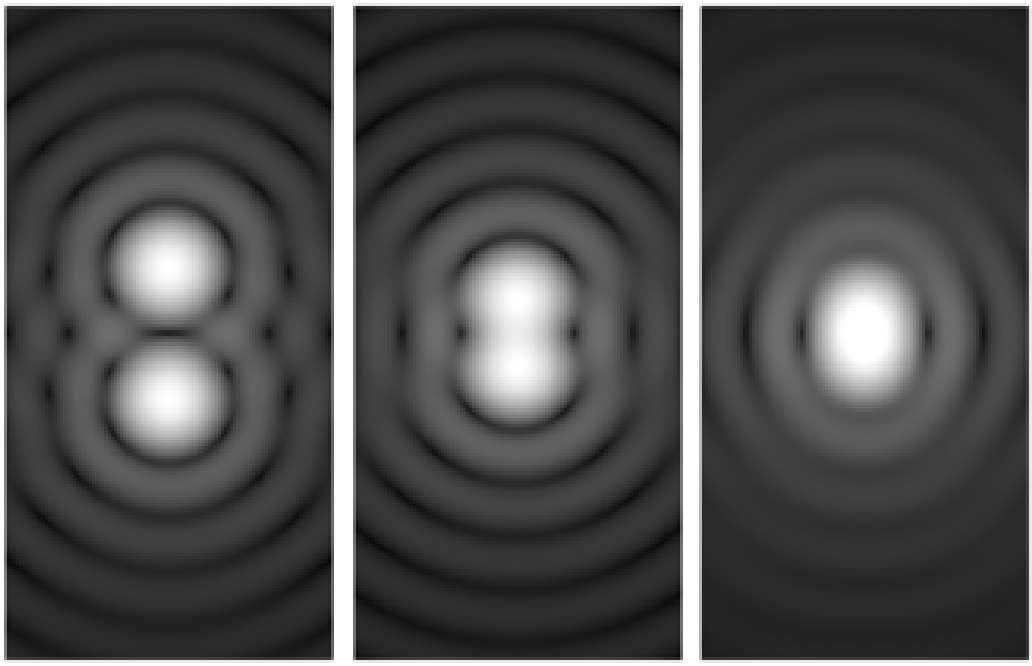

Figure 1.2: Three cases of two sources at different separation is shown in the three frames. First, the two objects are fully resolved since the first minima of their point spread function are not superimposed. Second image shows the two objects closer to one another, and third frame demonstrates nearly perfect superposition of the two, at which point it becomes unclear if it is one or two objects.(Bliven (2014)).

1.2.2 Coherent and incoherent wavefront

The distinction between the two states needs to be established to understand the constructive and destructive cases of interference. The wavefront can be thought of as a group, a collection, of photons. In a coherent field, photons all occupy the same

state. The waves transverse "in phase", such that the instantaneous value of ϕ from Equation 1.1 is the same for all the photons; the waves also need to be in an aligned along the direction of propagation, such that their phases relative to one another remain constant. A single photon, quantum approach to describing this process is discussed in Chapter 3, Section 3.1.

If the waves are of different frequencies, or temporally modulated, the light will be coherent for a short period, since the waves will come to and out of phase alignment as they transverse. If the light waves are all identical in frequency, the duration for which the coherence will be maintained is longer. The coherence time τ_c is inversely proportional to the bandwidth of the light,

$$\tau_c = \frac{1}{\Delta\nu}, \tag{1.3}$$

since the waves are essentially creating a beat frequency amongst themselves.

Lasers, as an example, are almost perfectly coherent sources. The coherence is due, in part, to a very narrow spectral bandwidth of the devices, which ensures that the traveling photons are of almost identical wavelength, and the coherence is maintained in time and space. A narrow band thermal source could be coherent if the mechanism driving the photon emission is correlated. If the photon generation mechanism is random, then partial coherence *from an incoherent source* can be established at a certain point in space assuming that the wavefronts *arriving* to said point, are planar due to the emitter being in the far field of the optical system. This description is referred to as the Van Cittert-Zernike theorem (van Cittert, 1934; Zernike, 1938)

On the other hand, an incoherent light will be a superposition of waves with random phases. Such is the case, under normal conditions, with the broadband and isotropic emitters, as shown in Figure 1.3. With different wavelengths superimposed on one another, the waves go in and out of phase. Furthermore, being emitted at

different angles, spatial alignment occurs on short timescales. These effects can be mitigated somewhat by narrowing the bandwidth, with the introduction of an optical filter. The spatial alignment, where the path-length difference between the different surface parts of the emitter and the detectors allows for in-phase wavefront arrival can be achieved by moving the sources further away or observing a source that is already far away. As previously discussed, the waves from an unresolved source are planer, arriving with a similar if not identical phase. Because of this, it is possible to measure just to what degree the stars, fundamentally chaotic and incoherent sources, become locally coherent. The degree of coherence is set by their angular size and the spatial resolution capabilities of the telescope.

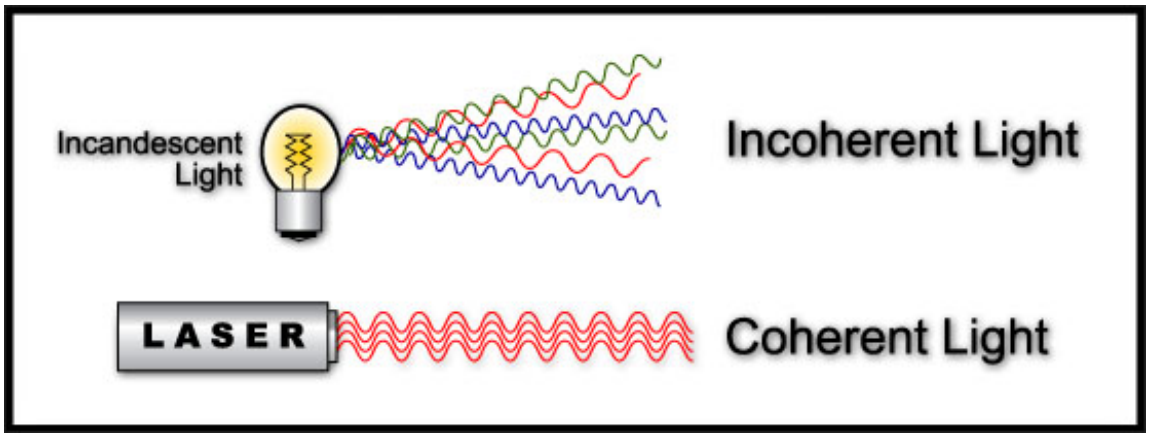

Figure 1.3: Example image, obtained from Ngeyaabwe (2014) for an incoherent, chromatic light-sources such as an incandescent lightbulb or a star and a coherent, monochromatic laser, with simplified illustration of wave propagation.

1.2.3 Interference of light: classical wave formulation

Let us revisit the case of two emitters setup in Section 1.2.1. As previously mentioned, two things need to occur to establish coherence, spatial alignment and

narrow band. Postulating that the waves from source A_1 and A_2 are observed with a narrow band filter, and the sources are unresolved, two sets of equations describing the electromagnetic waves are

$$\begin{aligned} A_1 &= a_1 e^{-i(kx_1 - \omega t + \phi_1)} \\ A_2 &= a_2 e^{-i(kx_2 - \omega t + \phi_2)} \end{aligned} \tag{1.4}$$

The power measured with the photodetectors is proportional to the intensity I, which is a time average of the amplitude and its complex conjugate $\langle AA^* \rangle$. If the two fields are aligned in space, such that $x_1 = x_2 = x$, the average intensity $\langle I \rangle$ measured can be described as

$$\begin{aligned} \langle I \rangle &= (A_1 + A_2)(A_1 + A_2)^* \\ &= A_1 A_1^* + A_2 A_2^* + A_1 A_2^* + A_2 A_1^*. \end{aligned} \tag{1.5}$$

The last two terms $A_1 A_2^*$ and $A_2 A_1^*$ are analogues, and for simplicity lets assume that the two amplitudes are equal, $A_1 = A_2 = A \rightarrow I_1 = I_2 = I$. Combining them, and rewriting Equation 1.5 in the long form, we see that

$$\begin{aligned} \langle I \rangle &= I_1 + I_2 + 2A_1 A_2 e^{-i(kx - \omega t + \phi_1 - \phi_2)} \\ &= 2I + 2I e^{-i(kx - \omega t + \phi_1 - \phi_2)}. \end{aligned} \tag{1.6}$$

The only variables in Equation 1.6 that are of interests are the phase components of the two waves, ϕ_1 and ϕ_2. We can examine three different scenarios, and we will start with the case where $\phi_1 = \phi_2 = 0$. With this assumption, the complex value of the exponential is $e^{-i(0)} = 1$. The solution to Equation 1.6 becomes $\langle I \rangle = 2I + 2I$, and the measured intensity is a factor of 2 greater, relative to what is emitted by each source independently! This case is called constructive interference, producing

the bright fringes in Figure 1.2. At first glance, it would appear as though well-established rules of physics were violated, as there is an imbalance of observed power measured. To restore the balance, let us examine another case.

If the two incident waves are out of phase by half the cycle π, such that $\phi_1 = 0$ and $\phi_2 = \pi$, the complex exponential of $e^{i(-\pi)} = -1$. Under this condition, the solution to Equation 1.6 is $\langle I \rangle = 0$, meaning that the electric field measured is 0. This result corresponds to the dark fringes in Figure 1.2. The imbalance set by the previous case is rectified, and everything becomes well again in the realm of physics.

The last case, while less dramatic but necessary to examine, is when they are $\frac{\pi}{2}$ (90°) out of phase. The value of $e^{i(\pm\pi/2)}$ is $\pm i$, which yields a complex value without a real component. Since we are unable to measure the complex components with power detectors, the solution to Equation 1.6 becomes $\langle I \rangle = 2I$, power equivalent to the summation of the irradiated power from the two sources.

The description presented in this section is of classical, wave nature approach. A more in-depth, quantum-based analysis is shown in Chapter 3. Nevertheless, with an established description of how wavefront can interact with one another, we can move on to exploring the history and evolution of optical interferometers and their application in astrophysics.

1.3 Classical Intensity Interferometry

Interferometric measurements of stellar objects at optical wavelengths began in 1921 with Albert A. Michelson measuring the diameter of α-Orionis (Michelson and Pease, 1921), commonly known as supergiant star Betelgeuse. This accomplishment was achieved when he applied the principals developed during his Michelson Morley experiment (Michelson and Morley, 1887) to self-interfere the electric field collected from different parts of a telescope mirror. This results of the experiment have demon-

strated that, in principle, segmented apertures can be combined to form a whole; this approach later became known as aperture synthesis and is widely used at radio frequencies, for scientific experiments as well as commercial applications. While not indeed intensity interferometry, but rather amplitude interferometry, where individual photons self-interfered, this experiment paved the way for future developments in the field of optical stellar interferometers.

The next step in the evolution of optical interferometry came thirty years later when Hanbury Brown and Twiss (Brown and Twiss, 1956b) performed an in-lab demonstration of a zero point, second-order correlation with two detectors. A mercury arc lamp was used to illuminate a *rectangular* aperture, and split via a beam splitter. The light from two arms of the interferometer illuminated two different photomultiplier tubes (PMT). The detectors were thus superimposed in 1) Time, given that the path-length between them was identical and 2) Space, since the incident photons came from a single spatial mode. The output from the PMTs was amplified and passed to a correlation. As the electric field produced by the source fluctuated, temporal correlations between the power output of the PMTs were observed. This effect can be described mathematically by examining the two electric fields that are incident on the detectors and comparing the expectation value of an individual field to the combined one.

For example, while the source may, on average, produce 100 photons per second, the distribution is not uniform; at any given second, the number of observed photons with a perfect detector can vary such that 100 ± 10 photons are observed. The average count-rate is a Poisson distribution which approaches a Gaussian distribution in the limit of large numbers. The average count-rate is better modeled as a Gaussian distribution, with the mean value of X and a standard deviation of $X^{0.5}$, in arbitrary units of power or number of photons. The second order correlation function gives the

ratio of the joint expectation value of the intensities converted to power relative to the expectation value from the individual contributions, $\gamma^{(2)}_{1,2}$, as

$$\begin{aligned}
\gamma^{(2)}_{1,2} &= \frac{\langle I_1 I_2 \rangle}{\langle I_1 \rangle \langle I_2 \rangle} \\
&= \frac{\langle (I_1 + \delta I_1)(I_2 + \delta I_2) \rangle}{\langle I_1 + \delta I_1 \rangle \langle I_2 + \delta I_2 \rangle} \\
&= \frac{\langle I_1 I_2 + \cancelto{0}{I_1 \delta I_2} + \cancelto{0}{I_2 \delta I_1} + \delta I_1 \delta I_2 \rangle}{\langle I_1 \rangle \langle I_2 \rangle} \\
&= 1 + \frac{\langle \delta I_1 \delta I_2 \rangle}{\langle I_1 \rangle \langle I_2 \rangle} \\
&= 1 + \Gamma^{(2)}_{1,2}.
\end{aligned} \tag{1.7}$$

Since the average value of δI is zero, the two middle terms cancel. It is also evident from Equation 1.7 that if the variation in the intensities, δI_1 and δI_2 are uncorrelated, the product of the two terms is zero. On the other hand, when the variations are correlated, $\Gamma^{(2)}_{1,2} \neq 0$, and an "excess" intensity is measured. The term $\Gamma^{(2)}_{1,2}$ is normalized by the expected value from the uncorrelated signal, such that $0 \leq \Gamma^{(2)}_{1,2} \leq 1$.

The value of $\gamma^{(2)}$ is precisely what Hanbury Brown and Twiss were able to measure in the laboratory setting. Equation 1.7 can also be rewritten classically, in terms of the electric fields as

$$\begin{aligned}
\gamma^{(2)}_{1,2} &= \frac{\langle E_1 E_1^* \rangle \langle E_2 E_2^* \rangle + \langle E_1 E_2^* \rangle \langle E_1^* E_2 \rangle}{\langle E_1 E_1^* \rangle \langle E_2 E_2^* \rangle} \\
&= 1 + \frac{|\langle E_1 E_2^* \rangle|^2}{\langle |E_1|^2 \rangle \langle |E_2|^2 \rangle},
\end{aligned} \tag{1.8}$$

and will become of importance in Section 1.4.

Because the measured quantity is obtained from the intensity, the phase information not retained and image reconstruction is not possible without making some

assumptions about the object under the observation. Nevertheless, information regarding the size of the object is retained, and the physical size can be derived assuming adequate precision is obtained, the distance is known, as well as the telescope separation; derived in Equation 1.2.

Experiments on the sky were performed after the construction of the Narrabri Stellar Intensity Interferometer located in Narrabri, Australia. Albeit no longer in use, it was monumental to developments of intensity interferometry. The interferometer was composed of two $\sim$7 meters, segmented mirror telescopes. The telescopes were mounted on trucks and placed on a circular track which allowed the separation between the telescopes to vary from 10 to 188 meters, as shown in Figure 1.4.

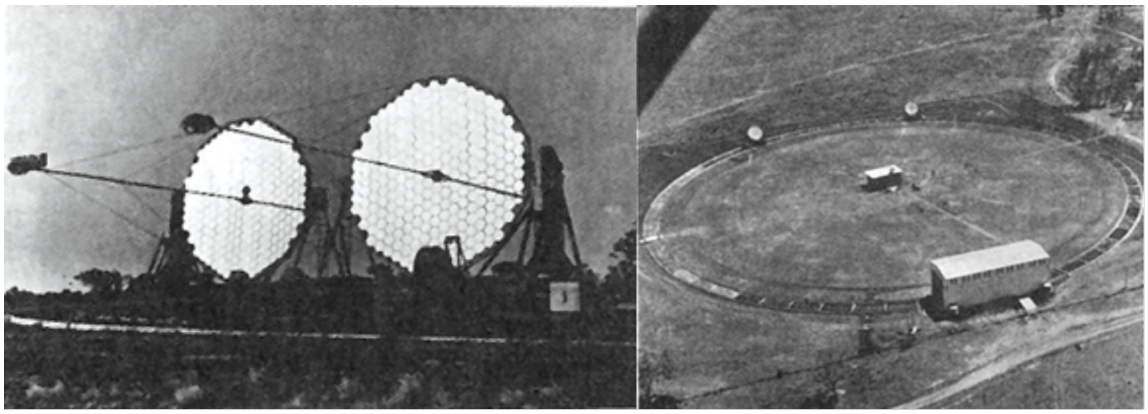

Figure 1.4: Narrabri Stellar Intensity Interferometer created by Hanburry Brown and Twiss. The telescopes (left) are made of segmented mirrors, with PMTs attached at the focal points, eliminating the need for a secondary reflector. Two telescopes are placed on a track (right, aerial view) in order to control the separation between the pair. Image obtained from Padula (2005).

The first star measured by Hanbury Brown and Twiss was Sirius (Brown and Twiss, 1956a), not surprising since it is the brightest exo-solar object at optical wave-

lengths. Four measurements were obtained at different baselines, with about 3 to 6 hours of integration time dedicated to each data point. The results, shown in Figure 1.5, were used to constrain the angular diameter of Sirius to 6.3 mas, with an error of about 10%, and close to the currently accepted value of 6.04 mas (Davis *et al.*, 2011).

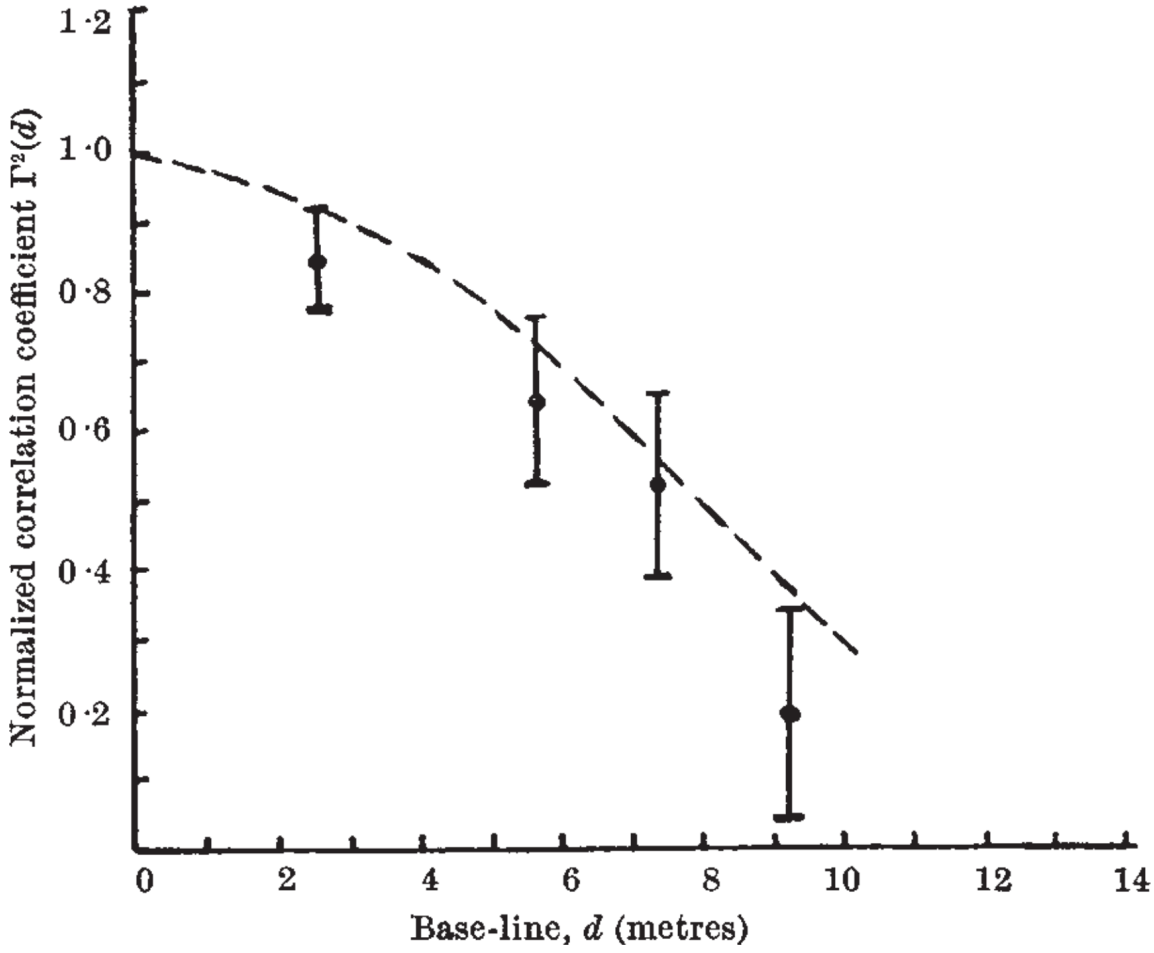

Figure 1.5: Measurement of the second order correlation function $\Gamma^{(2)} = \gamma^{(2)} - 1$ as a function of separation between the telescopes (d). Each point was obtained over a course of $\sim$8 hours. This is the first measurement of its type, obtained by Hanburry Brown and Twiss Brown and Twiss (1956a)

With the intensity interferometry concept demonstrated on a star, Hanbury Brown and Twiss set out a survey mission. Throughout the next few years, Hanbury Brown was able to measure the angular size of 32 different stars (Hanbury Brown *et al.*, 1974) successfully. This contribution has not only added to our knowledge and understanding of stars, contributing to stellar models, but also set up the foundation upon which modern intensity-single photon interferometers are being built. However, the path forward was not straight, and a detour of a few decades was made in favor of an "analog" technique, amplitude interferometry.

1.4 Modern Amplitude Interferometry

The fundamental advantages of amplitude interferometry, compared to intensity interferometry, are two-fold. First, the signal to noise is significantly higher given the same integration time and photon collecting area. The secondary advantage is *phase* information is retained, which allows for the direct conversion of amplitude/phase measurement in Fourier space, to an image. However, this method does come with its limitations. The current limiting stellar magnitude at optical wavelengths is $\sim$6. Monnier (2003) elaborates on the numerous problems in modern amplitude interferometry, with the biggest culprit being the numerous optical elements that are necessary, which significantly lowers the photon throughput.

While the intensity measurement looks for correlations in the fluctuations of the electrical field, the amplitude interferometer coherently combines the light from two or more arms of the interferometer before the detection. The telescopes are position such that their separation is on the order of hundreds of meters, and vacuums tubes or fiberoptic cables "funnel" the light towards the central location where recombination occurs, followed by detection and measurement.

Amplitude interferometry introduces the path-length difference between the arms

of the interferometer such that a photon can *self-interfere*. In the classical intensity interferometry, such an event would not contribute to the correlations in the electrical fields between the two detectors. However, in an amplitude interferometer, statistics could be built up over time, and an interferogram will emerge as one would expect in a double slit experiment where a single photon source is used as an illuminator. Therefore, amplitude interferometry allows for a higher incident photon utilization which contributes to a higher signal to noise ratio. Given that the path length is controlled to a fraction of a wavelength, $\sim$ 10s of nanometers; phase information is also retained since fringe are directly observed.

New technological developments during the 1970's in hardware/software and techniques, which allowed fringe tracking, digital signal processing, high precision path length control, made amplitude interferometry a preferred method for direct measurements of stellar objects angular size. An image and a schematic of the two largest, regarding angular resolution, modern optical amplitude interferometers are shown in Figure 1.6.

The basic mathematical principals have already been derived in Section 1.2.3. The light from each telescope (N) is split into (N-1) beams and recombined at a central location with beam splitters. This configuration allows for the fields to add. The intensity is then measured, while small path-length changes are introduced to vary the phase. Phase variations allow for measurements of not only a sum of the two intensities, but their also their cross product, which is an additional component of the constructive, destructive, and partial interference. By combining the complex amplitudes prior to detection, the *first* order coherence function $\gamma^{(1)}_{1,2}$ can be obtained since

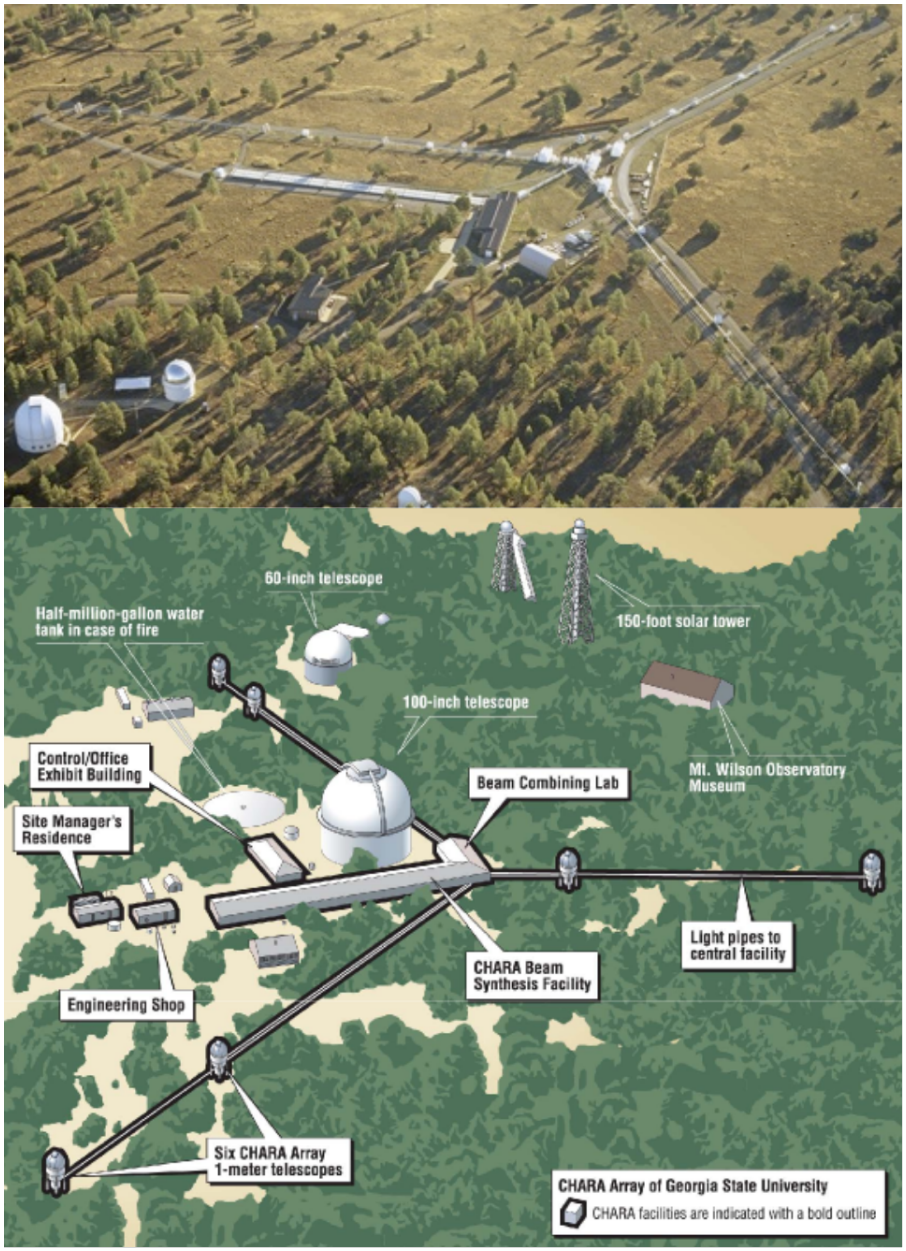

Figure 1.6: Top: Arial view of the NPOI, with baselines spanning 600+ meters. Bottom: Schematic view of CHARA interferometer, with the facilities and components labeled. Top image obtained from Wikipedia, uploaded by spaceblanket (2009). Bottom was obtained from the CHARA website, Monnier.

$$\gamma_{1,2}^{(1)} = \frac{\langle E_1 E_2^* \rangle}{\sqrt{\langle E_1 E_1^* \rangle \langle E_2 E_2^* \rangle}} \tag{1.9}$$

In the normalized form, $\Gamma_{1,2}^{(1)}$ represents the constructive and destructive interference, with the range of values of $-1 \leq \Gamma_{1,2}^{(1)} \leq 1$. If we recall Equation 1.8, it becomes evident that the normalized value of the second order correlation function $\Gamma_{1,2}^{(2)}$ is just $|\Gamma_{1,2}^{(1)}|^2$.

Alternatively, the constructive and destructive interference can be represented as complex visibility (V):

$$V = \frac{I_{max} - I_{min}}{I_{max} + I_{min}}. \tag{1.10}$$

Labeyrie *et al.* (2006) expands upon the concept described in Equation 1.6, writing the time-averaged intensity field as

$$I = I_1 + I_2 + 2E_1 E_2 \cos\big(\Delta\phi\big) |\gamma_{1,2}^{(1)}|, \tag{1.11}$$

where $\Delta\phi$ is the phase difference and $\gamma_{1,2}^{(1)}$ is the degree of coherence. Inserting these relationships into Equation 1.10 with appropriate $\pm 2E_1 E_2 \cos\big(\Delta\phi\big) |\gamma_{1,2}^{(1)}|$ for the max and min values, we obtain

$$\begin{aligned} V =& \frac{2E_1 E_2}{E_1 E_1 + E_2 E_2} |\gamma_{1,2}^{(1)}| \\ =& \frac{2\sqrt{I_1 I_2}}{I_1 + I_2} |\gamma_{1,2}^{(1)}|. \end{aligned} \tag{1.12}$$

If the two intensities are the same, Equation 1.12 informs us that the complex visibility is equal to the magnitude of the coherence function.

In order to make an accurate measurement, the path-length between the two arms will need to be varied by a fraction of a wavelength, before the path-length in the atmosphere changes, which occurs on millisecond timescales; It is possible to integrate for an extended period, assuming that the closure phase has been obtained

(See Chapter 2.4). Although the stringent requirement makes it a challenging measurement, amplitude interferometry was a worthy pursuit as it comes with additional benefits than Hanbury Brown and Twiss could not access.

In the case of the first order correlation, the information from the preserved phase allows for image reconstruction, as well as higher signal to noise ratio throughout the same integration time. With this technique, the CHARA interferometer has been successful at reconstructing image of Regulus (Che *et al.*, 2011), Rasalhague (Zhao *et al.*, 2009), Altair (Monnier *et al.*, 2007), Alderamin (Zhao *et al.*, 2009), and Beta Cas (Che *et al.*, 2011), shown in Figure 1.7. Such images allow astronomers to expand understanding of stellar evolution through examining stellar oblateness, rotational speeds, temperature and convection/radiative processes that are responsible for stellar surface structure and features.

However, even with the modern equipment, Amplitude Interferometry has its drawbacks. In order for the telescope array to function, the coherence of the individual beams collimated at the telescopes needs to be preserved as the light is passed to the central control building where interference can occur. The alignment, which needs to be on the order of $\lambda/10$ or better, is difficult to maintain. The issue arises from small temperature fluctuations along the optical path which can induce nano-scale changes in the difference of distance transversed by the two beams. Additionally, atmosphere scintillation will also vary the path-length between the top of the earth atmosphere, and the telescopes on the ground. The variability in the atmosphere is on the order of kHz or "few hundredths to a few tenths of a second" (Osborn *et al.*, 2015), and varies depending on the telescope location as well as the distance of the object from the zenith. This effect means that during a $\sim$10 millisecond time window, a calibration AND integration needs to occur.

Furthermore, the scalability of an Amplitude interferometer array with an intro-

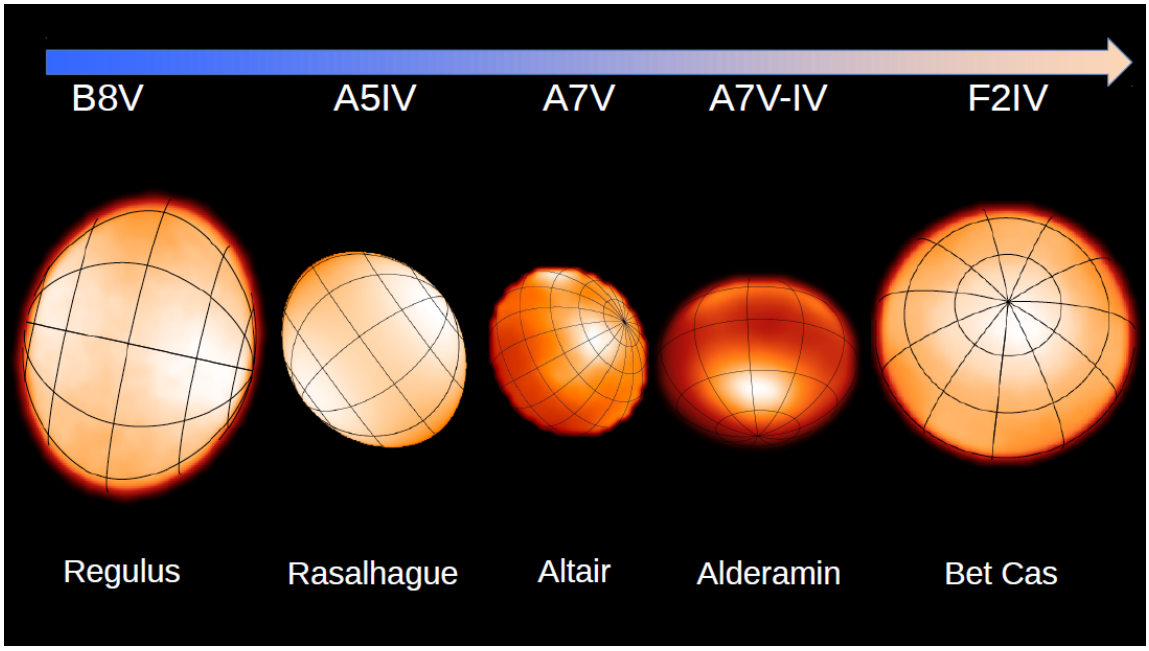

Figure 1.7: Five stars observed by the CHARA interferometer, ranked by the spectral type from the hottest to the colder ones. Uploaded composite by (Monnier, 2015).

duction of additional dishes is one of a diminished return. Since the light is combined in a pair-like fashion between the telescopes, the number of unique pairs scales linearly, as $N/2$. To address these issues, let us now explore the modern take on the Intensity Interferometry through Single Photon counting.

Chapter 2

INTENSITY INTERFEROMETRY AND SINGLE PHOTON TIMING

In recent years, there has been a revived interest in optical intensity interferometry, first demonstrated by Hanbury Brown and Twiss (HBT). Because of updated instruments, data storage, and processing techniques, the shortcomings of the half-century-old methods such as long integration time can be resolved. Additionally, the promise of completely decoupling the telescopes will allow for higher angular resolution with arbitrarily large baselines to acquire empirical data which is currently unobtainable.

The current proposals to revolutionize the field come in what essentially amounts to two separate, but complementary approaches: 1) intensity interferometry using photomultiplier tubes (PMTs) and digitizers, analogs to what Hanbury Brown and Twiss have used and 2) Single photon time tagging, effectively discretizing the measurement to nearly the photon noise limit. Advancements and proposals using PMTs is discussed in Section 2.1, while Section 2.2 is reserved for an analogue discussion with single-photon detectors (SPDs). Comparison of between PMTs and SPDs is given in Section 2.3. Near-term expected advancements in the field, their potential, and advantages over amplitude interferometry are discussed in Section 2.4.

2.1 Intensity Interferometry with Photomultiplier Tubes

Relative to the classical intensity interferometry of the Hanbury Brown and Twiss era, current methods utilizing PMTs have two distinct advantages.

While the technology behind PMTs is old, modern-day versions can achieve about a factor of 10 greater timing resolution, reduction in the instrumental noise and

additional factor of 3 increase in the quantum efficiencies Brown and Twiss (1956a). These improvements correspond to an overall increase in the signal to noise (SNR) of measurement by roughly a factor of ~ 10 for the same integration time and telescope size. A more in-depth discussion, analysis, and derivation on the SNR are given in Section 3.3.

The original measurements obtained by HBT utilized PMTs, which were coupled to an on-site mixers/correlators, thereby "connecting" telescopes via cables, similarly to how amplitude interferometry telescopes are coupled via vacuum tubes or fiber optic cables. However, modern electronics such as analog to digital converters (ADCs) and time to digital converters (TDCs) can digitize incoming signals, and *digitally store them* for future analysis. Therefore, if free space synchronization between different digitizers, comparable to the detector timing resolution τ_{det}, can be achieved, the telescopes can be completely decoupled. Arbitrarily long baselines can be established, significantly increasing the angular resolution, since the signals can be correlated in software post data acquisition.

An obvious question arises, why not just digitize the amplitude? To first order, such a task is currently impossible since the frequency of light is 2 to 3 orders higher than what is currently achievable with the fastest responding electronics. Additionally, there are not enough photons available for this to yield meaningful results. A heterodyne technique for optical wavelengths has been explored as a method to amplify the signal. The shot noise effects have been described in Rakhmanov (2001), with an application for gravitation wave detection. To be used with photon counting devices, the Cramér-Rao bound has been explored by Erkmen *et al.*, based on a proposal to use a low power oscillator Jiang and Luu (2008). While the prospect of use for intensity interferometry has been started by Le Coarer *et al.*, the topic requires additional exploration beyond the work presented in this thesis.

Applied to intensity interferometry, increase in the SNR, and complete decoupling of telescopes which increases the angular resolution, have sparked a new interest in the revival of the classical technique. Proposal to modify currently-under-construction Cherenkov Telescope Array (CTA) Dravins and LeBohec (2008); Dravins *et al.* (2013) has been made since the majority of the critical components necessary for Intensity Interferometry are already scheduled to be integrated into the telescopes. Although the purpose of the array is to observe Cherenkov radiation for high energy astrophysics, the array is also perfect for I-Int applications, with baselines spanning up to a kilometer. The telescopes sizes will vary from a few meters to a few tens of meters, composed of segmented mirrors to form a larger aperture. While the optics are poor for direct imaging, since the spot size produced on the imaging plane is quite large, it is ideal for PMTs, which have an active are on the order of centimeters. With the quantum efficiency of about 25%, this array would be able to perform measurements of stellar objects of an apparent optical magnitude of 6 and brighter Le Bohec and Holder (2006), similar to what is described for Kitt Peak trace study (See Chapter 4).

Laboratory demonstrations of post-data acquisition correlations have shown significant promise. Matthews *et al.* (2018b) have established not only the correlated signal is preserved and recoverable, but that orthogonal polarizations are uncorrelated, which suggests that each polarization can be measured independently. The simultaneous observations of both polarizations can increase the sensitivity of the measurement by a factor of $\sqrt{2}$. Due to instrumental noise, an on/off observations are required for calibration purposes, which does hinder the overall efficiency of the systems by introducing a duty cycle to the integration Matthews *et al.* (2018a). The numerous sources of instrumental noise in the PMTs can include temperature fluctuations, instability in the power supply, and digitization error in the ADCs, and others

that are beyond the scope of this publications. However, a significant portion of these effects are eliminated in the SPADs due to the fundamental architecture of the detectors, which produce a single digital pulse if a photon has been detected. Although there is dead-time of ~ 25 ps that is associated with these detectors the probability of an additional photon arriving during this time is very low unless the target being observed is very bright, and the measurements are carried out with a large telescope. The chance of such an event occurring can further be mitigated by using a narrow band filter ensuring that the incident photon rate per detector remains at ~ 10 MHz or less.

2.2 Intensity Interferometry with Single Photon Time Tagging

Advances in electronics and sensor development have allowed for the production of detectors with the ability to detect individuals photons at optical and near-infrared wavelengths. Two types of detectors, superconducting nanowire single-photon detectors (SNSPDs) and solid-state Single Photon Avalanche Diode (SPAD), are under consideration to be used in I-Int measurements.

The SNSPDs can detect an individual photon through an absorption which breaks up electron Cooper pair, creating a non-superconducting area on the wire, causing a change in the impedance and producing a voltage change. Developed at the turn of the 21st century Semenov *et al.* (2001b); Gol'Tsman *et al.* (2001), the detectors have better timing resolution ($\sim$10's ps) than their room temperature SPAD counterparts. However, the requirement of achieving superconducting temperatures in order for SNSPDs to functions make it difficult and expensive for deployment on multiple telescopes.

Similarly, the SPAD detectors operate around the breakdown voltage bias, and absorption of a photon causes an avalanche of electrons through the silicon material

Stipčević *et al.* (2010). The produced voltage spike indicated that detection has occurred. After a short period, about $\sim$ 20ns, the detector returns to the previous levels and regular operation resume; this time sets the maximum limit on the number of detectable photons over time. The backend electronics of the detector of the detector change the pulse shape into a standardized format of transistor logic TTL, which amounts to a top-hat pulse shape. The rising edge of the TTL pulse is used as a time reference, by a high-speed and accurate external clock, or when an event occurred. The jitter of the rising edge tends to be on the order of 100's of picoseconds for SPADs (see Chapter 4.6), which sets the timing accuracy of the detector τ_{det}.

While the timing resolution is worse by a factor of 10, relative to the SNSPDs, this translated to a difference of only $\sim$ 3 regarding SNR (Chapter 3.3). The advantage of SPADs over SNSPDs comes from the active area, and coupling efficiency (Chapter 4.5), cost, and commercial availability make them a more attractive choice for I-Int applications.

Numerous groups have recently explored the use of SPADs. Their use with small, commercial telescopes has been done by Horch *et al.*. Retrofitting available telescopes with SPADS has been done by the author (Pilyavsky *et al.*, 2017), and adding to the Cherenkov Telescope Array mentioned above has also been explored in (Dravins *et al.*, 2013). Significant advancements have been made, in theoretical and actual applications, of SPADs for the use with I-Int.

A couple of groups have achieved temporal photon bunching from a thermal source, which is observed by having the detectors very close or superimposed in space (via beamsplitter). The original laboratory experiment, which used a Mercury arc lamp to observe photon bunching, Hanbury Brown and Twiss, has been replicated using modern equipment by Tan *et al.*, and in Chapter 6. Also, an aperture illuminated by the Sun was used to synthesize an astrophysical-like source. To avoid

detector saturation, without sacrificing any of the signal (see Section 2.3 and 3.3), Tan *et al.* (2015, 2014) used a narrowband Fabry-Perot filter. However, Fabry-Perot filters are extremely sensitive to the temperature changes. Since the filter can expand and contract with temperature fluctuations, it is not a viable piece of equipment for multi-telescope observations; different "widths" of the filter [1] correspond to different central wavelengths and observed photons arrival times would not be correlated if the two filters are mismatched due to temperature difference between them.

Two instruments, Aqueye+ Zampieri *et al.* (2015) and Iqueye Naletto, G. *et al.* (2009), which have multiple SPAD detectors, were successfully mounted on telescopes and demonstrated to be able to measure the photon bunching effect from a *single* dish Zampieri *et al.* (2016). The custom instrument consists of detectors placed very close to one another, exposed to the light from the telescope. Because of the small separation between the detectors they can be viewed as virtually occupying the spatial mode. Additional temporal measurements on the sky have been demonstrated by Guerin *et al.* (2017).

In the last months of writing this thesis, on-sky observations using a pair of telescopes have been achieved Guerin *et al.* (2018). The demonstration was done with two 1 meter class telescopes, separated by 15 meters and physically coupled. The measured stars were βOri, a blue giant with apparent magnitude $m_R = 0.13$, αLyr, A0V type star with $m_R = 0.07$, and αAur, spectroscopic binary with $m_R = -0.52$. Their results match the predictive model discussed in Chapter 4. However, because of the location of the telescope, the baseline does not vary significantly; thus the pair of telescopes provide a single point in the $\Gamma^{(2)}$ measurement. Although not good enough for science measurements, this achievement has demonstrated, after 40+ years, the viability of I-Int with modern single-photon detectors. Plans to increase the baseline

[1] or separation between two components forming the optical cavity

by using a third telescope have been discussed in Guerin *et al.* (2018). This successful measurement further reinforces that I-Int technique should be revived with modern equipment.

2.3 Choice of Detectors

The equation for the signal to noise is derived further in the text, in Section 3.3. However, in order to draw a clear comparison between the use of PMTs and SPADs, we can focus on two parameters: 1) The quantum efficiency of the detector ϵ, and the timing resolution τ_{det}. The proportionality is $\frac{S}{N} \propto \epsilon\tau_{det}$.

Commercially available SPADs have achieved $\epsilon \sim 70\%$ compared to the PMT's ϵ which tends to be about half of that at $\sim 35\%$. When it comes to timing resolution, the two type of detectors are comparable to one another, both achieving sub-nanosecond precision ~ 0.5 ns. Based on these values, the $\frac{S}{N}$ would be higher for the SPADs by about a factor of 2. In addition to this factor, the dark count/current of the PMTs and the SPADs will contribute to noise thereby setting a limit on how dim of an object can be before these effects becoming dominant. A comparison between two commercially available units of the Excelitas SPAD SPCM-AQRH Excelitas (2016) and Hamamatsu R13089 Hamamatsu (2016) is used as an example. The dark counts for the AQRH are ≤ 600 Hz and with the Hamamatsu R13089 radiant sensitivity of $2.5(10^4)$ A/W, which corresponds to approximately ~ 1 MHz in terms of the dark current. These factors constrain the limiting magnitudes observable from telescopes and are summarized in Figure 5.3, which initially appeared in Sinclair *et al.* (2016).

While the S/N is not directly affected by the bandwidth (See Section 3.3), there is a subtle effect which stems from using multiple spectral channels. Sub-nm optical filter diffraction gratings can be used in combination with multiple detectors on the telescope in order to increase the S/N ratio. SPADs require significantly fewer

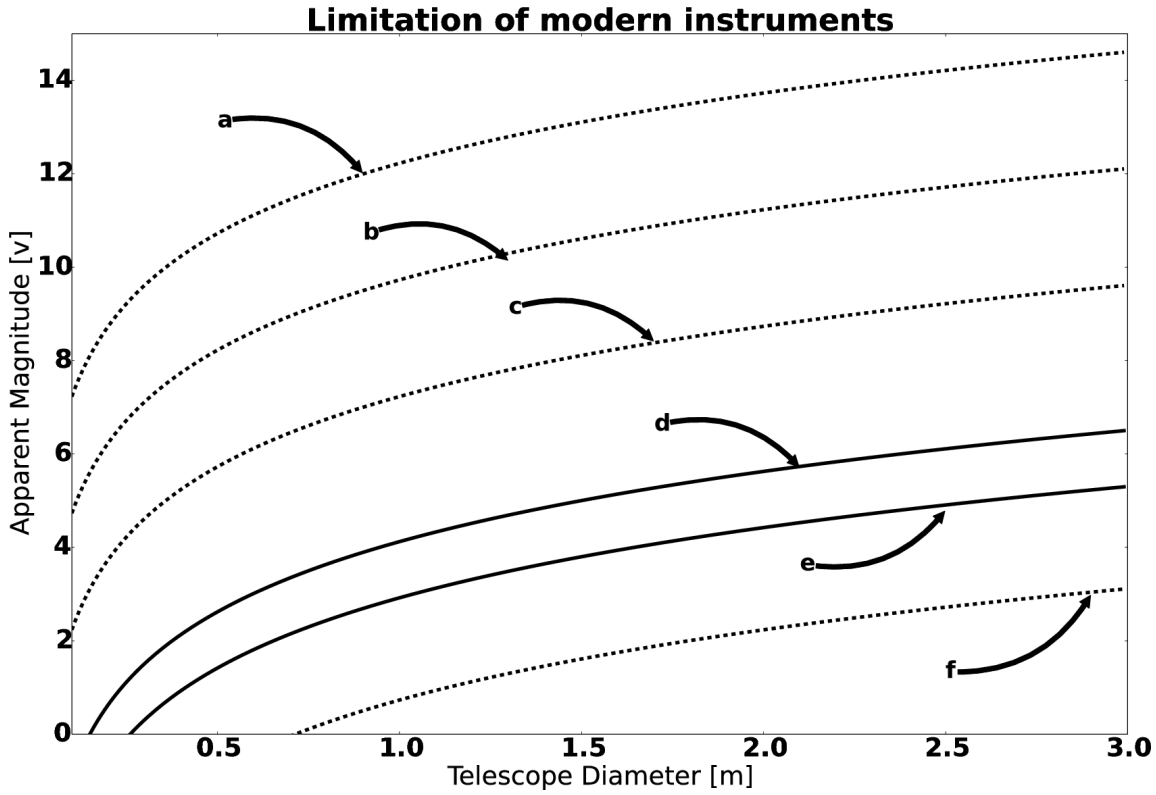

Figure 2.1: Parameter space of telescope diameter (in meters) and apparent stellar magnitude (m_v). Different curves represent the limitation of modern instruments as follows: a) SPADs, 1 nm filter ($\Delta\lambda$), $\sim$1kHz count rate per detector b) PMT, $\Delta\lambda$=100 nm, 1MHz count-rate per detector c) PMT, $\Delta\lambda$=10 nm 1MHz count-rate per detector d) Two point correlation with SPADs, 8 hour long integration, S/N=5; the approximate limit of PMT, with $\Delta\lambda$=1 nm, 1MHz count-rate per detector e) Two point correlation with PMT, 8 hour long integration, S/N=5 f) SPADs saturation limit, assuming 20MHz count rate at the detector *after* polarization has been removed.

photons to operate above their dark count rate; they may be more applicable where a spectrograph approach is utilized. Simultaneous observations of different parts of the spectrum would allow for each spectral channel to act as an independent measurement, thus increasing the overall sensitivity by a factor of $\sqrt{N_c}$, where N_c is the number of unique spectral channels.

The PMTs do have a clear advantage over SPADs in one aspect, and that is the active area. The active area of Hamamatsu R13089 is 45 mm, about 200 times larger than the SPAD's active area of 200 μm. Having the larger active area relaxes the constraints on the quality of the optical mirrors, making the detectors less susceptible to optical aberrations.

A SPAD is a Geiger mode detector and carries information in the time and frequency of pulses as opposed to a PMT in a linear mode which produces an electrical output that is proportional to the optical input within a particular response time. The optimal readout for both types of detectors differ. Geiger mode detectors require a digital pulse counter or time-to-digital converter (TDC). Modern linear mode detectors require an analog-to-digital converter (ADC). When it comes to data storage, processing, and handling, the number of bits generated per second by a TDC and SPAD combination may be compared with a PMT and ADC combination. An advantage of the PMT/ADC method in the high photon rate over the TDC/SPAD method is the independence of photon rate in the number of bits generated per second. This is a disadvantage for the PMT/ADC method in the low photon rate limit where the average number of empty samples is f_{ADC}/N_p, where f_{ADC} is the ADC sampling frequency and N_p is the photon rate. The photon rate required for the TDC/SPAD at which the two methods generate the same number of bits in one channel is

$$N_p = \frac{W_{TDC}}{W_{ADC}} \times f_{ADC}, \tag{2.1}$$

where W_{TDC} is the number of bits in a TDC measurement and W_{ADC}, is the number of bits of the ADC. These factors may be ignored for the case of onboard real-time correlation. However, the long-term goal of I-Int is the decoupling of telescopes. In this case, data must be stored as efficiently as possible to resolve smaller objects with longer baselines.

The bottom line is that PMTs are favorable to use with large telescopes, wide bandwidth, and imperfect optics, wheres the smaller telescopes would be better utilized with SPADs.

2.4 Higher Order Correlation and Closure Phase

While advantages of digitizing and storing data allow for de-coupling of instruments, there are additional benefits which can be explored. Hidden from the two-point correlation, information regarding the emitter can be obtained by exploring higher orders of correlation. Similarly to Equation 1.7, a mathematical description of third-order correlation can be given as

$$\begin{aligned}\gamma^{(3)}_{1,2,3} &= \frac{\langle I_1 I_2 I_3\rangle}{\langle I_1\rangle\langle I_2\rangle\langle I_3\rangle} \\ &= 1 + |\gamma_{1,2}|^2 + |\gamma_{2,3}|^2 + |\gamma_{3,1}|^2 + 2\mathcal{R}\{\gamma_{1,2}\gamma_{2,3}\gamma_{3,1}\}.\end{aligned} \tag{2.2}$$

With $\gamma_{1,2}$, $\gamma_{2,3}$, and $\gamma_{3,1}$ obtained from a two-point correlation between the three pairs of telescopes, represented by the indexes 1, 2, and 3. The *real* component of the third order correlation is obtainable with equation 2.2. Although some image reconstruction is possible in the absence of phase information Nunez *et al.* (2010); Dravins *et al.* (2015), some degeneracies in the solution remain. The additional information included in the measurement of $\gamma^{(3)}_{1,2,3}$ is a component of the complex amplitude, which implies partial preservation of phase information. This information

could be used to constrain stellar surface models and aid in image reconstruction, as explored in (Malvimat *et al.*, 2013).

The third order correlation is referenced to as "closure phase", and is often used in radio astronomy for aperture synthesis. Perturbations in the relative phases of waves incident onto the telescopes are due to different atmosphere cells above the telescopes. These errors are removed with the closure phase. Examining just the phase components of the exponential term in the complex amplitude, the relationship for the three measurements of can be written as

$$\begin{aligned} \phi_{1,2} &= \theta_{1,2} + \epsilon_1 - \epsilon_2 \\ \phi_{2,3} &= \theta_{2,3} + \epsilon_2 - \epsilon_3 \\ \phi_{3,1} &= \theta_{3,1} + \epsilon_3 - \epsilon_1. \end{aligned} \tag{2.3}$$

The ϕ variable is representing the phase component at the telescopes, θ is the phase before the atmosphere perturbation, and ϵ is representing the errors introduced by the atmosphere. The product of $\gamma_{1,2}$, $\gamma_{2,3}$, and $\gamma_{3,1}$ translates to the summation of the phase components such that

$$\begin{aligned} \phi_{1,2} + \phi_{2,3} + \phi_{3,1} &= \theta_{1,2} + \epsilon_1 - \epsilon_2 + \theta_{2,3} + \epsilon_2 - \epsilon_3 + \theta_{3,1} + \epsilon_3 - \epsilon_1 \\ &= \theta_{1,2} + \theta_{2,3} + \theta_{3,1}. \end{aligned} \tag{2.4}$$

Not only does the closure phase remove atmospheric effects, but systematics in the electronics/cables/detectors are also mitigated. Higher order correlations (4+) are also possible, and calculating the values requires nothing but appropriate software and algorithms. While there may be additional information in higher-order correlations, they are not likely to be observed with optical interferometers in the near future since the signal to noise ration is poor, as described in Section 3.5.

2.5 Scalability of the telescope array

The scalability of different types of interferometers and techniques is an important subject to examine as the relationship is not linear and is informative as to the "upgradability" of the telescope array.

In the case of an amplitude interferometer, the measurements require that each telescope be optically coupled to another. It is possible to split the light from a single telescope, and recombine it with multiple other telescopes. However, when the light is split by $N-1$ the signal to noise ratio which goes as the square root of the number of photons decreases by $\sqrt{N-1}$, and there is some photon loss due to optical components which tend to be close to, but not 100% efficient. The number of detectors required increases quadratically with the number of telescopes, and linearly with the number of baselines in use.

In the case of intensity interferometry or photon arrival time tagging, the scalability is significantly more favorable. The question of "How many unique baselines can be produced" is addressed in the classical statistical scenario of given N_t a total number of items (telescopes), and picking out (correlating) N_c number (telescopes) together, the number of combinations (available baselines) N_b is expressed as

$$N_b = \frac{N_t!}{N_c!(N_t - N_c)!}. \tag{2.5}$$

If we were to correlated just pair of telescopes to obtain $\Gamma_{i,j}$, Equation 2.5 simplifies to $N_b = \frac{N_t(N_t-1)}{2}$. Similarly, for a three-point correlation of $\Gamma_{i,j,k} \rightarrow N_b = \frac{N_t(N_t-1)(N_t-2)}{6}$. These results imply that the scalability of an I-Int array is a lot more favorable to the introduction of additional telescopes relative to the currently used I-Int method. Introduction of additional telescopes does not require complicated optics to split/recombine the light, and the number of detectors scales as the number

of telescopes, and not the number of baselines.

2.6 UV-plane Exploration Due to Earths Rotation

With multiple telescopes, many projected baselines are created in the UV-plane, sometimes referenced as wave-space, k-space or Fourier space. Taking out an elevation component and observing the telescopes from a bird's eye view, the telescopes would appear as small points distributed in some patter along the x- y-plane. The line can then be drawn from each telescope to the others. Placing the center of the line segments at the same point would give us the projected baseline separation amongst all the unique pairs.

Alternatively, the different baselines produced by the telescopes can be obtained by taking the Fourier transform of this two-dimensional plane, resulting in $N_t(N_t - 1)/2$ number of points, where N_t is the number of telescopes in the setup. However, the measurement obtained from such a setup would provide an abysmal sampling of the UV-plane due to under-sampling. Luckily, Earths rotation helps to vary the location of these points, increasing the total sampling area.

A couple of parameters determine the projected baseline between a pair of telescopes. The physical location of the telescope plays a significant role, as this corresponds to which stars are observable. The latitude and longitude position is of importance so that an actual physical separation can be obtained. Furthermore, the latitude and longitude also inform us of how the baseline is going to change as the Earth rotates throughout the integration time. The RA and DEC coordinates of the star are also of vital importance since the spacial relationship between the star and the telescopes are continuously changing. Lastly, the observational wavelength matters, and acts as a scale factor for the UV-plane coverage, mainly stretching and contracting the k-space.

This information can be obtained by using the coordinate transformation matrix from Ségransan (2007), which is given in Equations 2.6. The variables used in the matrix are defined in Table 2.1.

$$\begin{bmatrix} u \\ v \\ \omega \end{bmatrix} = \frac{1}{\lambda} B_p = \frac{1}{\lambda} \begin{bmatrix} a_1, a_2, a_3 \\ b_1, b_2, b_3 \\ c_1, c_2, c_3 \end{bmatrix} \begin{bmatrix} B_{north} \\ B_{east} \\ B_{up} \end{bmatrix} . \tag{2.6}$$

$$a_1 = -\sin(l)\sin(h) \qquad a_2 = \cos(h)$$

$$a_3 = \cos(l)\sin(h) \qquad b_1 = \sin(l)\cos(h)sin(\delta) + \cos(l)\cos(\delta)$$

$$b_2 = \sin(h)\sin(\delta) \qquad b_3 = \cos(l)\cos(h)\sin(\delta) + \sin(l)\cos(\delta)$$

$$c_1 = -\sin(l)\cos(h)\cos(\delta) + \cos(l)\sin(\delta) \qquad c_2 = -\sin(h)\cos(\delta)$$

$$c_3 = -\cos(l)\cos(h)\cos(\delta) + \sin(l)\sin(\delta)$$

Understanding and modeling the changes in the baseline is vital, as we shall see in future sections. Where in the UV-plane the measurements have been taken are used to obtain $\Gamma^{(2)}$. The ω component is responsible for the temporal delay in the arrival time of the correlated photons and could shift where the signature occurs, as we will see in Section 4.3.

Table 2.1: Variables use in Equation 2.6

Variable	Definition
λ	Central wavelength
l	Telescope latitude
δ	Declination of the star
h	Hour angle of the star
B_{north}	Separation between telescopes along latitude
B_{east}	Separation between telescopes along longitude
B_{up}	Change in elevation between telescopes
u	Wave-space component corresponding the North-South separation between the telescopes
v	Wave-space component corresponding to the East-West separation between the telescopes
ω	Wave-space component corresponding to elevation difference between telescopes, often changed to temporal space.

Chapter 3

PHOTON STATISTICS

Before modeling and predicting system behavior, requirements, and achievable science goals, a few concepts need to be established. The single photon experiments rely on the interaction of two-photon wave-function (Section 3.1). While the probability of observing two simultaneous photons is low, modern single-photon detectors are sensitive enough to make the measurement. The wave-function will only interact with one another if the photons are within the same coherence time, Section 3.2, where the photons are indistinguishable from one another.

The timing precision of state of the art instruments are approaching that of the coherence time, with a 0.1 nm commercially available filter translating to $\sim$10 ps. This timing precision is on the order of what has been achieved with nanowires, as demonstrated by Zadeh *et al.* (2018), while SPADs remain about an order of magnitude away. The ability to control the coherence time of the system and the effect it has on the signal to noise ration is further discussed in Section 3.3. The SNR calculation relies on knowing the angular size of the object, as well as the temperature of the source. This information is often unavailable but can be approximated from knowing stellar magnitudes [1] and the spectral type of the star, as discussed in Section 3.4.

Furthermore, it is possible to obtain higher order correlations since the data for the measurement is stored digitally. The derivation for the expected signal to noise

[1] since the stars are blackbodies, we do not need to know the temperature.

of higher order $\Gamma^{(n)}$ is given in Section 3.5.

3.1 Quantum of photon bunching

The coherent quantized electrical field can be expressed as

$$E(r) = i \sum_{k,\mu} \sqrt{\frac{\hbar\omega_k}{2V\epsilon_o}} \left(p_\mu a_\mu(k) e^{ik\cdot r} - p_\mu^* a_\mu^\dagger(k) e^{-ik\cdot r} \right). \tag{3.1}$$

However, to demonstrate the effect of photon bunching, the equation can be significantly simplified by eliminating some terms; each term will be discussed as we progress further towards a simplified form of Equation 3.1. For example, the subscript μ corresponds to the polarization (± 1). Examining single polarization, the index can be discarded, along with the polarization vector p_μ and its complex conjugate p_μ^*. The Planck constant $\hbar$, angular frequency $\omega_k = c\,|k|$, potential (V) and the electric constant (ϵ_o) will act as scalers, which means they too can be disregarded as we are not interested in energy, only relative photon count.

Furthermore, assuming that everything considered in this example is happening at the same spatial location, so the dependency on the wave vector k can be eliminated from the sum. The newer and simpler equation becomes

$$E \propto i \left(a e^{ik\cdot r} - a^\dagger e^{-ik\cdot r} \right) \tag{3.2}$$

which leaves the photon creation and annihilation operators $(a, a^\dagger)$ and components of the Fourier basis $e^{\pm ik\cdot r}$. The creation and annihilation operators stem from the quantization of the electrical field and the total energy in the system, as represented by the Hamiltonian as

$$H = \hbar\omega \left(a^\dagger a + \frac{1}{2} \right) \tag{3.3}$$

with zero-point energy of $\frac{\hbar\omega}{2}$. In this harmonic oscillator form, the creation operator is analogous to an excitation, while the annihilation operator is de-excitation. The product of $a^\dagger a$ yields the quanta of excitations, a photon, and is represented by a number operator n. The reverse combination of $aa^\dagger$ is $n+1$, forming the relationship of

$$aa^\dagger - a^\dagger a = 1. \tag{3.4}$$

These formulations are discussed in basic quantum texts and are not necessary for the concept demonstration of special cases given below.

Three cases will be examined, an observation of a single photon, observation of two distinguishable photons, and observations of indistinguishable photons. In a single photon case, the measurement can be described as

$$EE^* \propto \left(a_1 e^{ik\cdot r} - a_1^\dagger e^{-ik\cdot r}\right)\left(a_1^\dagger e^{-ik\cdot r} - a_1 e^{ik\cdot r}\right), \tag{3.5}$$

with index of 1 introduced to the photon operators indicating a unique photon. There are four different products produced in this case,

$$a_1 a_1^\dagger, \quad \cancel{-a_1 a_1 e^{2ik\cdot r}}, \quad \cancel{-a_1^\dagger a_1^\dagger e^{-2ik\cdot r}}, \quad a_1^\dagger a_1. \tag{3.6}$$

The terms with paired creation-creation and annihilation-annihilation operators are invalid, and also imaginary. Therefore, only two terms, $a_1 a_1^\dagger$ and $a_1^\dagger a_1$ contribute to the photon detection. It is fair to assume that if another identifiable photon is present, Equation 3.7 should be scaled by a factor of 2. This is easily verifiable, if we rewrite Equation 3.7 for a pair of photons with creation and annihilation operators a_1, a_2 and $a_1^\dagger, a_2^\dagger$ as

$$EE^* \propto \left(a_1 e^{ik\cdot r} - a_1^\dagger e^{-ik\cdot r} + a_2 e^{ik\cdot r} - a_2^\dagger e^{-ik\cdot r}\right)\left(a_1^\dagger e^{-ik\cdot r} - a_1 e^{ik\cdot r} + a_2^\dagger e^{-ik\cdot r} - a_2 e^{ik\cdot r}\right). \tag{3.7}$$

In this case, 16 terms are produces, which are:

$$\begin{aligned}
&a_1 a_1^\dagger, \quad \cancel{-a_1 a_1 e^{2ik\cdot r}}, \quad \cancel{a_1 a_2^\dagger}, \quad \cancel{-a_1^\dagger a_2^\dagger e^{2ik\cdot r}} \\
&\cancel{-a_1^\dagger a_1^\dagger e^{-2ik\cdot r}}, \quad a_1^\dagger a_1, \quad \cancel{-a_1^\dagger a_2^\dagger e^{-2ik\cdot r}}, \quad \cancel{a_1^\dagger a_2} \\
&\cancel{a_2 a_1^\dagger}, \quad \cancel{-a_2 a_1 e^{2ik\cdot r}}, \quad a_2 a_2^\dagger, \quad \cancel{-a_2 a_2 e^{2ik\cdot r}} \\
&\cancel{-a_2^\dagger a_1^\dagger e^{-2ik\cdot r}}, \quad \cancel{a_2^\dagger a_1}, \quad \cancel{-a_2^\dagger a_2^\dagger e^{-i2k\cdot r}}, \quad a_2^\dagger a_2
\end{aligned} \tag{3.8}$$

Again, pairs with identical operators are invalid and are not considered. Additionally, operators with different indices such as $a_i a_j^\dagger$ (and other perturbations of this pair), where $i \neq j$, are zero. This leaves four valid terms, as previously predicted. However, in the case where the photons are indistinguishable from one another, it is impossible to assign unique index values to the photon operators, which means Equation 3.9 becomes

$$\begin{aligned}
&aa^\dagger, \quad \cancel{-aae^{2ik\cdot r}}, \quad aa^\dagger, \quad \cancel{-a^\dagger a^\dagger e^{2ik\cdot r}} \\
&\cancel{-a^\dagger a^\dagger e^{-2ik\cdot r}}, \quad a^\dagger a, \quad \cancel{-a^\dagger a^\dagger e^{-2ik\cdot r}}, \quad a^\dagger a \\
&aa^\dagger, \quad \cancel{-aae^{2ik\cdot r}}, \quad aa^\dagger, \quad \cancel{-aae^{2ik\cdot r}} \\
&\cancel{-a^\dagger a^\dagger e^{-2ik\cdot r}}, \quad a^\dagger a, \quad \cancel{-a^\dagger a^\dagger e^{-i2k\cdot r}}, \quad a^\dagger a.
\end{aligned} \tag{3.9}$$

In total, eight terms are valid, which is twice more than what has been shown with individual photons in different, distinguishable states. This example yields similar results to classically derived amplitude interferometry. In the case of an incoherent source, such as stars, the photons will have random phases. Having multiple photons

of different frequencies will amount to "beating" between them. Because they are of different frequencies, their phases will go in and out of alignment, and for a short duration of time, they will appear to be coherent, and be indistinguishable from one another. This time is rightfully denoted as coherence time.

3.2 Photon Occupation Number and Coherence Time

We begin by defining the photon occupation number η_{occ} as the number of observable photons per second, per mode, per Hz emitted from a source. The mathematical equation describing this state is derived from the Bose-Einstein statistics. Since photons fall into a category of bosons, two particles of the same energy are allowed to not only be superimposed spatially/temporally but are also indistinguishable from one another when this occurs. Because the photon energy is proportional to the frequency (inversely proportional to the wavelength), if the bandwidth is narrow enough, the number of photons with the same energy can be approximated as

$$\eta_{occ} = (e^{hc/\lambda kT} - 1)^{-1}, \tag{3.10}$$

where h, k, c are Planck, Boltzmann, and speed of light constants. The temperature of the source is represented by the variable T, and λ is the central wavelength of light used for the measurement. The value is given for a single polarization, within the same coherence volume, where the photons are considered to be indistinguishable from one another.

The x-y- dimensions of this coherence volume, the imaging plane, is probed by the telescopes of varying baselines. The z- dimension of the volume can be converted to *coherence time* (τ_c), which is inversely proportional to the bandwidth ($\Delta\nu$).

Since single-photon interferometry relies on the precise time of arrival measurements, high-speed electronics are necessary. However, even with the state of the art

electronics, probing this temporal domain is extremely difficult. At optical wavelengths ($\sim$ 650 nm), even with a 0.1 nm bandwidth filter, the coherence time $\tau_c = \left[\frac{\lambda^2}{\Delta\lambda c}\right]$ is $\sim$15 picoseconds. Ideally, the detectors need to match this value. However, this timing precision is an order of magnitude higher than the room temperature single photon avalanche diode (SPAD) and only recently beginning to be matched by superconducting nanowire single-photon detectors (SNSPD).

3.3 Signal to Noise Ratio of Coherent, and False Positive Photons

With the occupation number defined, we can explore the probability of photon detection at a given telescope. The number of photons incident upon the detector per second (γ_p) is going to be set by the occupation number, quantum efficiency of the system (ϵ), and the bandwidth. Since the bandwidth is not infinitesimally small, its contribution of $\Delta\nu = \frac{\Delta\lambda c}{\lambda^2}$ needs to be accounted for. Combining all these factors, the number of incident photons, per second per m^2 is

$$\begin{aligned} \gamma_p &= \epsilon\, \eta_{occ}\, \Delta\nu \\ &= \epsilon\, \eta_{occ}\, \frac{\Delta\lambda}{\lambda^2} c. \end{aligned} \tag{3.11}$$

Knowing γ_p, we can explore the probability of detecting two photons simultaneously, from the same coherence time as simultaneous detection where our inability to temporally resolve two photons yields a false positive.

The total number of correlated photons observed (γ_c) is set by the system efficiency of both the "arms" of the interferometers (ϵ^2), joined occupation number (η_{occ}^2) from the same coherence time ($\Delta\nu$). Additionally, the angular size of the illuminator (Ω), which contributed to the total number of observable modes $\frac{A\Omega}{\lambda^2}$, where A is the collecting area of the telescope, contributed to the total number of observed photons. Lastly, the total integration time devoted to the experiment (τ_{int}), since the longer

the observation is carried out for, the more "pairs" of photons can be observed. Combining all the terms yields

$$\gamma_c = \epsilon^2 \, \eta_{occ}^2 \, \Delta\nu \left(\frac{A\Omega}{\lambda^2} \right)^2 \tau_{int}. \tag{3.12}$$

Similarly, the number of false positive coincident hits depend on the same parameters with the exception of coming from differentness coherence times ($\Delta\nu^2$) set by the timing resolution of the detector τ_{det} (or the readout electronics) which gives us:

$$\gamma_{uc} = \epsilon^2 \, \eta_{occ}^2 \, \Delta\nu^2 \left(\frac{A\Omega}{\lambda^2} \right)^2 \tau_{int} \, \tau_{det}. \tag{3.13}$$

The only difference between Equation 3.12 and 3.13 is $\Delta\nu$ vs $\Delta\nu^2$ and additional variable τ_{det}. The reasoning behind this can be explained by observing Figure 3.1, which represents a three-dimensional parameter space with temporal, spectra, and photon occupation number as its dimensions. It is useful to recall that the coherence time is inversely proportional to the bandwidth.

Therefore, in the coherent case, we are picking two photons from the volume, hence η_{occ}^2. Furthermore, they are picked out from the available spectral range $\Delta\nu$, out of the same coherence time (τ_c), which is just a sliver of the temporal domain since the detectors are unable to resolve it. Similarly, for in the uncorrelated case, we are picking one photon (η_{occ}), from some bandwidth ($\Delta\nu$) across our detectors temporal resolution ($\tau_{det} >> \tau_c$) and then another photon from the same τ_{det}, which yield another factor of η_{occ} and $\Delta\nu$.

The signal to noise ration, $\frac{S}{N}$ is defined as the ration of the correlated photons γ_c to the white noise fluctuations of the uncorrelated photons $\gamma_{un}^{0.5}$:

$$\frac{S}{N} = \frac{\gamma_c}{\gamma_{uc}^{0.5}} = \epsilon \, \eta_{occ} \, \frac{A\Omega}{\lambda^2} \left(\frac{\tau_{int}}{\tau_{det}} \right)^{0.5} \Gamma^{(2)}. \tag{3.14}$$

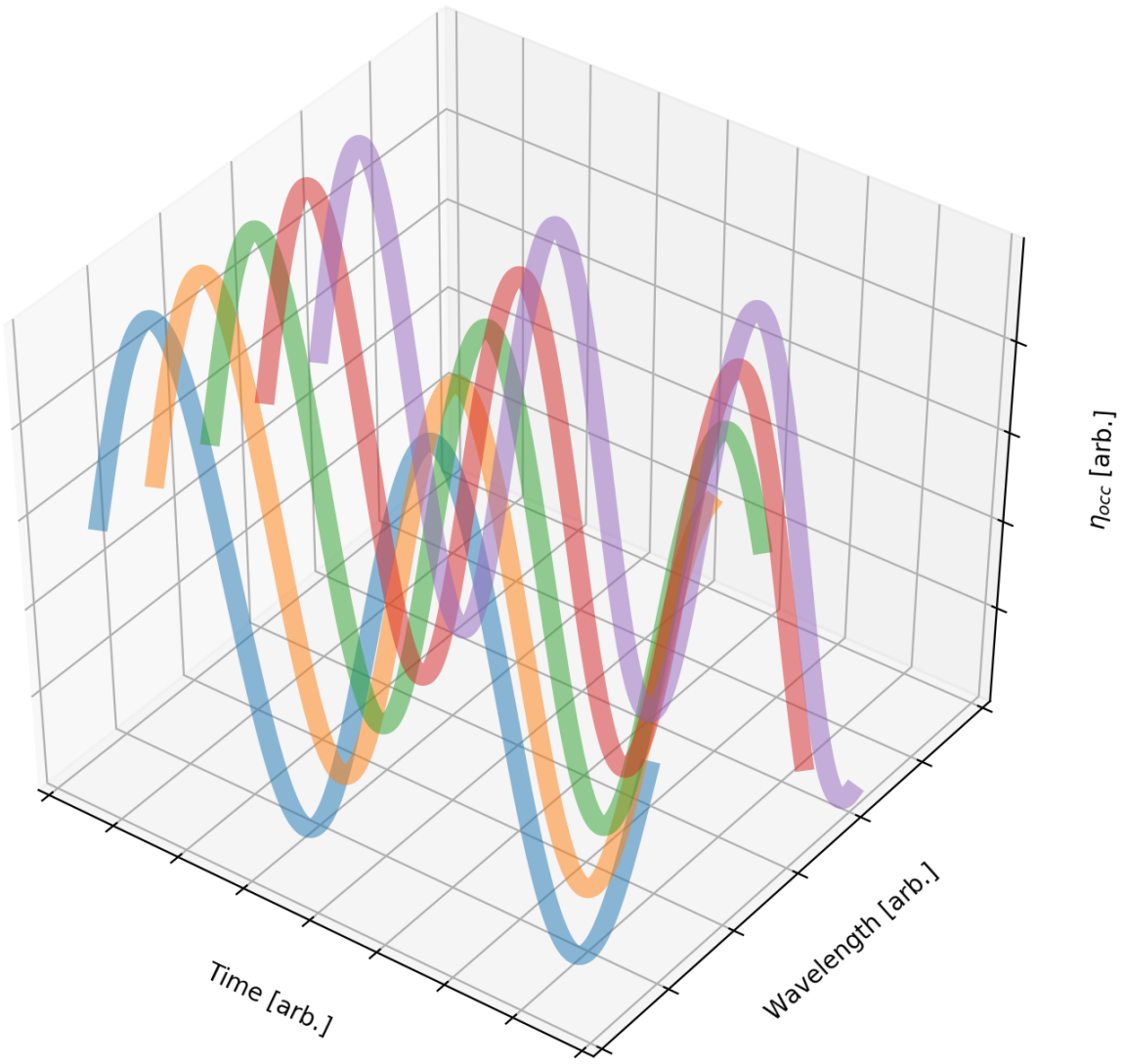

Figure 3.1: Three dimensional space of η_{occ}, $\Delta\nu$ and time, in arbitrary units. Multiple sinusoidal lines are representative of slightly different wavelengths. Color has been arbitrarily chosen for clarity and does not correspond to any particular wavelength.

The factor of $\Gamma^{(2)}$, with values ranging between 0 and 1, is introduced into the equation to scale the total number of correlated photons as different portions of the coherence volume are probed by varying the projected baseline between the telescopes. The fraction of $\frac{A\Omega}{\lambda^2}$ is included to introduce for the number of modes, as well as the

telescope collecting area.

It is of importance to observe that equation 3.14 is **not dependent on bandwidth** $\Delta\nu$. The implications are such that 1) count rate can be varied to avoid detector saturation or domination due to dark counts without sacrificing the integrity of measurement and 2) multiple spectral channels can be utilized to increase the overall $\frac{S}{N}$, as each spectral channel functions as a unique, interdependent measurements relative to the other spectral channels.

3.4 Signal to noise from stellar magnitude

At times, it is easier to compute the expected SNR from a known and measured apparent stellar magnitude. Calculations using the occupation number are dependent on three unknowns, temperature, distance, and size of the star. This information may not be readily available, especially since the actual size of the source is what the I-Int is attempting to measure. However, stellar magnitudes inherently have this information already built into their measured quantities.

3.4.1 From Bessel calibration

We can compute the expected SNR based on the Bessel calibrations Bessell (1979). By knowing the stars apparent magnitude, it is possible to approximate the incident photon rate from defining the Janskys units as

$$1Jy = 10^{-26}. \tag{3.15}$$

in units of Juels sec^{-1} m^{-2} Hz^{-1}. Photon energy an be expressed as $E = hc/\lambda$ with $h = 6.626(10^{-34})$ and $c = 3(10^{8})$.

Combining the constants, the energy of a photos is $hc/\lambda = 1.99(10^{-25})/\lambda$. Rewriting Equation 3.15 as

$$
\begin{aligned}
1Jy &= \frac{10^{-26}\lambda}{1.99(10^{-25})} \\
&= \frac{\lambda}{20}
\end{aligned}
\tag{3.16}
$$

in units of photons s^{-}1 m^{-2} Hz^{-1}. The Bessel approximation can be done for multiple bands to obtain the expected photon count rate N_p per m^2 perf Hz with Equations 3.17. Expressed as

$$
N_p = \frac{\lambda}{20} \times 2.512^{m_x} F_x \tag{3.17}
$$

with m$_x$ representing apparent magnitude at a specific optical band, and F_x are the calibrated values. The values for different bands are shown in Table 3.1. If the interest is to obtain an actual photon count rate, the factor of calibrated bandwidth $\frac{\Delta\lambda}{\lambda}$ needs to be introduced, which is also available in Table 3.1. However, for a substitution into the SNR Equation 3.14, which is bandwidth independent, Equation 3.17 is sufficient since $N_p = \eta_{occ}\frac{\Omega}{\lambda^2}$.

3.4.2 Comparing and Converting η_{occ} to Bessell Calibration for SNR Calculation

The comparison of η_{occ} relative to the Bessell calibration was done on $\sim$ 2500 stars, obtained from the Bright Star Catalogue Hoffleit and Jaschek (1991). The Giant class stars were not included in the analysis. Table 3.2 was used as a calibrator, for values of temperature and radii of spectral types O5 through M0. The distance, in parsecs, was deduced from their measured apparent magnitude m_v and their absolute magnitude M_v as

$$
d_{pc} = 10.0^{(m_v - M_v + 5)/5}. \tag{3.18}
$$

Computed values of $\eta_{occ}\frac{\Omega}{\lambda^2}$ and N_p were compared as a ratio. An Error of 5% (one sigma) was introduced for uncertainties in the distance, size, and temperatures

Table 3.1: Table of calibrated fluxes from $m = 0$ sources. The information within this table was obtained from McGaugh *et al.*

Band	Observation λ μm	$\frac{\delta\lambda}{\lambda}$	F_x at m=0 Jy	Reference
U	0.36	0.15	1810	Bessell (1979)
B	0.44	0.22	4260	Bessell (1979)
V	0.55	0.16	3640	Bessell (1979)
R	0.64	0.23	3080	Bessell (1979)
I	0.79	0.19	2550	Bessell (1979)
J	1.26	0.16	1600	Campins *et al.* (1985)
H	1.60	0.23	1080	Campins *et al.* (1985)
K	2.22	0.23	670	Campins *et al.* (1985)
g	0.52	0.14	3730	Schneider *et al.* (1983)
r	0.67	0.14	4490	Schneider *et al.* (1983)
i	0.79	0.16	4760	Schneider *et al.* (1983)
z	0.91	0.13	4810	Schneider *et al.* (1983)

of the stars. Three values of η_{occ} were computed: 1) η_{occ}^{hi} with errors T+σ_T, R+σ_R, and D-σ_D, creating a hotter, larger, and closer star 2) η_{occ}^{med} with no errors, and 3) η_{occ}^{lo} with errors of T-σ_T, R-σ_R, and D+σ_D which yield a colder, smaller, further away star. For each of the three variations, the average value for a given spectral type was used.

Upon examining Figure 3.2, it becomes evident that the two methods match, to first order. The η_{occ}^{med} works very well for spectral types of A0 to M0. However,

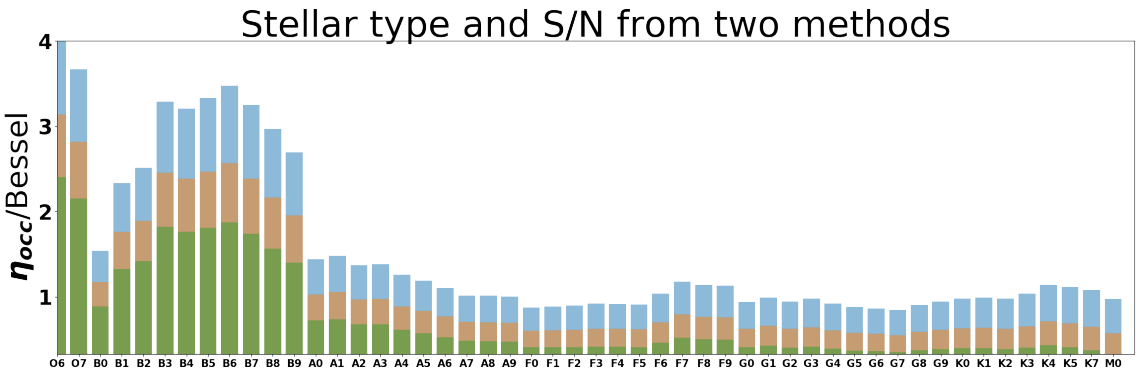

Figure 3.2: Comparison of η_{occ} to Bessel approximation approaches, as a ratio, in calculating an SNR target, based on a spectral type (y-axis) is shown. The blue corresponds to the maximum value of η_{occ} obtained by using the upper error bounds for temperature and radius, and lower error bound for distance; hottest, biggest, and closes object. The yellow represents the accepted value of temperature, size, and distance. The green is the lowest bounds for temperature and radius, with the largest possible distance.

the relationship appears to diverge for the hot O and B type of stars, with the η_{occ} systematically overshooting the expected value from the Bessell calibration. This behavior is intrinsic to a bias estimated, and in this particular case, can be attributed to the data in Table 3.2, which served more as a rough guide rather than precisely measured quantities. Surprising, B0 type stars also appear to match.

Table 3.2: Main sequence spectral types, along with their temperature, absolute magnitude, luminosity and radii. Values obtained from Morgan.

Spectral Type	Temp. [K]	M_v	L $[L_\odot]$	R $[R_\odot]$	Spectral Type	Temp. [K]	M_v	L $[L_\odot]$	R $[R_\odot]$
O5	54000	-4.5	200000	15	O6	45000	-4.0	140000	14
O7	43300	-3.9	120000	13	O8	40600	-3.8	80000	12
O9	37800	-3.6	55000	11	B0	29200	-3.3	24000	8.4
B1	23000	-2.3	5550	7.86	B2	21000	-1.9	3190	7.32
B3	17600	-1.1	1060	6.78	B4	16400	-0.8	720	6.24
B5	15200	-0.4	380	5.7	B6	14300	0	240	5.16
B7	13500	0.3	140	4.62	B8	12300	0.7	73	4.08
B9	11400	1.1	42	3.54	A0	9600	1.5	24	2.7
A1	9330	1.7	20	2.6	A2	9040	1.8	17	2.5
A3	8750	2.0	14	2.4	A4	8480	2.1	12	2.3
A5	8310	2.2	11	2.2	A6	8115	2.3	9.9	2.1
A7	7920	2.4	8.8	2.0	A8	7730	2.6	7.566	1.9
A9	7540	2.8	6.333	1.8	F0	7350	3.0	5.1	1.6
F1	7200	3.15	4.45	1.56	F2	7050	3.3	3.8	1.52
F3	6850	3.5	3.2	1.48	F4	6775	3.6	2.95	1.44
F5	6700	3.7	2.7	1.40	F6	6550	4.0	2.0	1.36
F7	6400	4.3	1.5	1.32	F8	6300	4.4	1.4	1.28
F9	6175	4.55	1.3	1.24	G0	6050	4.7	1.2	1.1
G1	5930	4.9	1.1	1.075	G2	5800	5.0	1.0	1.05
G3	5753	5.13	0.91	1.025	G4	5706	5.16	0.82	1.0
G5	5660	5.2	0.73	0.975	G6	5587	5.3	0.657	0.95
G7	5514	5.4	0.584	0.925	G8	5440	5.6	0.51	0.90
G9	5340	5.8	0.445	0.875	K0	5240	6.0	0.38	0.85
K1	5110	6.2	0.32	0.83	K2	4960	6.4	0.29	0.81
K3	4800	6.7	0.24	0.79	K4	4600	7.1	0.18	0.77
K5	4400	7.4	0.15	0.75	K6	4200	7.7	0.13	0.73
K7	4000	8.1	0.11	0.71	K8	3916	8.3	0.1	0.69
K9	3832	8.6	0.09	0.67	M0	3750	8.7	0.080	0.63
M1	3700	9.4	0.055	0.584	M2	3600	10.1	0.035	0.538
M3	3500	10.7	0.027	0.492	M4	3400	11.2	0.022	0.446
M5	3200	12.3	0.011	0.4	M6	3100	13.4	0.0051	0.354
M7	2900	13.9	0.0032	0.308	M8	2700	14.4	0.0020	0.262
M9	2500	14.9	0.0008	0.216					

3.5 Signal to Noise Ratio in Higher Order Correlations

Because the photon arrival times are digitally stored, with cross-correlation performed after the acquisition, higher order correlations can also be computed. Additional information can be extracted from the odd order correlations, such as partial phase information, as described in Section 2.4, as well as Malvimat *et al.* (2013).

Equation 3.12, 3.13 can be expended to an arbitrarily order (n) with

$$\gamma_c^{(n)} = \epsilon^{(n)}\,\eta_{occ}^{(n)}\,\Delta\nu\left(\frac{A\Omega}{\lambda^2}\right)\tau_{int} \tag{3.19}$$

and

$$\gamma_{uc}^{(n)} = \epsilon^{(n)}\,\eta_{occ}^{(n)}\,\Delta\nu^{(n)}\left(\frac{A\Omega}{\lambda^2}\right)^{n}\tau_{int}\,\tau_{det}. \tag{3.20}$$

Computing the $\frac{S}{N}$ using $\gamma_c^{(n)}$ and $\gamma_{uc}^{(n)}$ produces

$$\begin{aligned}\frac{S}{N}^{(n)} &= \frac{\gamma_c^{(n)}}{\gamma_{uc}^{0.5(n)}} \\ &= \epsilon^{n/2}\,\eta_{occ}^{n/2}\,\Delta\nu^{(1-n/2)}\left(\frac{A\Omega}{\lambda^2}\right)^{n/2}\left(\frac{\tau_{int}}{\tau_{det}}\right)^{0.5}\Gamma^{(n)}.\end{aligned} \tag{3.21}$$

As expressed in Section 3.4.1, the occupation number can be rewritten in terms of the stellar magnitudes with since

$$\left(\eta_{occ}\frac{\Omega}{\lambda^2}\right)^{n/2} = \left(\frac{\lambda}{20}2.512^{m_x}F_x\right)^{n/2}. \tag{3.22}$$

.

Placing the relationship from Equation 3.22 into 3.21 yields

$$\frac{S}{N}^{(n)} = \epsilon^{n/2}\;\Delta\nu^{(1-n/2)}\left(\frac{\lambda}{20}2.512^{m_x}F_x\right)^{n/2}A^{n/2}\left(\frac{\tau_{int}}{\tau_{det}}\right)^{0.5}\Gamma^{(n)}. \tag{3.23}$$

Unfortunately, higher order correlations introduce a bandwidth dependency, which has a significant, negative impact on the SNR. While it is feasible to obtain a 3rd

order correlation when observing very bright stars with large telescopes ($\sim$10 meters), measurements of higher-order correlations appear to be highly improbable in the near future.

It would be interesting to explore this subject matter further, as the scalability of the array with an introduction of additional telescopes is factorial (Equation 2.5). In principle, factorial terms of the number of baselines grow faster than power terms. After a certain point though, the number of available photons within the coherence time is going to make higher order detection nearly impossible. However, an introduction of additional telescopes essentially amounts to having one large telescope with segmented mirrors. However, at what point such turnover occurs is beyond the discussion presented in this thesis.

Chapter 4

FROM THE STARS TO DATA

Before developing a dedicated single-photon interferometry array, the concept of single photon interferometry should be demonstrated on small to medium (0.5 to 5 meters) sized telescopes telescopes. An ideal observatory would have 1) multiple optical telescopes, preferably in a two-meter class (Section 4.5) 2) accessibility, regarding obtaining observation time and 3) capability for introducing and integrating new photoelectric equipment. There are multiple optical observatories throughout the world which would satisfy this criterion. One, in particular, located at Kitt Peak in Arizona, appears to be very promising. It satisfies all three points stated above, as well as being located a few hours away from Arizona State University [1] , where the test instruments are being assembled and characterized.

The Kitt Peak Observatory has more than 7+ optical telescopes of varying sizes (0.9 to $\sim$ 4 meters) which could provide 21+ different baseline measurements to probe the UV-plain (Section 4.2). The projected baselines vary from a few meters to +650 meters, which allows access to stars of an angular size which are currently unresolved (Section 4.1). Majority of these telescopes are also in the line of sight of one another, placed on elevated platforms (Section 4.4). The weather conditions on Kitt Peak are very favorable for astronomical observations (See Section 4.5). For this reason, the observatory and its telescopes have been chosen to perform a trace study as to what would be achievable from such a site, using commercially available equipment (See

[1] Tempe location

Section 4.6 and 4.1).

4.1 Viable Targets From the Kitt Peak Observatory

The limiting stellar magnitude and precision in measurements of angular diameter from observations carried throughout a night are dependent on the location of the star in the sky. The dependency arises from two factors: 1) The first is that the RA and Dec of the object will determine the projected baselines, and thus the uv-plain coverage over which the measurements will be acquired. Therefore, some measurements of Γ^2, as a function of telescope separation, will vary in precision. 2) The second factor is that the angular size of the object will determine how many baselines are sampled before the first minima in Γ^2 occurs, as well as "redundant" baselines which would allow for tighter constraint of $\gamma^{(2)}$. The data collected along the projected baselines with separations less than the first minimum in $\Gamma^{(2)}$ give the most robust constraints on the derived radii, whereas the measurements beyond the first minimum introduce additional spacial modes, correspond to smaller features on the surface of the star.

As a test case, we simulated a star with the physical diameter of Alkaid but with a magnitude, $m_v = 6$, effectively moving the star further away. Setting the magnitude to $m_v = 6$ was done in order to match the limiting magnitude for objects observed from Kitt Peak for single photon intensity interferometry. By using this new target, the projected baselines remained the same, but the Γ^2 value as a function of telescope separation would change. Since the new object has effectively decreased the angular size of the object, the first minimum would occur past the limit of the I-Int telescope array, with $\Gamma^{(2)}$ values ranging from 1 to $\sim$0.2. Additionally, the error in each measurement will be higher than for actual Alkaid since it has been made cooler, significantly decreasing η_{occ}. With 10000 simulated, 8-hour observations of

this source (using the 7 Kitt Peak telescopes), the variance in the measured angular diameter of the star is about $\sigma = \pm 1.16\%$. Since the stellar distances are known to a higher precision than 1%, $m_v = 6$ would appear to be a reasonable threshold for target selection. Anything dimmer would be difficult to justify, with regard to time investment, and there is no shortage of stars that are brighter available for observations from Kitt Peak.

The potential target stars brighter than m_v =6 were identified from the list of the Bright Star Catalogue (Hoffleit and Jaschek, 1991). At first, all binary star systems and stars with Dec $\leq$ -30 degrees were eliminated from the set. The brightness for binary stars would be too time-consuming and have to be dealt with on a case by case basis while contributing little to already large dataset. The stars with Dec $\leq$ -30 degrees do not rise significantly above the horizon line. The final sample contained 3207 stars. Their angular size was approximated based on the spectral type, from O to M, and sub-type 1-9.

Two categories of stars were created: stars that would be fully resolved and partially resolved. The fully resolved stars are defined as those whose angular size is large enough such that the first minimum of $\Gamma^{(2)}$ would fall within the projected baseline limit. The partially resolved stars were defined such that $\Gamma^{(2)}$ would fall within two times the projected baseline limit. It is possible to derive the angular size of partially resolved sources, albeit with additional uncertainty, since the signal to noise will be higher where values of $\Gamma^{(2)}$ are closer to 1. These constraints narrow our sample size to 3121 stars, 2378 of which would be fully resolved and 743 would be partially resolved.

The angular size as a function of the magnitude and spectral type are present in Figure 4.1. Table 4.1 summarizes the results and further breaks it down by spectral type and by magnitude. Additionally, comparison to the state of the art amplitude

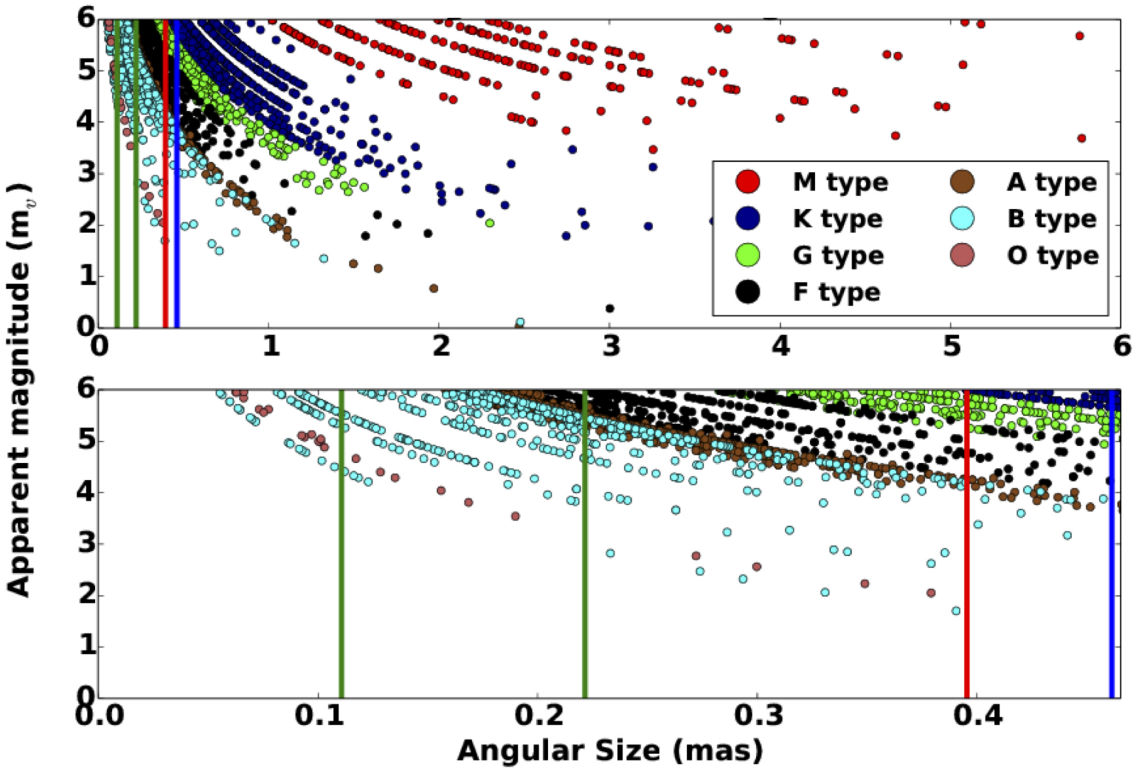

Figure 4.1: Top: Stellar magnitudes from the Bright Star Catalogue plotted as a function of their approximate angular size. The colors correspond to the spectral type, given in the legend. Bottom: Identical plot, with a narrower range in angular size, showing the bounds where observations from Kitt Peak can fully resolve the star ($\sim$ 0.21 milli-arcsec) and bounds where stars will be partially resolved ($\sim$ 0.11 milli-arcsec).

interferometer CHARA is made, in terms of overlapping objects.

Table 4.1: Stars, according to their spectral type (top) and apparent magnitude (bottom), observable from Kitt Peak.

Spectral type	Number of fully resolved stars	Overlap with CHARA	Number of partially resolved stars
M	230	230	0
K	729	726	0
G	424	282	0
F	431	118	52
A	364	77	348
B	205	44	328
O	4	0	6
Total	2387	1450	734

Apparent Magnitude	Number of fully resolved stars	Number of partially resolved stars	Approximate integration time[1]
$\leq$1	7	0	$\ll$ 1h
1 to 2	18	0	$\ll$ 1h
2 to 3	76	0	$\ll$ 1h
3 to 4	199	5	0.2 h
4 to 5	667	52	1.24 h
5 to 6	1420	677	8 h
Total	2387	734	

[1] in order to obtain angular size measurement with precision of $\sim$10%

4.2 UV-plane Coverage from Kitt Peak

Stars can be modeled to a first-order as circular apertures. Assuming they are perfectly round and uniform across their surface, the diffraction pattern in the uv-plane will be that of an Airy disk, a first-order Bessel function. The angular size will determine where the first minima will fall; deviation from a perfect circle, i.e., obliquity due to the rotation will distort the Airy disk pattern, making it more oval like in appearance. Surface features, such as star-spots, as well as stellar winds, will affect the higher order maxima.

By changing the distance between the telescopes, different portions of the uv-plane are sampled. The Earth's rotation further modulates the parameter space over which the sampling occurs. The "projected" separations between the telescopes vary as the star rises-sets and depends on the orientation of the baselines between telescopes on the ground.

A routine to calculate the uv-plane coverage from an arbitrary array of telescopes, of varying size and corresponding visibilities for the different baselines given a template star, was designed in Python language. The routine works under the assumption that the star is spherically symmetric with no limb darkening or any other features such as starspots and stellar winds. This assumption significantly simplifies the complexity of the model with little fidelity loss in the computational model. The complex visibilities (complex amplitudes) along the x- y-plane, are obtained by taking the Fourier transform of the sky image. The assumption is that the star of interest is the only object in the sky, and the background noise levels are minimal. The complex visibilities are then multiplied by their complex conjugate to give the expected correlated intensity signals for a given pair of telescopes.

Some of our closest stellar neighbors, especially the main sequence giant stars,

Table 4.2: Telescopes on Kitt Peak which were used in the simulations. The latitude, longitude and elevation are presented as an offset from 31.9°, -111° and 2000 meters.

Name	Telescope Diameter (m)	Latitude offset (10^{-2}) (degrees)	Longitude offset (10^{-1}) (degrees)	Elevation (m)
Mayall	4.0	6.40	-6.00	88
WIYN	3.5	5.80	-6.00	90
WIYN	0.9	5.80	-5.99	87
KPNO	2.1	5.82	-5.98	86
Bok	2.3	6.29	-6.00	71
SW	1.8	6.16	-6.00	75
SW	0.9	6.19	-5.99	91

can be resolved with huge telescopes and adaptive optics system (10+ meters) or using interferometers with dish separation that is on the order of tens of meters. However, a majority of the visible main sequence stars falls outside of this range, requiring telescope separation that is on order $\sim$100's of meters. Since the projected baseline is $\gg$ diameter of the telescope, we can simplify our simulation by making the assumption that the variation in flux across the telescope dish can be neglected and our *telescopes* can be considered point-detectors in the *uv*-plane. The beam pattern of the telescopes, as well as their combined beam pattern, can be ignored.

The *uv*-plane coverage is calculated for the telescope array using their latitude, longitude, and elevation as inputs. Combining seven different telescopes located on Kitt Peak yields 21 unique baselines.Table 4.2 gives the location, size, and the name of the telescopes used in this model.

The projected baseline between two telescopes is determined by the RA and DEC

of the target and varies as a function of time due to the Earth's rotation. This information can be obtained by using the coordinate transformation matrix from Ségransan (2007) and provides us with u, v, and ω -baselines. The variable ω corresponds to elevation difference in telescopes in frequency space. It is useful to think of it as a temporal offset, which will change the location of where the correlated intensity peak, $\Gamma^{(2)}$, is located in the histogram. In our simulation, the value of ω varies as much as 4 meters during one minute. It is therefore vital to correct for the value of ω for a given target-telescope pair on a scale of milliseconds in order to avoid smearing the signal across multiple bins.

Additional constraints on our observations which were 1) the target will only be observed if it is above 20 degrees from the horizon and 2) the hours of the observation must be between 9 p.m. and 5 a.m., for a single night.

The simulation package utilizes the PyEphem routine which allows the user to enter the location of each telescope as well as the location of the stars in the sky as a function of time. The local coordinates of the star, as seen from each telescope throughout the observing period, are thus generated. The coordinates are incremented at one-minute intervals, along with the targets RA and Dec positions. Shorter time increments have been tried, but additional computational time is not justifiable by a small increase in the precision of the model.

The projected baselines are superimposed onto the generated *uv*-plane (see Figure 4.2). The intensity at each projected baseline is measured and normalized by the maxima to yield the expected correlations function value (see Figure 4.3) from which the angular size of the star can be derived by fitting first order Bessel function and minimizing the residuals. The physical diameter can be derived if the distance to the star is known.

The values from the *uv*-plane for each unique baseline produced in the telescope

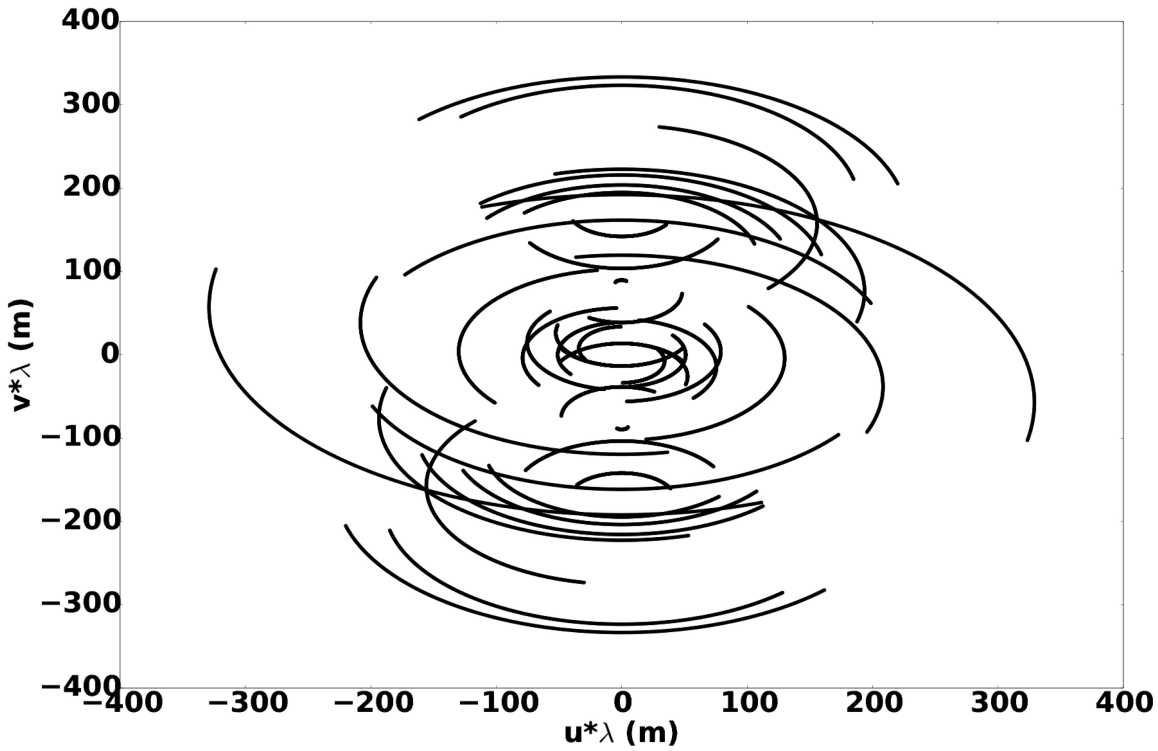

Figure 4.2: Plot representing the 21 unique sweeps of uv-plane performed by seven different telescopes at Kitt Peak while observing Alkaid throughout the night.

array are stored, which allows for further analysis to determine favorable configuration of telescope pairs to use for a given target; If the additional measurements are necessary to constrain the $\Gamma^{(2)}$, a follow up observation can be made using just a pair, as supposed to the entire array. As an example target star, Alkaid, one of the brightest stars in the sky at (m_v=1.8) was used. Table 4.3 gives additional parameters of the star used in this simulation.

The quantum efficiency of the detector was assumed to be ∼70%, based on common values in the commercially available SPADs. Under the assumption that there is photon loss in the optical system as well as in the telescope-fiber-detector coupling, the entire system efficiency was set to 50%. The central wavelength at which our simulated observations were carried out was set to be 650 nm since that is the peak of the

Table 4.3: Alkaid (Eta Ursae Majoris)

m_v	1.84	Ducati (2002)
RA	13:47:32.43	van Leeuwen (2007)
DEC	+49:18:47.76	van Leeuwen (2007)
Distance (m)	$9.868(10^{17})$	van Leeuwen (2007)
Radius (m)	$2.365(10^{9})$	Underhill *et al.* (1979)
Temperture (K)	16823	Underhill *et al.* (1979)

quantum efficiency for the majority of the detectors. The projected baselines created by the seven telescopes in this simulation varied from 30 to 650 meters, throughout the night. The baseline of 650 meters corresponds to the angular resolution of $\sim$0.25 milli-arcseconds.

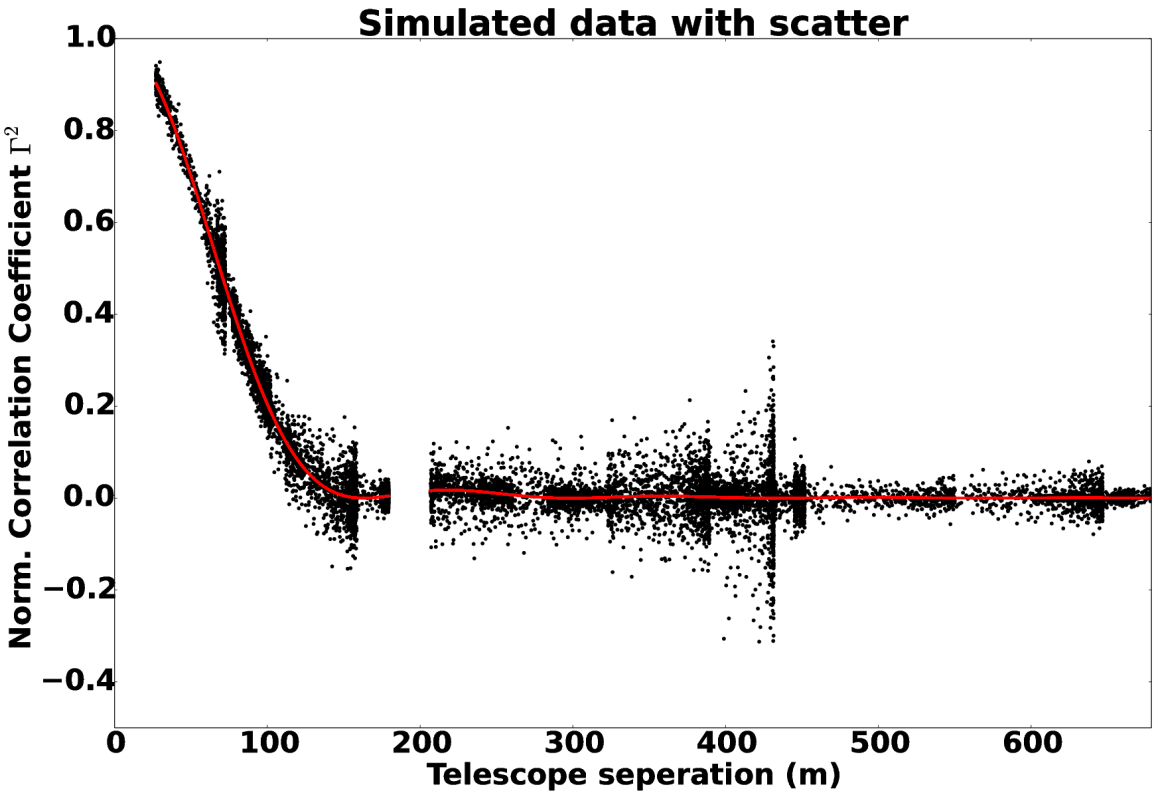

Figure 4.3: Simulated Γ^2 window coverage for Alkaid. Scatter was introduced based on the errors from each point. The variation in the range of the scatter produced is due to the different size telescopes combination. The gap at ∼200 m is due to a gap in the *uv*-plane coverage. Red line represents the best fit of a Bessel function through minimization of the residuals.

4.3 Time bin shift

The difficulty of measuring $\gamma^{(2)}$ over the course of a single night is further augmented by the changes in the telescopes spacial location, relative to that of the star. As the Earth rotates, projected baselines of telescope pairs "move", and sample a larger area in the UV-plane. With a wider coverage, more values of $\gamma^{(2)}$ at different baselines are obtained, at the expense of higher signal to noise ratio for a given telescope separation.

The projected baselines spacial coordinates change, but so does their "temporal" location, due to elevation and proximity to the star. While this change is small, it is not subtle enough to be ignored. As described in Section 4.2, a model of changes in the ω component can be constructed in order to mitigate the temporal drift of $\gamma^{(2)}$.

The change in elevation as a function of time $\Delta\omega$ can be translated to a temporal shift in the histogram of photon arrival times, $\frac{\Delta\omega}{c}$. Examining the change in elevation $\Delta\omega$, as a function of time, for all unique baselines (Seed Figure 4.4, has shown that for certain telescope pairs, $\frac{\Delta\omega}{c}$ is very large. The biggest culprit varies by as much as 6 ns every 15 seconds. The time variation suggests that with τ_{det} of $\sim$300 ps timing resolution, the expected bin will change every $\sim$ 0.7 seconds. A single pulse every second from a GPS based clock source should be more than sufficient to keep track of this information so that the data processing can compensate for the drift. The synchronization is further discussed in 4.4.

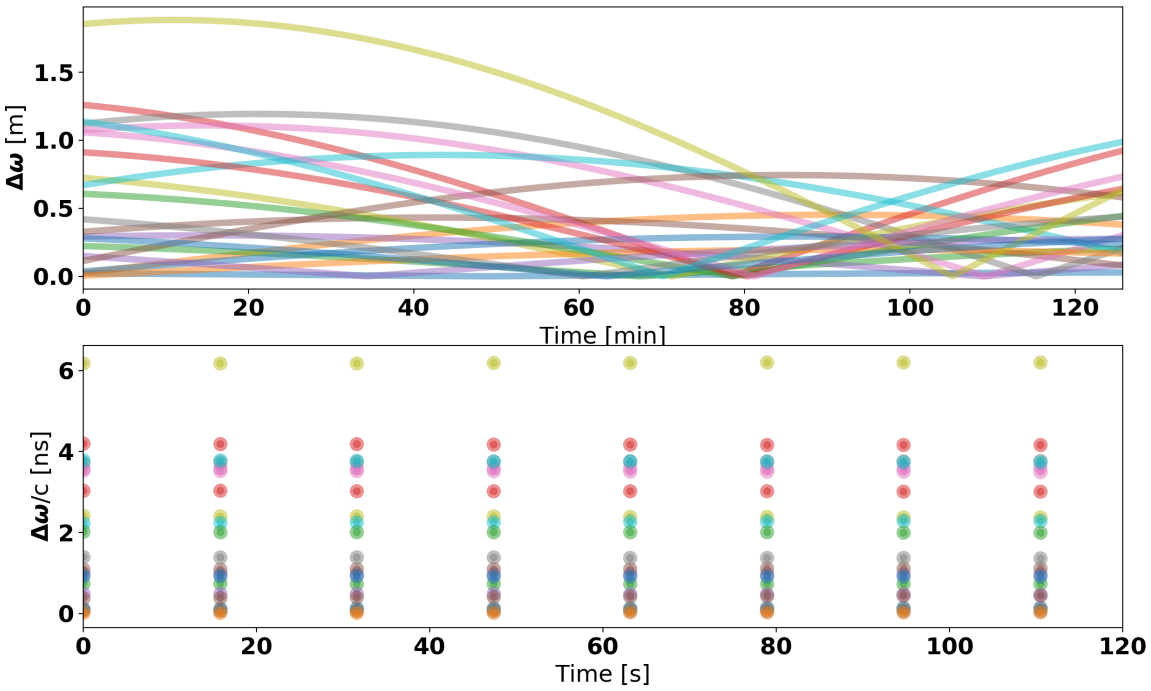

Figure 4.4: Top: Change in the telescopes elevation $\Delta\omega$, as a function of time, in minuets. Different colors represent different telescope pairs, 21 in total. Bottom: Zoomed in version, showing the time bin drift ($\frac{\Delta\omega}{c}$), in nanoseconds, over a course of 120 seconds.

4.4 Synchronization of the Decoupled Telescopes

Since the signal can be processed after data acquisition and correlated with software, telescopes in an I-Int array can be, in principle, separated by arbitrarily large distances. The underlying assumption here is that the time of arrival of each photon is given in reference to an "absolute time", which is not the case. The clocks at different locations will drift over time and become out of sync. Perturbations in the phase of the local oscillators cannot be entirely removed, and become exaggerated if proper temperature control is not established. Since placing cables or optics fibers between telescopes on Kitt Peak is not a viable solution, and would defeat the signif-

icant motivator behind intensity interferometry, the synchronization will need to be performed via free-space signals from a common clock reference source.

A straight-forward solution of using a standard reference clock can be achieved using a commercially available GPS receiver which produces a pulse per second (PPS). This pulse could be sent to the multiple TDCs to provide a common reference point between the units. This method has been proposed and simulated in Horch (2015), based on the observation that the two clocks in different TDCs (Hydroharp and Picoharp) drifted from one another by about ~ 300 μs per second. Two constraints need to be met. The local clock must be reset at timing intervals such that the drift is less than the timing resolution of the detectors; in this case, the PPS would need to be converted to a $\sim$ 1MHz signal to achieve a reset every 300 ps. Additionally, the timing precision of the GPS signal needs to be on the order of the timing resolution of the detectors. Commercially available GPS units can obtain precision in the $\sim$10 ns. However, it is possible to obtain a more precise timing solution after the fact, once the orbits of the GPS satellites are better-known Ray and Senior (2005) through an updated orbital parameter model. In principle, GPS timing on the order of hundreds of picoseconds is possible since the data is stored digitally and does not require a real-time solution. However, this approach with SPADs and TDCs has yet to be demonstrated.

In addition to GPS synchronization, another viable solution is through free-space, a line of sight optical/microwave combination. Optical cavity-stabilized lasers have provided synchronization across a turbulent atmosphere with the stability of 40 fs over the course of days (Deschênes *et al.*, 2016). Similar precision (13 fs) has been achieved using a combination of microwave clocks separated by 4 km driven by an optical master clock by Bergeron *et al.* (2016). Since the level of precision provided by local clocks is several orders of magnitude better than what the current SPADs

technology can achieve, incorporating this into the setup would allow the telescope array to be detector limited in terms of the timing resolution.

4.5 Optimal Telescope Size and the Affects of Seeing

While atmospheric effects do not contribute to the noise directly, turbulent mixing of the atmosphere will affect the spot size of the star through random jitter (i.e., seeing) of the point spread function (PSF). The central location of the PSF will vary on the millisecond timescales as the path-length between the top of the atmosphere, and the telescope, shifts. This effect is due to the light transversing "cells" of varying density, acting as a small lens. The result is broadening of the PSF. Therefore, if the effective area due to seeing projected on the image plane is larger than the area of the fiber coupled to the telescope, the efficiency of the system will decrease as the ratio of the two areas.

The plate scale of the telescope (P_s), in units of arc-seconds per mm, can be written as

$$P_s = \frac{206265}{D \times f} \quad [\text{arcseconds/mm}], \tag{4.1}$$

where D and f represent the diameter and the focal length of the telescope, respectively. In order to maximize the efficiency of the system, P_s needs to be higher than the effect of atmospheric turbulence so that all of the incident light can be fed into the detector via fiber cable. While the telescope diameter is fixed, focal length reducers can be used in order to increase the field of view if the seeing is inadequate.

The seeing on Kitt Peak varies nightly, and the coupling efficiency will thus be different for each telescope. By using detectors with active areas of 200 μm $\times$200μm, a threshold can be derived where the effects of seeing are inconsequential. With seeing of 1.5 arc-seconds, not uncommon for a good observing night at Kitt Peak, all telescopes under consideration will not take a hit in efficiency. For almost all

telescopes, seeing of 2 arc-seconds will be sufficient, if the observations are carried out with 10 nm bandwidth or less. The results are shown in Figure 4.5.

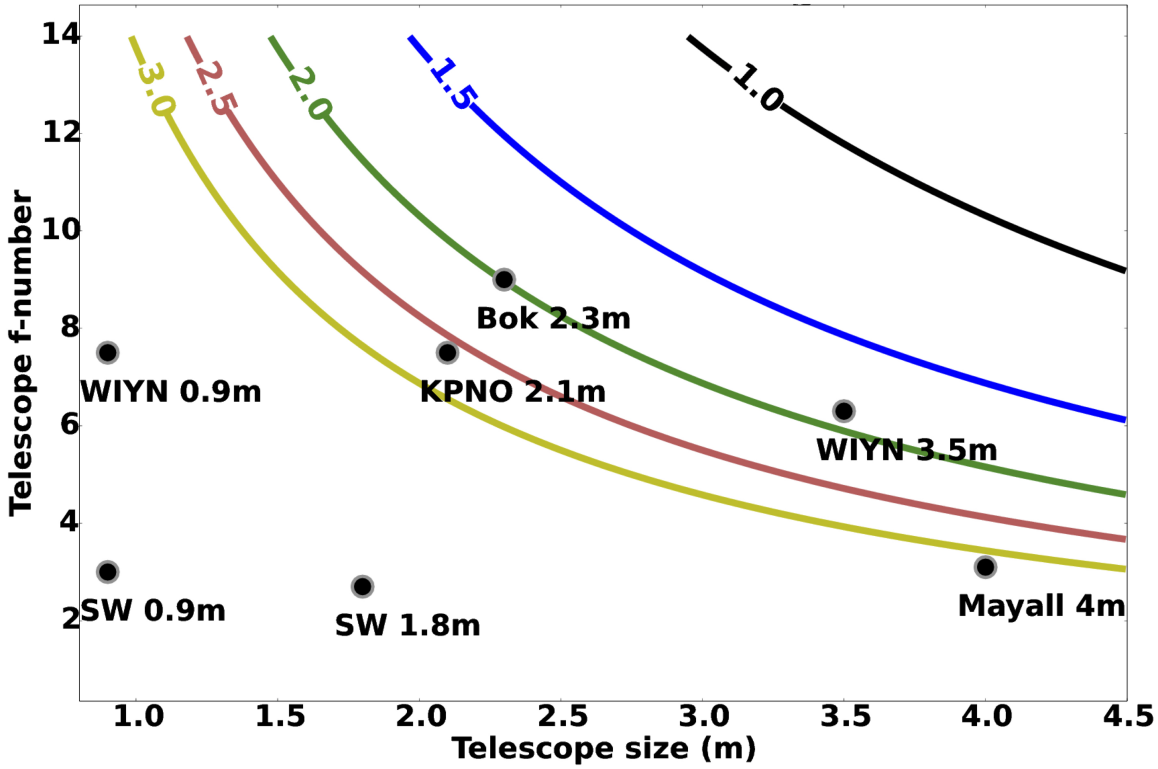

Figure 4.5: Contour plot displaying the plate scale in arc seconds per 200 μm as a function of the telescope f-number and the diameter. The black dots represent the seven telescopes at Kitt Peak used in our simulation. The observed light is assumed to be narrow-band

4.6 Telescope to SPAD coupling

In order to achieve telescope to SPAD coupling, the light collected by the telescope will need to be channeled into a fiber, which should be placed at the imaging plane. The diameter of the multi-mode fiber is closely matched to the active area of the de-

tectors to minimize photon loss. For the majority of multimode fibers, the acceptance angle will be larger than the angle of the light rays coming from the telescope.

The length of the fiber could be $\lesssim$ meter if the detector is not mounted directly onto the telescope, which would be a less invasive approach for coupling to existing telescopes. In this case, the remaining components of the set up would be placed in the vicinity of the telescope. A 10-meter fiber should provide sufficient slack as the telescope moves to/from the target star or tracks it throughout the night while attenuating a negligible number of photons. Since the movements of the telescope will be slow while tracking, the telescope operator can adjust the fiber to avoid bending it to a critical angle where a break can occur. The light would then be passed through a collimator and narrow band filter to a commercially available SPAD. Alternatively, the entire setup could be mounted onto the telescope, removing the need for fiber. The incident light can then fall directly onto the detector, assuming it has been placed at a correct focal length.

The SPAD would produce an electronic pulse upon successful photon detection. The signal would travel along high fidelity SMA (preferred) or BNC cable to a TDC. The electronic pulse would then be "time tagged" by a TDC module, and the data would be stored on a hard drive. The TDC units at different telescopes should be synchronized via local crystal oscillators which provide short time stability, and GPS or optical cavity for long term. A summary of commercially available SPADs and TDCs is given in Table 3.2.

[2]250 ps is available for a TTL output, while the 50 ps option is for a NIM output type.

Table 4.4: Commercially Available SPAD units

Manufacturer	Name	Timing Resolution (ps)	Peak efficiency (%)	Dead time (ns)	Active area μm	Max Count rate MHz
Excelita	NIR-12	350	70	20	180	40
Micro Photon Devices	PDM	250 or 50^2	49	77	100	unknown
Laser Comp.	Count S	1000	70	45	100	0.5
	Count T	350	75	45	100	20
IDQuantique	ID120	400	80	1000	500	unknown

4.7 Readout Electronics

As discussed in Chapter 2.3, viable backend electronics for time tagging photons is an ongoing field of research, driven by the need to have accurate time of arrival measurement. In the scientific community, such devices are used for 1) Time of flight measurements 2) High energy particle physics and 3) Quantum Key distribution and encryption and of course 4) Single photon interferometry. In the commercial world, time to digital converters (TDCs) provide support for things 1) LIDAR, which maps out environments through what amounts to as beam tracing, 2) Bioluminescence and Ramen spectroscopy, 3) Decay of particles 4) Quantifying performance of Micro-Opto-Electro-Mechanical Systems. The availability of TDCs for commercial purposes allowed for of the shelf components to be integrated into a I-Int array. The list of a few commercially available products, as well as some key parameters is listed in Table 4.5.

Laboratory test and instrument characterization proved to be disappointing. Un-

Table 4.5: Commercially Available TDCs Units

Manufacturer	Name	Timing Resolution (ps)	Max Rate (MHz)	Number of chan.
Voxtel	YVX-657	32	25	8
Picoquant	HydraHarp	1	12.5	2-8
Picoquant	PicoHarp	4	10	2
IDQuantique	ID800	81	2.5	8
Laser Comp.	quTau	81	3	8

fortunately, the instruments listed in Table 4.5 were often designed to function over relatively "short" timescales, on the order of milliseconds. While the quoted event rate can be in the MHz range, these rates are unsustainable. A couple of models had a duty cycle, often the "on" state lasting only 10% of the time, and "off" state where the data is being transmitted/stored occupying the remaining 90%. Such duty cycles significantly hinder the overall system efficiency and changing the required integration times by one to two orders of magnitude. In a passive measurement and a photon-starved regime that I-Int. is operating, a non-continuous readout is a deal breaker.

Onboard processing was another issue that has been encountered. The processing of data by the hardware acted as a black box, and in an environment where the entire optoelectrical system of Telescope-SPAD-TDC performing astronomy measurements has yet to be proven to function, becomes a hindrance when debugging, troubleshooting and calibrations are performed. Furthermore, units with onboard processing tend to have an associated cost per channel in the 10k range, making them very expensive for a large scale implementation.

The more cost favorable units, of about 1k per channel, tended to have internal crosstalk. Although not proven, it is hypothesized that this effect occurred due to TTL to LVDS converter chips placed at the front end of the FPGA. It was observed that channels which shared the same converter chip had significantly higher cross talk value, to the degree that the expected correlated photon signal is expected to be covered by the instrumental noise. The effect is shown in Figure 4.6. The noise was determined to grow linearly with time, which means no amount of integration time would allow for successful detection of the temporally correlated photons. This issue served as an inspiration for designing and building a special TDC for intensity interferometry with control over the firmware and software, which is discussed in great detail in Chapter 5.

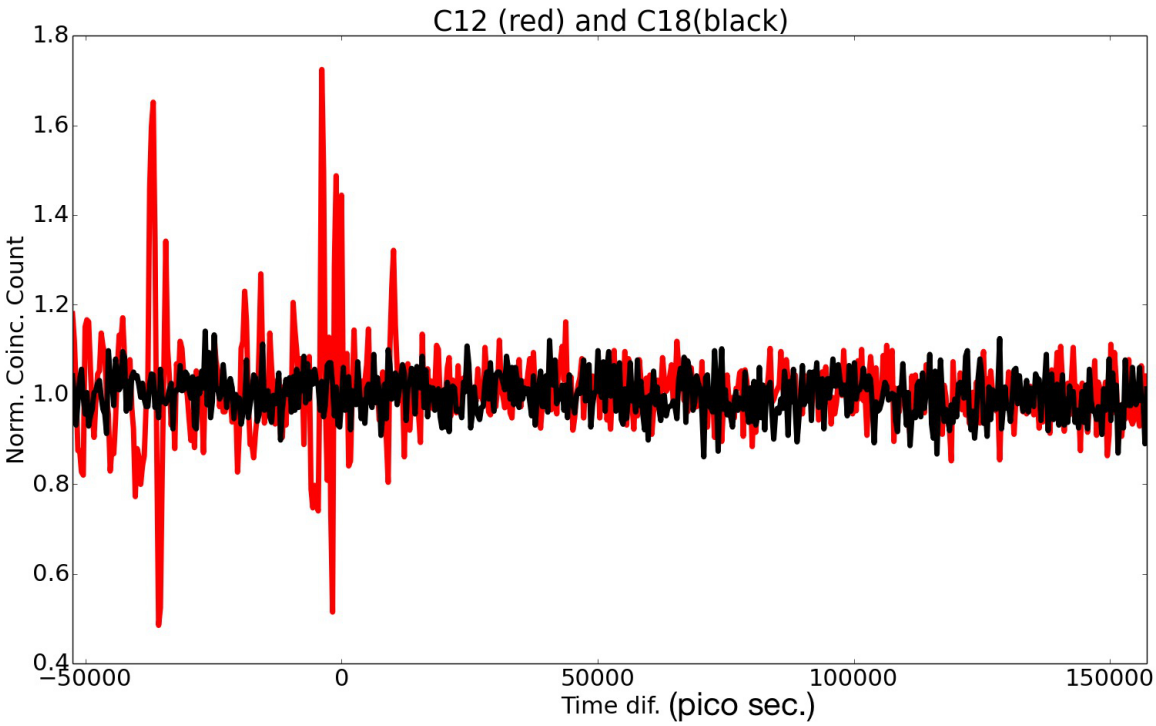

Figure 4.6: Normalized coincident photon arrival times for two channel pairs. Uncorrelated light (two sources) were used to illuminated the detectors. Channel 1 and 2 (red) shared and LVDS converted while Channel 1 and 8 (black), did not. The integration time and photon count rate was kept constant for both measurements.

Chapter 5

READOUT ELECTRONICS AND DATA ANALYSIS

At first, this project was focused on utilizing commercially available equipment to achieve a demonstration of single photon interferometry. However, as it progressed, the bottleneck in the system occurred with the readout electronics, forcing a custom solution. Multiple approaches were considered, but ultimately, a time to digital converter (TDC) was chosen as the readout solution since the performance and architecture is, at this time, best suited to tackle the problem of time tagging (Section 5.1). The TDC was implemented on a commercially available board (Section 5.2), using custom firmware (Section 5.3) and software (Section 5.4 and 5.5) for data analysis. Here we present a characterization of a time-to-digital converter (TDC) based on previous work of Sinclair *et al.* (2016) with improved timing resolution and number of input channels.

5.1 Background

Measurements with timing precision in the tens of picoseconds can be achieved by multiple means, such as high-speed analog-to-digital converters (ADC), TDC chips, and recently, FPGAs. The data output from ADC sampling at high rates is unnecessary for this application since we are only interested in *when* an event has occurred. It is possible to design a discriminator, which only outputs data when a certain critical threshold has been achieved, but this would require the development of a custom board. Similarly, a TDC chip requires complex readout electronics, often coupled to an FPGA board in order to do some data processing.

Progress in FPGA development has been steady over the course of the last few

decades. The on-board logical elements can be driven at frequencies of hundreds of MHz, allowing for coarse timing resolution to be on the order of only nanoseconds. However, inputting a signal into the FPGA asynchronously, relative to the onboard clock, allows the timing resolution to increase by two orders of magnitude, down to tens of picoseconds. Multiple approaches have been demonstrated, such as using single or arrays of delay lines, tapped delay line Narasimman *et al.* (2015), Vernier Delay line Gao *et al.* (2011), ring oscillator, pulse shrinking delay line and measurement matrix Zhang *et al.* (2017). The differences, advantages, and disadvantages of these implementations are beyond the scope of this paper, and the reader should refer to Soni *et al.* (2017) for a comprehensive review.

The basic delay-line is the easiest to implement and can achieve a timing precision that is small, compared to the typical single photon detector timing resolution of ∼350 ps. The adaptation of this design is further discussed in Section 5.3.2, along with supporting firmware.

5.2 Hardware

5.2.1 ROACH2 FPGA Board

The developed TDC firmware is implemented on the the Re-configurable Open Architecture Computing Hardware Revision 2 (ROACH2) CASPER (2013) platform. The board, as well as some of the MATLAB/Simulink/VHDL wrappers, have been developed by Collaboration for Astronomy Signal Processing and Electronics Research CASPER (2009). The FPGA is a Xilinx Virtex-6, which has been donated to us by Xilinx, Inc. The options for signal input to the FPGA chip available to the user are composed of 8 GPIO pins, sync in, sync out, aux clock and 2 Z-Dok connectors. The board also contains a PowerPC for easy control, interface, and operation such as

uploading the FPGA binary file and sampling data via Python scripts. There are two options available for data output: 1) a 1Gb Ethernet port which is currently being used to test and characterize the board and 2) two slots for a multi-gigabit transceiver mezzanine card, which would allow transfer speeds of ∼10 Gb per second. The board is shown in Figure 5.1.

Multiple inputs have been tested, with varying degree of success. The GPIO pins proved to be adequate for testing out the firmware. However, because GPIO pins were not designed for high-frequency inputs on of GHz frequencies, the S-parameters are not may not be matched well enough to avoid reflections at the interfaces. The aux clock, as well as sync in and out ports, limit the number of inputs to 3 and eliminated dedicated lines which are meant for synchronization. Using the Z-Dok inputs would be the most cost effecting solution, allowing for dozens of independent channels per single board to be used in photon counting experiments.

5.2.2 LVTTL to LVDS Z-Dok Board

The Z-Dok connector has 40 pins, which allows multiple signals to enter the FPGA. A custom interface board had to be built, as commercial Z-Dok to SMA boards have not been found. The custom interface board to convert a TTL signal from an SMA input to an LVDS signal directed into the Z-Dok port using an LVDS Differential Driver (part number DS90LV011AQ). This chip was chosen due to its low cost and transition time, high to low and low to high voltage, matching that of the SPAD. The maximum operating frequency of 250 MHz is a factor of 25 more significant that the expected photon count rate per channel, meaning the chip will never become saturated with photons and function in a predictable routine.

Currently, 10 different input pins have been placed and tested, with the goal of expanding it to 32 different inputs per Z-Dok port. As seen in figure 5.1, there is

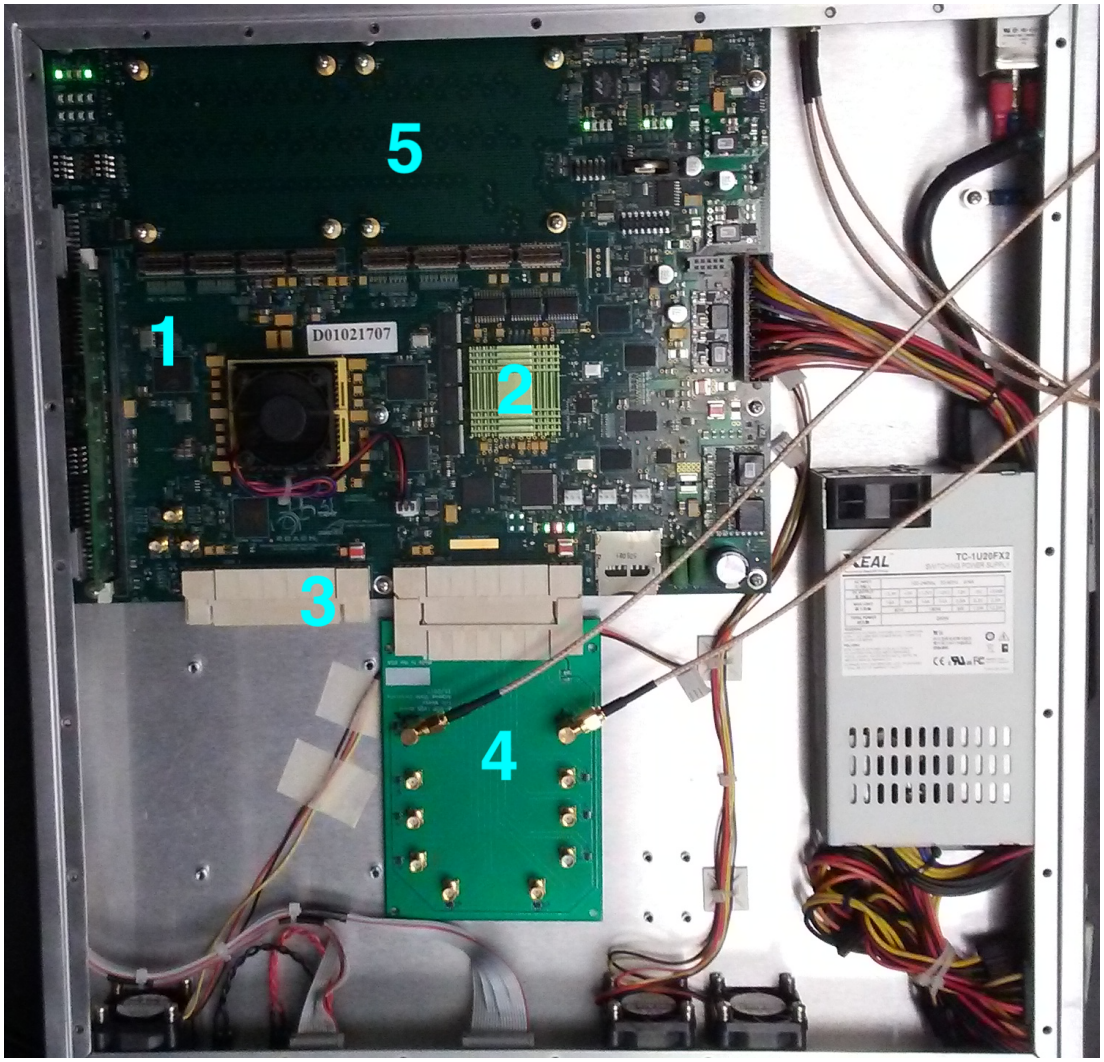

Figure 5.1: Image showing ROACH2 . (1) The Virtex 6 FPGA chip, under a cooling fan. (2) Power PC, which allows for communication with the board. (3) Two of the ZDOK connectors, with (4), a custom SMA to LVDS converter board. Designated Mezzanine Card slot (5) is available to increase data transfer rates from 1Gb to 10Gb.

enough area left on the board to place another dozen or so channels, and with room to make it longer for remaining channels.

Since there are two Z-Dok connectors on the ROACH2 board, so it is possible to

achieve 64+ independent channels per ROACH2 board. Such a setup would allow for observations of multiple optical bands per telescope, further increasing the signal to noise since each band constitutes a different measurement. With 64 unique channels, a mezzanine card will need to be used for a 10Gb bus since the 1Gb port will most likely not be able to keep up with high photon rates.

5.3 Firmware

The developed firmware used to time tag incoming TTL pulses consists of 5 components. The input filter shrinks the incoming pulse to a clock cycle or less in order to avoid multi-counting a single event. The CARRY4 chain acts as a delay line allowing sub-clock resolution, base on how far the propagating pulse has transversed before synchronous [1] readout of all the components. The bubble filter removes the effects of non-linearity within the CARRY4 elements which are due to the manufacturing processes. The encoder translated the output of the CARRY4 delay chain from 512 to 9 bits; because the propagation is linear, in theory, only 512 values are possible. The dual ping-pong buffer allows for continuous operation by iterating between read-only and write-only states. A simplified block diagram of the firmware is shown in Figure 5.2 and the following sections are used to describe each component with greater breadth.

5.3.1 Input filter

The input filter, based on the publicly available code from Homulle (2015), serves two purposes, 1) to shrink the incoming pulse down to a clock cycle or less and 2) allowing the placements of the delay line to be anywhere on the chip, thereby giving flexibility since the delay line does not need to placed close to the FPGA input pin.

[1] as synchronous as possible within the FPGA clock line path differences

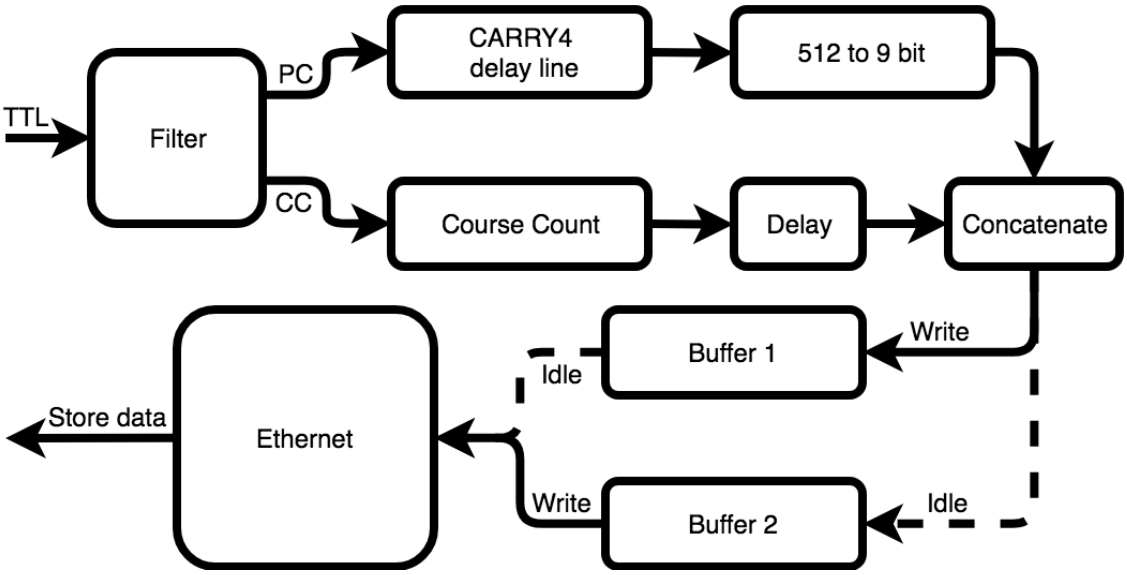

Figure 5.2: Block diagram representing the firmware of the TDC. The TTL pulse produced by the SPADs enters the FPGA asynchronously, filtered and split into two lines for a precision counter (pc) and corse counter (cc). After signal processing, the two time-stamps, pc, and cc, are concatenated along with the channel number. Two ping-pong buffers are used to pass the data to an ethernet block, which passes UDP packets to a data acquisition computer for storage.

The filter consists of two FDR primitives (D flip-flop), with the input pulse entering *asynchronously* into the *clock* port of the first FDR. The output of the first FDR is fed back into the reset port of the first, as well as into the second FDR. This feedback shrinks the pulse, and the asynchronous reset of the second FDR block changes its output from high "1" to low "0"; an inverter is placed right after the output of the second FDR in order to ensure that a high value of "1" only exists if the second block has been reset. The signal is split into two, and the asynchronous pulse then propagates along the delay line, placed on the neighboring slice as well as to a coarse counter. Because this operation is not tied to the internal FPGA clock, it does not

get “lost”, ensuring that every photon detected by the SPADs will have an associated time tag. However, the first timing bin is larger as the propagation from the filter to the first element in the delay line is longer than the propagation delay between the sequential elements.

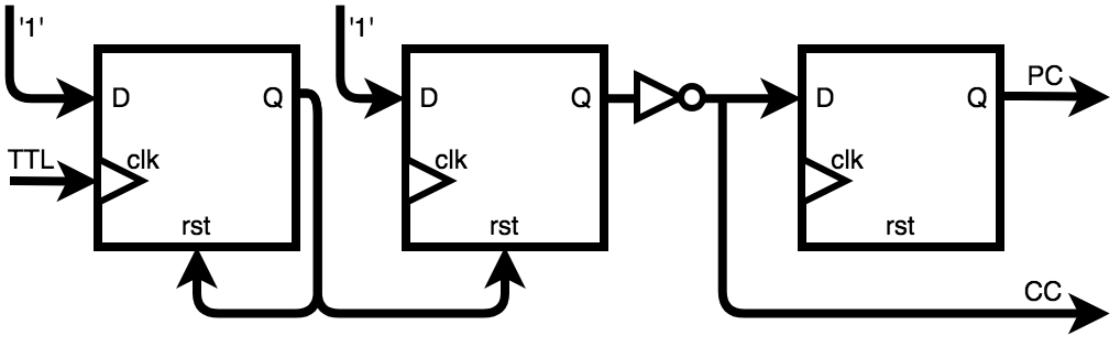

Figure 5.3: Schematic view of the input filter, consisting of 3 FDR blocks. The first two blocks are set to “high” value, and a clock port is used as a trigger. An incoming pulse resets the second block, and the inverted output is passed to a corse counter as well as triggering the CARRY4 delay chain.

5.3.2 Delay line

The delay line consists of 128 CARRY4 primitives, linked in series, with a total of 512 unique outputs tied to FDR blocks. The FDR blocks serve as a “latch” so that an asynchronous pulse can be clocked, and synchronize with the rest of the FPGA logic. The pulse propagates through ∼400 elements before the clock resets the logic. No pulses arriving after 420th element have been observed even during an 8-hour long integration, with 10 MHz photon rate. Since the FPGA clock is running at 200 MHz, each bin in the delay line corresponds to about 12.5 picoseconds.

Unfortunately, it has been observed that some CARRY4 primitives do not yield

an output, potentially due to metastability or manufacturing errors where the "nets" are not linked-up properly to the FDR blocks. This effect is not a unique/random process, but is persistent and affects the same primitives each time. Laboratory tests have shown that a delay line located along a different column of the FPGA chip will have its own unique,"faulty" CARRY4s primitives. In order to mitigate this effect, three unique delay lines per channel were placed in parallel. The output of these delay lines, from the FDR primitive, synchronously enter a 3 port look-up table (3LUT). The 3LUT acts as an OR gate, thereby removing any artifacts that may have been introduced due to faulty CARRY4 primitives. This form of error correction has been observed to improve the precision of the TDC. Additional tests are required to quantify the improvement and will be performed in the near future.

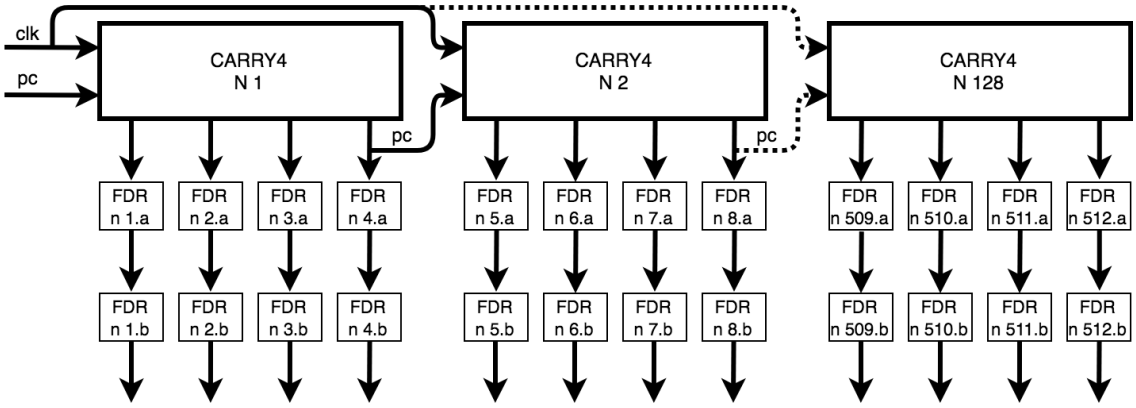

Figure 5.4: A carry chain formed by CARRY4 elements, placed in series. Total of 128 elements are used per delay line, with 512 unique outputs which are stored in an FDR block. The second set of FDR blocks are in place to mitigate affects of meta-stability.

5.3.3 Bubble filter

The propagation along the CARRY4 element to an FDR block has been observed to be non-linear. At times, the 4th element will have a high value, while the 3rd (or less frequently, 2nd) remains low. This effect is most likely tied to the manufacturing process of the primitives on the FPGA since their primary function assumes the digital logic is working with a signal that has been synchronized with the rest of the elements on the FPGA. Such non-linearity can also be temperature dependent, but the ROACH2 board comes with a cooling fan/heatsinks to minimize these effects.

The non-linearity creates additional "bubbles", where low elements of "0's" precede the high elements of "1's". In order to mitigate this problem, the 4 outputs were linked to 4 different 4-port lookup tables (4LUT). They were set up in such a way, that all high values were grouped in the beginning, and any zeros were moved to the end (Example: $0101 \rightarrow 1100$, $1011 \rightarrow 1110$). This particular process was implemented prior to the triple delay line error correction introduced in Section 5.3.2. Future tests will examine if it is necessary or redundant. For now, since the resource utilization for two channels with triple delay line is still under 1%, the bubble filter was kept in the firmware.

5.3.4 Encoder

The encoder is utilized in order to convert 512 available bits to 9 bits to minimize the output data rate. Since the propagation along the line is linear, maximum of 512 unique values can be produced, which can be represented by 9 bits. The implementation of the decoder is achieved with a tree algorithm, allowing for continuous processing, that splits the data into two sets each clock cycle. The middle value of the data set is examined, sending the upper half of the data if the value is high, and

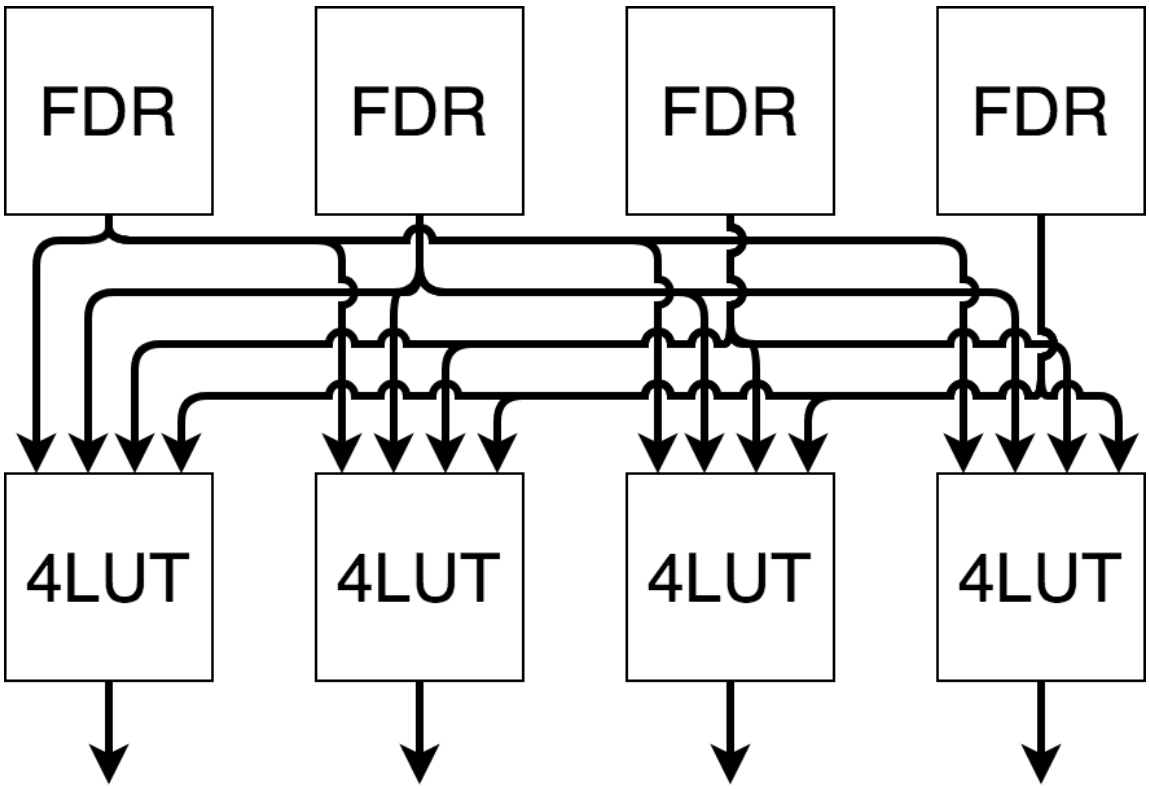

Figure 5.5: The output of 4 FDR blocks are tied to 4 separate look-up tables (4LUT), removing "bubbles" from the delay line outputs. Total of 512 4LUTs were used in the design, per delay channel.

lower half if the value is low. In practice, three steps in the iteration are achieved per clock cycle, and the entire decoding process is done in 3 clock cycles. These bits are then attached to the coarse counter, along with the channel number. This algorithm works under the assumption that non-linear effects discussed in the previous section are removed.

Numerous readout schemes and data formats have been tested, with varying degree of success. In the current operation, the readout utilized 2-9-9-12 bit format, which is optimal for a two-channel TDC. The first two bits represent the channel

number, including coincident hits. The next 18 bits represent the time stamp of the precision counter obtained from the delay line, for channels 1 and 2, 9 bits per channel. The remaining 12 bits are used for the coarse counter, with a roll-over occurring every 20.5 μs. Another configuration for 10 and 64 channel readout can utilize 4 or 6 bits to represent the channel value, 9 bits for precision counting and remaining 19 or 17 bits for the coarse counter, assuming coincident hits are discarded. Photon arrival time can be varied externally, via cables, to compensate for some data loss. Alternatively, 64 bit, rather than 32-bit format can be used. An implementing the 64-bit format with the 10Gb Mezzanine card expansion will be created in the near future.

5.3.5 Ping Pong Buffer

The ping pong buffer uses two DRAM blocks located on the FPGA, in order to allow continuous streaming of the data. At 32 bits deep, and 8192 values long, the out buffer sends 8 bit UDP packets through the Gigabit Ethernet port. The maximum data transfer rate is thus 200 MB, corresponding to 50 MHz total incident photon rate. The limitation in data transfer rate is set by the GbE port, to approximately 25 MHz incident rate. A factor of 10 can be obtained by using a 10 Gb PCI mezzanine card. As the number of channels increases, it is very likely that the data format will need to be changed and optimized.

The outbound buffer dumps its data at every 4 clock cycle, splicing any 32-bit value into 8 bits and storing the raw binary data on an external hard-drive connected to the data acquisition PC. The inbound buffer is continuously writing data and switching the memory index with every new incoming photon, or photons if it is a coincident hit. Once 8192 events have been time tagged, a switch is activated, and the function of the buffer changes. By iterating between the states and the buffers, a

continuous data stream is achieved, and no photons are lost.

5.4 Software

The data pipeline was written in C in order to optimize the processing speed. With each time-tagged photon represented by a 32-bit number and expected count rates of MHz per channel, the expected data rate will be anywhere from 8 MB (2 channels at 1 MHz each) to about 100 MB (upper limit of the Gb bus). This streaming approach allows for large files, sizes of ∼Tb, to remain "open" without filling up the RAM.

The buffer reads 8000 values, performing bit-masking to determine the channel, coarse time and precision time of each photon detection. The analysis of the data and the reading of the data is done out of phase by 4000 buffer elements so that continuous read/analyze procedure is possible with no interruption, mitigating discontinuity effects that would occur if the data is sliced. The data is examined as a single timestamp at a time. If the channel number of the time tag corresponds to the first channel chosen for the analysis, cross-correlation is performed, and a new value read into the buffer. If the channel number corresponds to the second channel in the analysis, no computation is performed, and another value is placed in the buffer.

The cross-correlation is done by first examining the previous time tags. Only the values which came from a different channel are considered. Difference between the two is measured, $4(10^6)$ is added, which determines the index number within an array that was instantiated to 0 for all elements. The corresponding array element gains a +1 to its count current count (initialized to zero), thus forming a histogram with $8(10^6)$ elements corresponding to ±400 ns. If the difference is determined to be larger than $4(10^6)$, or more than 400 elements have been examined, the scan breaks, the position is reset, and a forward scan is performed following the same conditions. The range of ±400 ns was chosen to provide a sizeable temporal window but can be

adjusted in software. The breaks were introduced to increase the performance of the analysis, speeding up the data processing time. Once this is performed, a new value is read into the buffer and the next time tag is analyzed. This process continues until the end of the file has been reached.

If the incident photon rate is ∼12 MHz across all the channels, the analysis can be performed in real time. The performance can be further optimized by implementing parallel processing. Additionally, the window of ±400 ns is unnecessary and was used to quantify and observe the performance of the instrument. The expected location of the signal should be known to a within a few 10's of nanoseconds, thereby increasing the analysis speed by another order of magnitude.

5.5 Post-processing

Although the firmware is designed to compensate for the effects of non-linearity within the TDC, additional post-processing is required on the acquired data to bring forth the signal. In an idealized world, the timing between each element of a CARRY4 element would be 12.5 ps. However, physical path lengths vary, amounting to differential nonlinearities, which means that sometimes, as an example, it takes 10 ps for the signal to transverse between the elements, and 20 ps between the next pair. This effect, referenced to as differential non-linearity (DNL), is deterministic. Therefore, it is common to remove the undesirable feature with an onboard calibration. However, because of large amounts of data gathered for I-Int experiments, *onboard calibration is not required.*

The DNL is different for each channel, and each delay line in the FPGA. However, since only ∼400 bins are affected, with high photon count rate in MHz range and an 8 hour long integration time, the DNL can be characterized. Removal on a channel to channel case is unnecessary. The unique signature of DNL is imprinted in each

channel, and when cross-correlation is performed, the signals from one channel is discretely convolved with the other. Since the new product is contained in each clock bin, a mask can be formulated to remove it, as shown in Figure 5.6, top plot.

Each clock cycle can be thought of as a "frame", containing random uncorrelated photon arrival times and the DNL signature. One or two clock bins will have a smeared signal of correlated photons. Since the correlation is performed across $\pm$400 ns, this yield 80 frames. A master frame is created from an average of $\sim$60 "sub-frames". The discarded sub-frames are those who vary the most of the entire data set. Each subframe is 5 nanoseconds long and contains 400 measurements. This operation produces a mask of 400 elements is then used to remove DNL from each clock cycle. Laboratory tests have shown that the measured standard deviation of the resulting dataset is within 10% of the standard deviation expected from random photon arrivals, and is shown in Figure 5.6, bottom plot. Through this simple procedure, complex digital operations such as convolution and resource hungry onboard operations such as calibration can be by-passed.

After the removal of DNL from the dataset, two additional processes take place. The values are re-binned from 12.5 ps to 25 ps, still an order of magnitude below the detectors timing resolution. A matched filter resembling the expected signal is then used, acting as a bandpass and smoothing out high-frequency spikes as well as low-frequency drifts. The results are discussed in Chapter 6.4.

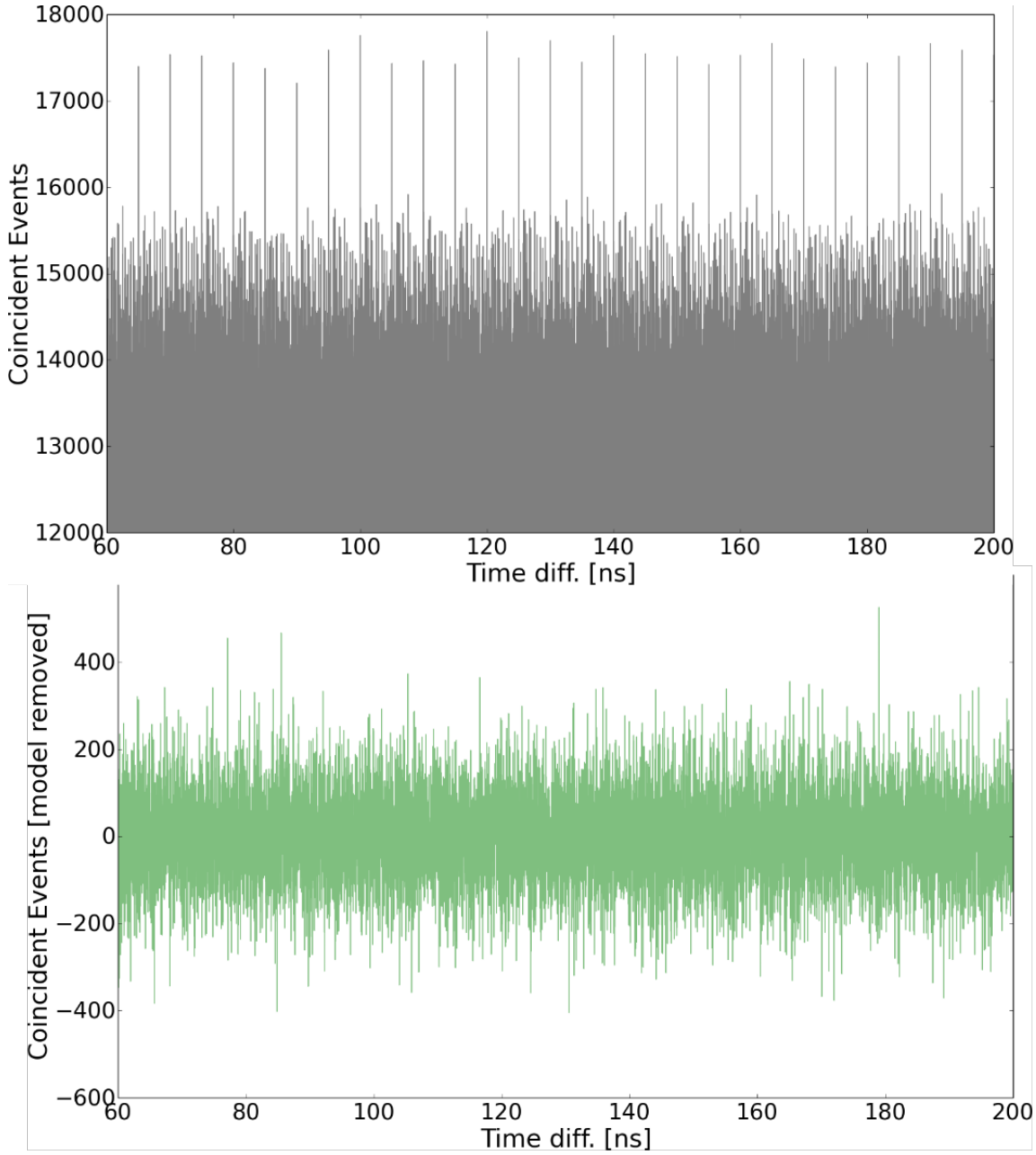

Figure 5.6: Top: Raw data output after cross correlating two signals with visible and periodic DNL signature. The mean number of coincident photons per bin is ∼15000, and the expected σ is ∼120. Bottom: Results after the mask has been removed, centered about the mean. The post-processing σ' is about 135.

Chapter 6

LABORATORY TESTS

To accurately test and quantify the performance of the TDC and primarily, the firmware that was designed, two channels of the signal generator was used (Section6.1. It was determined that the temporal resolution is about 83 ps, significantly higher than that of a SPAD detector. An optical (Section 6.2) was designed and assembled in order to observe correlated photons in the laboratory setting. As is often too common, additional sources of noise were found (Section 6.3, and eventually removed (Section 6.4). Although photon correlations were observed, it was accompanied by an unexplained signature described in Section 6.3.

6.1 Timing Precision

The timing precision of the TDC was measured by using an external signal generator SDG6032X, with two independent channels that were running of the same oscillator. Both channels sent out a pulse train at 6 MHz rate, that mimicked the output of the SPADs in their shape. The duration of the pulse was set to 20 ns, an amplitude of 3.3 V and rise time of 1 nanosecond. Although this provided $\sim$ 500 ps timing precision, this was the fasted rise time available on the signal generator and was close enough to the expected value of 350 ps timing precision achievable with the SPADs.

These channels were coupled to the TDC using the same cables that are used to test the SPADs. An external delay of $\sim$200 ns was introduced by having cables of different length. The data was acquired for a few minutes. The time of arrival difference between the two channels showed Poisson distribution but approached the

expected Gaussian distribution, with $\sigma \sim 83$ ps, as shown in Figure 6.1. While the deviation from the expected Gaussian distribution suggests a bias in the measurements, it is not significant enough to hinder the performance of the entire system. Long-term drift was not expected to induce additional spread in the arrival time as both channels would drift at the same rate.

Approximately the first 400 out of the 512 elements in the delay chain are active as the propagating pulse does not have enough time to reach the end of the delay line within a clock period. With a 5 nanosecond clock cycle of the FPGA (200 MHz), the maximum achievable timing precision is 12.5 picoseconds, matching what other groups have reported in the literature 78; 36. However, we were unable to achieve the expected value of 12.5 ps precision, implying that there is potential for improvement in the setup and the firmware. Nevertheless, with the timing precision of SPADs being higher by a factor of 4 (350 ps), we expect that even with 83 ps timing resolution, the TDC will not be the limiting factor in this experiment.

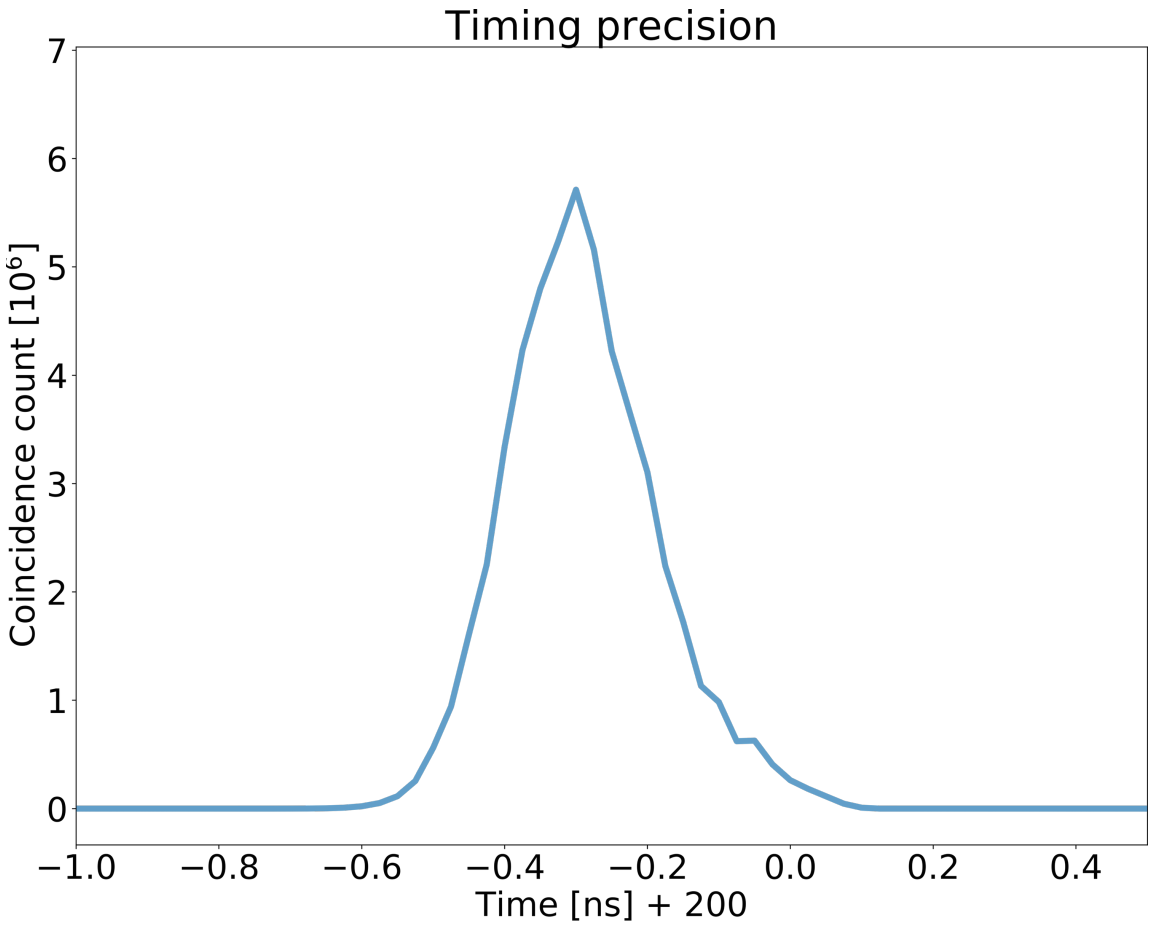

Figure 6.1: Number of coincident pulses observed, as a function of the time difference between them. An offset of $\sim$ 200 ns was introduced externally via different length SMA cables. The FWHM and σ of the distribution is $\sim$ 220 ps and $\sim$ 83 ps, respectively.

6.2 Optical Setup

The light source used to characterize the readout electronics, with SPADs incorporated, is a tungsten-halogen lamp, often used for microscope illumination. The emitted light was passed through a 12.5 μm circular aperture, and collimated by a 2.5 cm lens placed 0.4 meters away. This setup guaranteed that only a single spatial

mode of light was observed, i.e., the "source" was unresolved by our 2.5 cm "telescope". A heat sink was attached to the aperture because throughout an 8-hour integration it would become too hot to touch.

The collimated light was then passed through an Andover Corporation filter (656FS02 25), a 1 nm bandwidth filter of a Gaussian profile, centered at 656 nm. Since the signal to noise is not affected by the bandwidth, the filter served two functions 1) decrease the number of incident photons to avoid detector saturation and decrease the duration of the data analysis and 2) Minimize the number of photons from background ambient light. The filter was placed in the collimated light to avoid spectral leakage outside of the desired band which can occur with narrowband filters if the incident light is not perpendicular to the discriminating surface.

The filtered light was then focused by a secondary lens, placed on an adjustable optical bench stage which allowed for movement of the focal point. A 50/50 beam splitter was used although due to polarization sensitivity, was closer to 60/40 and 40/60 for the two polarizations. The fiber optic cables of 100μm diameter were mounted on adjustable x-y stages coupled the light to Single Photon Counting Module COUNT T-Series from laser components. Alignment in the x- y- z-direction was done manually, by maximizing the count rate in both detectors. Once the alignment was achieved, it proved to be stable for days.

The SPADs, Count T series, with an active area of 100 μm and 75% quantum efficiency, produced an outgoing TTL pulse of 3.3 V with the timing jitter of $\sim$350 ps. The incident photon count rate between the two detectors was 6.1 and 5.9 MHz. We believe the slight mismatch is due to the beam splitter not being a perfect 50/50 optical element, as the dark/ambient count rate was under 2 KHz when tested with the light source in the off position.

A pair of 2 dB attenuators were placed on each end of the SMA cables used

to couple the output of the single photon detectors to the SMA-LVDS board. The attenuators were used in order to lower the amplitude of the TTL pulse down to $\sim$2 V, which is the activation threshold of the LVDS converter chip, as well as minimize internal reflections in-case there is a small impedance mismatch between on the SPAD to SMA and SMA to LVDS interfaces. A delay of $\sim$200 ns was introduced between the detectors by using cables of varying lengths, placing the expected correlation signal well outside of the range where onboard/on-FPGA crosstalk is likely to happen. The optical setup is shown in Figure 6.2

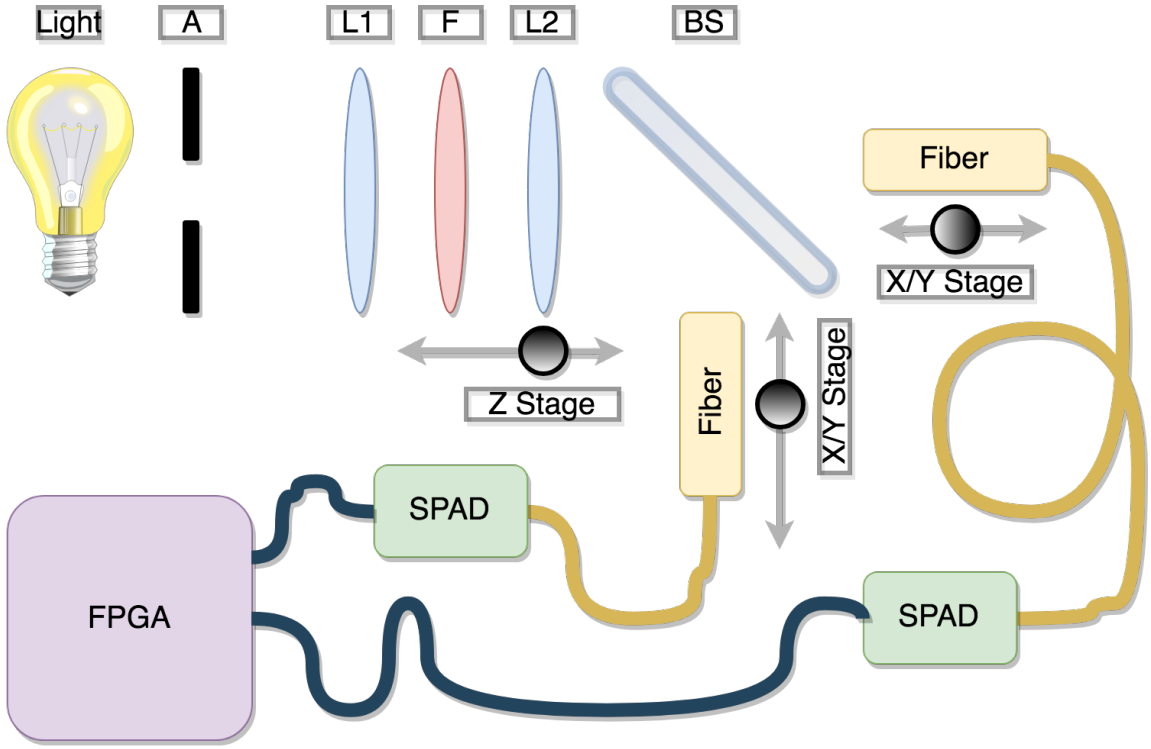

Figure 6.2: Optical setup used for photon arrival time correlation experiments. Components marked are as follows: 'A' is a 12.5 μm circular aperture. 'L1' and 'L2' are two lenses, 2.5 cm in diameter with focal lengths of 0.4 and 0.3 meters, respectively. 'F' is a 1 nm bandwidth filter, with the center frequency of 656. 'BS' represents a 50/50 beam splitter. The movable stages are shown as black points with arrows. The fiberoptic cables of equal length are shown as yellow lines. The SPADs (green blocks) are coupled to the ROACH2/FPGA with SMA cables (dark blue lines) of different length, producing ∼200 ns delay.

6.3 RF Pickup and Modulation

The preliminary observations were of a thermal source with two detectors receiving ∼6 MHz photon rate at ∼ 656 nm with a bandwidth of 1 nm from the same spatial mode. The dataset was acquired continuously over a 24 hour period. A very

prominent feature was detected. The "ringing" signature, centered at the cable time delay, is shown in Figure 6.3. These oscillatory features were significantly higher than the expected white noise as well as the expected signature from the correlated photons when the observing a single thermal source. Furthermore, the growth rate was linear, implying it would not be possible to integrate for longer allowing for the correlation signal to be higher than the noise.

Multiple modifications to the optical setup were made to determine the source of the unexpected noise. Simultaneous observations of two unique light sources, with matched count rate, with fibers coupled directly to them, were made to eliminate the source used in the standard setup as the culprit. With no correlated photons and no correlated intensity fluctuation expected, the noisy feature remained. This measurement demonstrated that the noise source was not due to the illuminator. Subtracting the uncorrelated dataset from the set which should have contained correlated signature did not suppress the noise to acceptable levels.

Firmware modifications were done to eliminate the FPGA as the noise source. Changes were made in the physical placement of the FDR filter and the CARRY4 delay line, and different channels were used. No significant changes in the structure of the noise signature were observed. The data analysis pipeline was also re-written from scratch to no avail.

Optical filters with different bandwidths, ranging from 0.1 to 10 nm centered at different wavelength were used to eliminate possible optical standing waves. The x- y- z- stage adjustments did not affect the signature. Furthermore, varying the delay by changing the cable lengths also moved the temporal center of the noise feature by the expected amount. These variations to the optical setup implied that the noise could not be moved away from the temporal region where the correlated photons were expected. Lastly, different grounds were given to detectors, as well as the actual

optical bench, with no effect.

These trials allowed us to constrain the source of this signature to *free space* crosstalk or possible RF pickup.

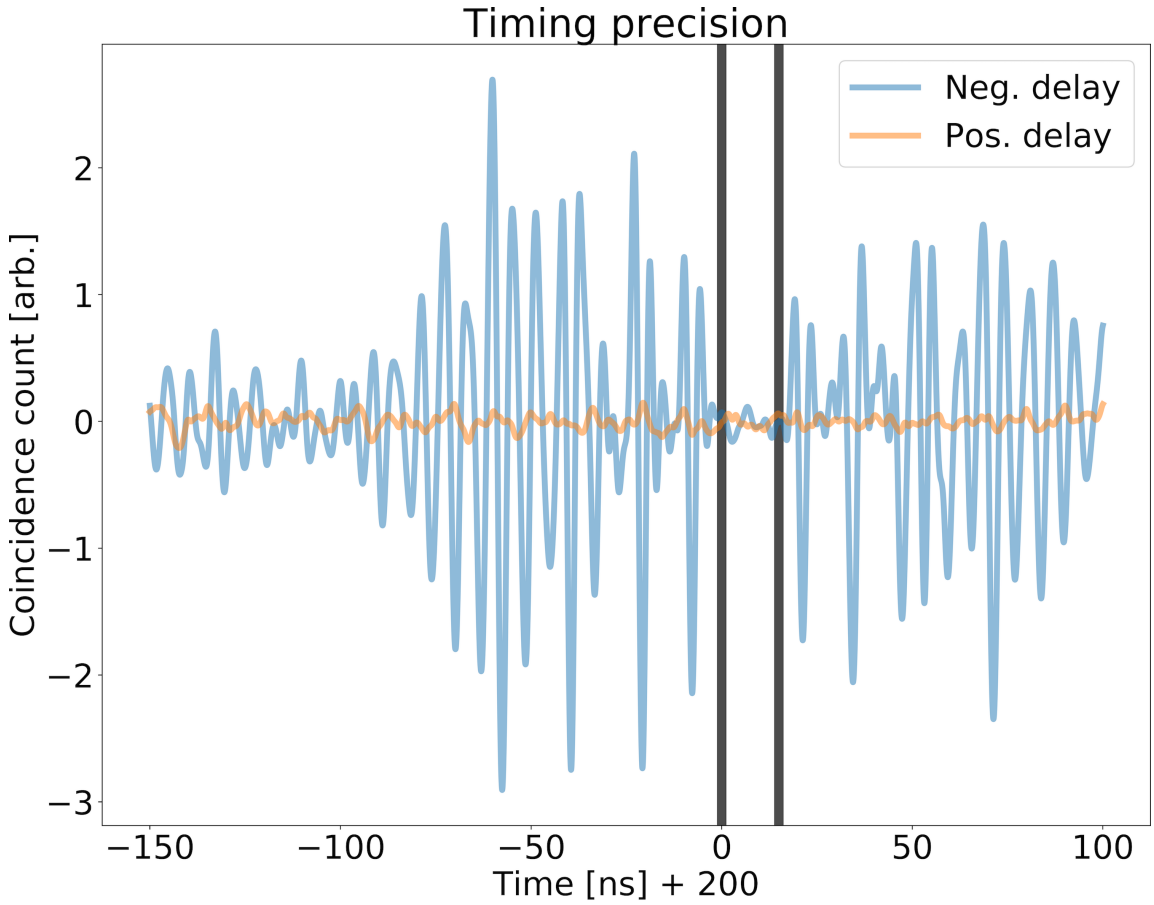

Figure 6.3: Histogram of time differences between pulses from a 24-hour integration with 6 MHz count rate in two optical channels. Blue: a yet-to-be-understood signature, centered at the cable delay, most likely due to some form of RF pickup. Orange is the other side of the histogram, at the positive delay end. The standard deviation of the orange data set is x1.1 that of expected photon noise. Black lines bound the 15 ns window where photon correlations would be expected.

Observations of the output from detectors using an oscilloscope have shown that when a pulse is produced by one detector, there is an additional signature in the other, with a varying amplitude on the order of mV. Even when one detector had no incident photons, the signature remained but would disappear when the second detector was shut off.

These small variations could induce a "shift" in the pulses generated at approximately the same time by changing the trigger levels, which would mimic the observed oscillations. The problem has been resolved, to some extent, by placing one of the detectors in a Hammond box. The box, acting as a Faraday cage, suppresses correlated free space crosstalk between the detectors as well as possible correlated pickup from other RF sources, such as wifi and cellphone signals.

6.4 Hammond Box and RF Shielding

In order to minimize on crosstalk between the detectors as well as any RF pickup that would induce false correlations or systematic time skew, one of the detectors was placed inside a Hammond box. The fiber, as well as the power supply cord and the SMA output, were further shielded with a flexible copper EMI-shielding tube. Preliminary observations of the output from two SPADs on the oscilloscope have shown a significant reduction/elimination of mV level pickup.

Two datasets were obtained to test the efficiency of the Faraday cage: 1) 24-hour integration where correlated photons should be observed, and 2) 24-hour integration where the number of optical modes was significantly increased by changing the aperture from 12.5 μm to $\sim$2 mm. Furthermore, for the uncorrelated integration, the 1 nm bandwidth filter was removed, and neutral density filters were added to match the photon count rate in the two datasets while significantly lowering the expected number of correlated photons. In both cases, the observed photon count rates at

the two detectors were ∼6.2 and ∼5.9 MHz. The signature previously observed was removed, and the results are shown in Figure 6.4.

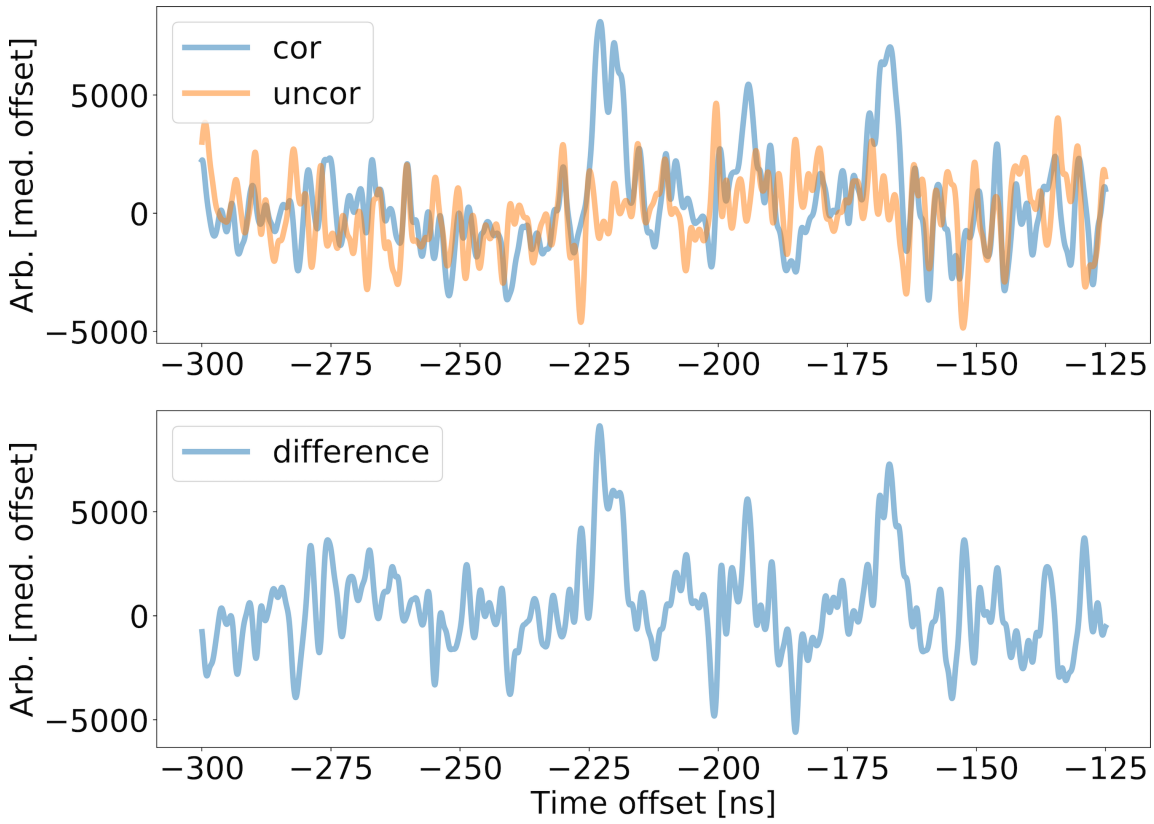

Figure 6.4: Top: Two datasets, where correlations are expected (blue) and no correlations expected (orange). Duration of observations was 24 hours. An offset of $7.6(10^7)$ for the correlated (blue) and $8.3(10^7)$ for the uncorrelated (orange) was introduced to place them on the same scale. Bottom: The difference between the two data sets is shown. The expected signature is ∼ -195 ns delay. The source of the two peaks to the side of it, at ± 25 ns is not yet understood.

It is evident that a significant difference in the photon statistics between the two data sets exists. The data where correlations are expected show 3 peaks, with the

central one located where the correlations are expected, with the side peaks ± about 25 ns away, matching the pulse duration of the SPADs. This signature is absent from the dataset where no correlated photon observations are expected. While the triple peak feature is not fully understood, the experiment is showing exciting results, as there is a difference between the two datasets. A Gaussian filter, matching the width of the expected peak produced by correlated photons has been used to smooth the data.

6.5 Additional Peaks and Troughs

The expected signal is located less than 500 ps from the predicted time delay. The amplitude is closely matched to what is expected theoretically. The profile of the optical filter can explain the difference. The 1 nm bandwidth filter has a Gaussian profile, while the model assumes that it is top hat in shape; The Gaussian profile is expected to have a slightly higher number of correlated photons because of the wings vs. flat profile. The model is superimposed on the real data after the uncorrelated data set has been subtracted, shown in Figure 6.5.

The trident shape, with peaks about 22 ns to each side of where the correlated signal is expected, as well as the anti-correlated minima at about 7 ns to the sides, is not fully understood. The area of the two peaks, even with the minima included, is too large to be "induced" by the correlated signal. Therefore, the source is most likely not related to the observed photon bunching effect but could be explain by the optical setup. The only difference between the correlated and the uncorrelated data set is the optical bandwidth and the number of spacial modes. The separation of ∼22 ns and 7 ns corresponds to about 6 and 2 meters, respectively. It is possible that an optical standing wave has occurred somewhere in the setup, but such a claim requires additional tests, which will be performed in the near future.

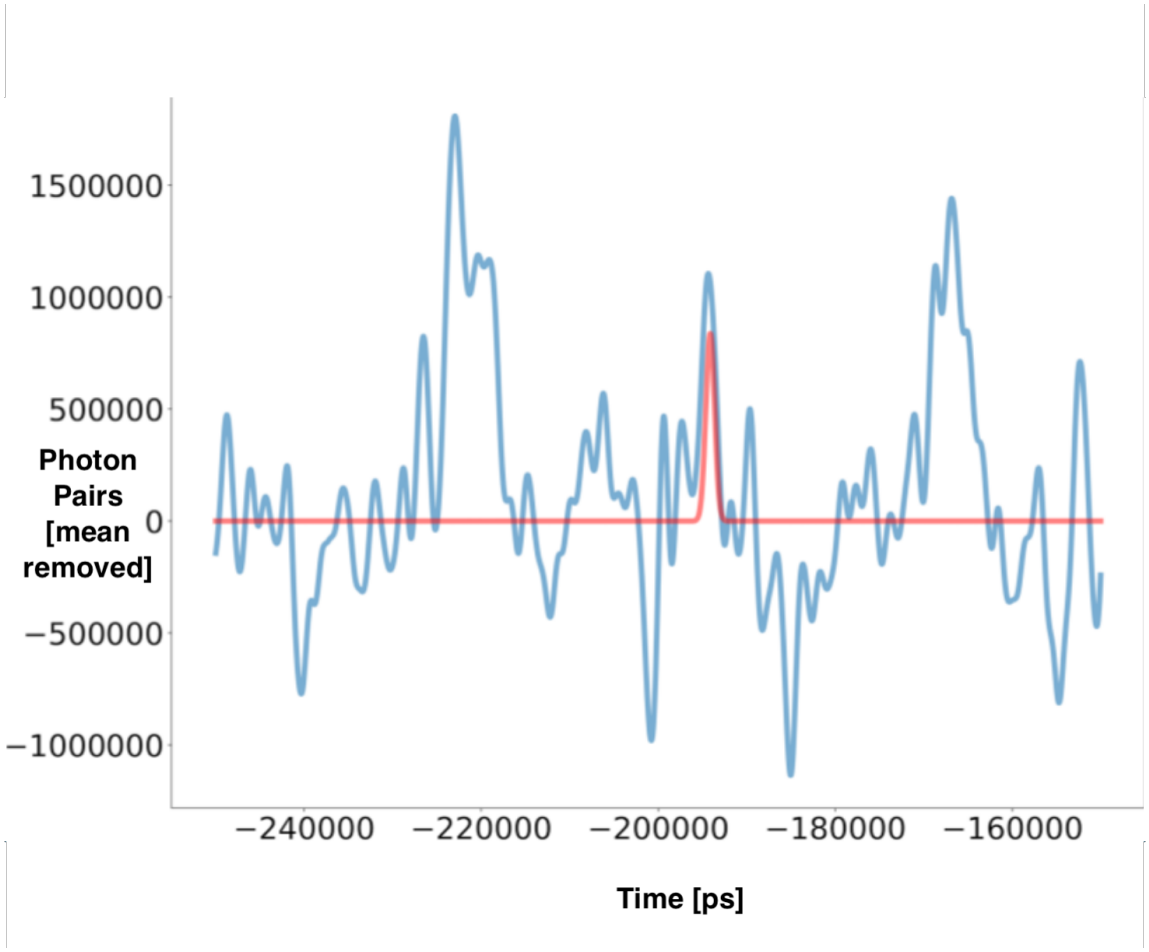

Figure 6.5: Reduced dataset of coincident photon arrival times as a function of a time delay between two channels (Blue). The red Gaussian represents the expected signal, placed at the predicted time delay.

Chapter 7

IMAGE INVERSION SINGLE PHOTON INTERFEROMETRY FOR EXOPLANET CHARACTERIZATION

Sometimes, spending years focusing on one idea can drive spinoff concepts. While not directly related to single photon interferometry, the proposed method does utilize similar technique and equipment. The application discussed in this chapter focuses on exoplanet measurements, and the starlight, as well as bunched photons, are considered noise, like an *anti-thesis* to the proposal discussed thus far. Even in its infancy, the concept is intriguing enough to explore further. The approach is the same, measuring individuals quanta of light, carry on with the general theme of quantum-astrophysics.

7.1 General Overview

Throughout the last two decades, thousands of exosolar planets have been identified orbiting stars. Thanks to dedicated survey missions like HARPS PHASE (2003), HAT Bakos *et al.* (2002), WASPStreet *et al.* (2003), and KEPLER Borucki *et al.* (2010), astronomers are able to derive exoplanets orbital period, eccentricity, separation from the star, temperature, mass, density, etc. However, the exoplanets elemental content remains a difficult parameter to measure. The lack of chemical composition data on exoplanets is a significant detriment when attempting to understand their formation, evolution, albedo, surface temperature, and potential biological signatures.

The obstacles in directly measuring elemental abundances are two-fold: 1. The fundamental resolution limit of the optical system, a reoccurring theme in astrophysics and 2. The contrast level between the exoplanet and its host star.

In this chapter, these two problems are addressed, and a solution is proposed

with regards to mitigating the resolution and contrast issues of a star/exoplanet systems; the technique, Image Inversion Interferometry (**iii**) is shown in Figure 7.1, as a concept sketch, demonstrating the evolution of two-point spread functions (PSF) as they propagate through the optical system.

There are three goals in this chapter, which are: First, Investigate the feasibility of image inversion interferometry for astrophysics with the focus on exoplanets. The next goal is to derive idealized instrument response as well as identifying sources of noise. Lastly, estimating the possibility of sub-Rayleigh resolution and contrast level suppression.

In order to achieve this goal, Section 7.2 provides background information on the current exoplanet imaging techniques (7.2.1) and the proposed technique to obtain sub-Rayleigh resolution (7.2.2). In Section 7.3.1, the theoretical limit of the technique is derived, the case for single photon detection made in 7.3.2 and first-order noise terms introduced in 7.3.3. The photon loss and the efficiency of the technique, are discussed in section 7.4, while the contrast reduction is presented in Section 7.5.

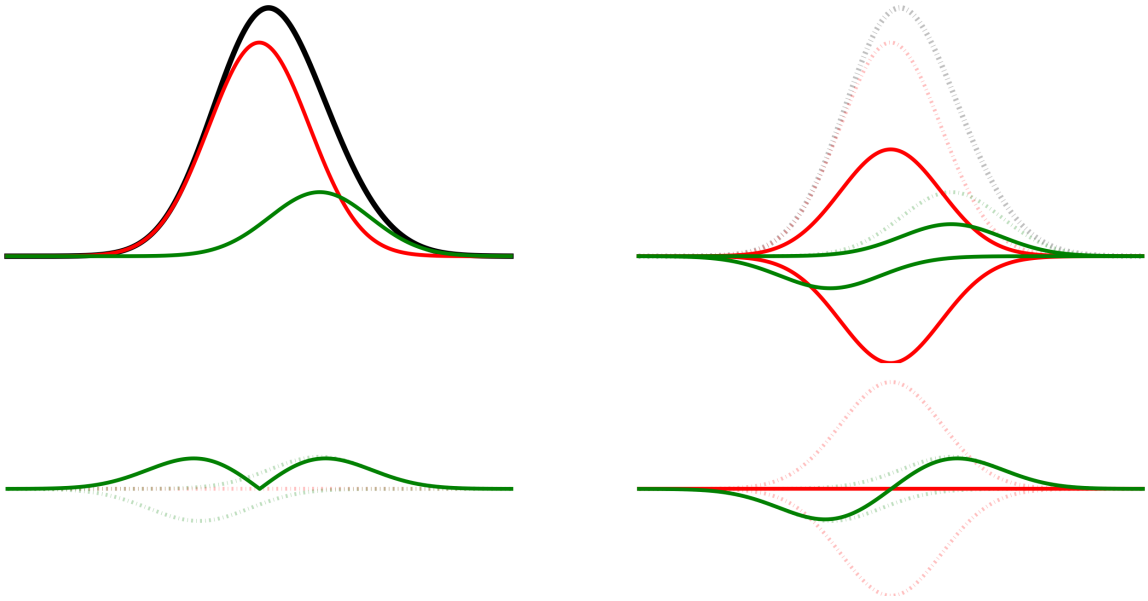

Figure 7.1: **Top left**: Two Gaussian PSFs with different areas representing the brightness of point sources. The black curve is the superposition of the two. The red one dominates in terms of brightness relative to the dim green one, making observations of the dimmer object significantly more difficult. **Top right**: The light beam is separated into two, one of the beams is phase-shifted by π and flipped along the x-axis. The two beams are then recombined. The previous image is superimposed as a dotted line, with increased transparency, for comparison. **Bottom right**: Upon the recombination, the PSF of the bright red source $\rightarrow$ 0, while a portion of the dim green source remains. **Bottom left**: The absolute value, which describes the detection statistics of the PSF, with only the dim source remaining.

7.2 Background

The resolving power of a telescope is set by the Rayleigh Criteria Rayleigh (1879), which states that an observer will not be able to differentiate between two PSFs if their *angular* separation (θ) is less than $\sim \lambda/d$, with λ representing the observational wavelength and d is the aperture of instrument. While θ of an exoplanet/star sys-

tem depends on the systems orientation, distance, and actual separation, it can be approximated to have values ranging between 0.5 arcseconds Perryman (2011) and smaller for the systems which are relatively close to Earth. Therefore, a single dish optical telescope of the 2-10 meter class, is capable of resolving the two PSFs. To compensate for the atmospheric turbulence, adaptive optics system Beckers (1993) should be used to make the receiver approach diffraction limit.

7.2.1 Current Imaging Techniques

The issue of contrast is significantly harder to address. Multiple instruments attempt to suppress starlight by placing a coronagraph within their optical design. Instruments such as the hybrid Lyot coronagraph Trauger *et al.* (2011), Optical vortex coronagraph Foo *et al.* (2005) and Shaped Pupil Coronagraph Belikov *et al.* (2007) achieve this by utilizing some form of a pupil mask within their optical setup to block the light from (and around) the star. The implementation is not perfect, with some starlight "leaking" through due to diffraction, thus placing a limit on the dimmest exoplanet that can be observed. Additionally, physically blocking the light will induce photon loss from the exoplanet as it approaches the $\sim \lambda/d$ limit since a portion of its PSF will be occulted by the mask. Furthermore, the performance of the coronagraph lowers the number of photons from an exoplanet when the separation between the two objects closer than 4 times or less than the diffraction limit of the telescope, putting more stringent constraints on which system can be observed.

An alternative to placing a pupil mask, the bright sources can be dimmed via destructive interference produced by a phase offset in the incident light. Proposals have been made to use Phase-Induced Amplitude Apodization (PIAA) Guyon (2003), Visible Nulling Coronagraph (VNC) Lyon *et al.* (2005) and Segmented Aperture Interferometric Nulling Testbed (SAINT) Hicks *et al.* (2017). The method can be

applied to multiple dish array, segmented mirrors or single mirrors. However, using simple phase cancellation technique would allow the telescope not only to suppress the brightness of the host star but also venture into the sub-Rayleigh regime in terms of resolution.

7.2.2 Sub-Rayleigh resolution

While it may appear that the classical wave nature of light has placed a threshold on the resolution limit, the field of quantum metrology Braunstein and Caves (1994) is showing promise in going beyond the Rayleigh Criteria. Based on Quantum Estimation and Detection theory Helstrom (1976), the field of quantum metrology has demonstrated Wicker *et al.* (2009) that sub-Rayleigh resolution could be achieved in a controlled laboratory setting for *coherent* sources; its implementations in the far-field for thermal sources has yet to be demonstrated. Nevertheless, it has been shown that the quantum Cramér-Rao bound (qCRB) is, which determines the privation limit of a measurement, significantly lower than what is expected from the classical CRB constricted by the Rayleigh limit Tsang (2016). This effect can be achieved through photon counting statistics and different propagation modes of light as proposed by Tsang *et al.* (2016).

A simplified method "Super Localization by Image Inversion interferometry", (SLIVER), introduced by Nair and Tsang (2016), can achieve similar results through image inversion and a two-arm interferometer. While the goal of SLIVER is to measure the separation between two equally bright sources, the application for exoplanets discussed in this chapter relies on the other extreme; it is assumed that the two PSFs are high in contrast ratio and the center, while unknown, is determined by the centroid of the system. Therefore, information regarding the separation between the exoplanet and its host star is not necessary if the observations are performed on a

system *known* to harbor an exoplanet. Rather, the goal of the measurement is to suppress the contrast between the two sources to such a degree that the number of photons from the exoplanets exceeds those that are "leaked" from the star.

The SLIVER instrument, shown in Figure 7.2, functions as a modified Mach-Zehnder interferometer Zehnder (1891), Mach (1892). Collimated light from the receiver, an optical telescope, in this case, will enter the instrument and be split into two "arms" via 50/50 beam splitter. One of the arms will undergo image inversion by passing through two lenses separated by 2×focal length, although such a feat can be achieved by other means. This procedure reflects the image about the center. A half-phase path length difference between the inverted arm and unaltered one will produce constructive and destructive interfering beams upon recombination. The beams are combined with a secondary 50/50 beam splitter, producing the two output which could be measured with a single pixel photon detector. In our application, the constructive arm can be used to obtain the centroid position, while the destructive arm to measure the photons from the exoplanet.

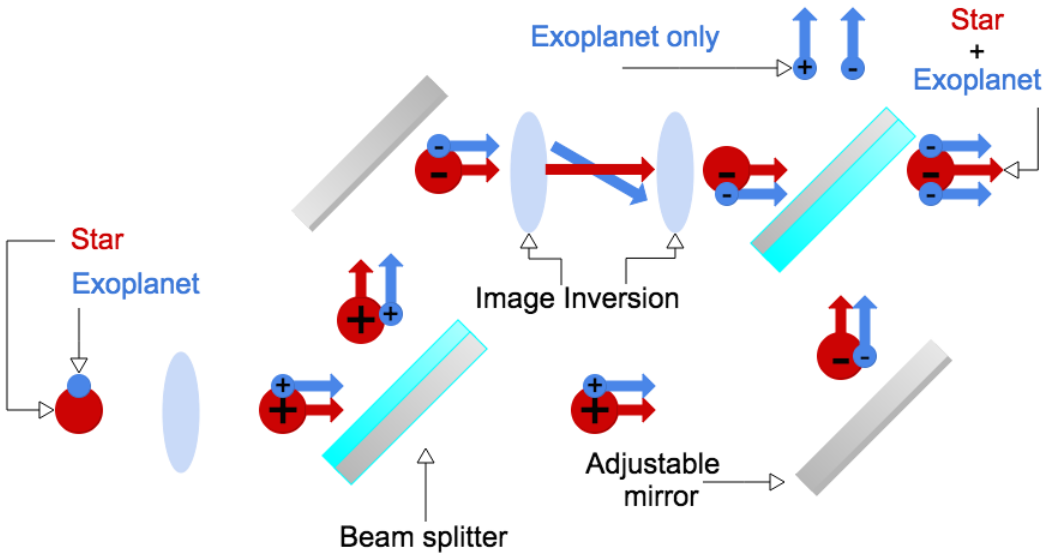

Figure 7.2: The light from a star (red) and an exoplanet (blue) is collected with the telescope, and split into, via a beam splitter, into two arms of the interferometer. One arm (top) undergoes image inversion and phase shift. The arms are recombined, producing constructive and destructive interference in the imaging plane, where detectors can be placed.

7.3 Semiclassical Explanation

7.3.1 Theoretical limit and total cancellation of the host star light

The electric field (E) entering the modified Mach-Zehnder interferometer can be described as a product of a complex amplitude A and a two dimensional Gaussian

$\psi(x, y)$, where x and y coordinates on the imaging plane:

$$E = A\psi(x, y). \tag{7.1}$$

In this case, the Gaussian distribution is assumed to be perfectly symmetrical with variance of σ^2 and integral of which yields:

$$\int_{-\infty}^{\infty}\int_{-\infty}^{\infty} \psi^2(x, y)\, \delta x\, \delta y = \pi\sigma^2 \tag{7.2}$$

For clarity, (and consistency with Nair and Tsang (2016)) notation change of $\psi(x, y) \rightarrow \psi(\rho)$ will be used for the remainder of the chapter, where ρ is used to represent the x and y coordinate on the imaging plane.

The electric field incident upon a detector in a diffraction limited telescope, observing an exoplanet (p) and its host star (s), can be described as a summation of the two:

$$E = A_s\psi(\rho_s) + A_p\psi(\rho_p). \tag{7.3}$$

The light is split into two arms with a 50/50 beamsplitter such that:

$$\begin{aligned} E_1 &= \frac{1}{2}(A_s\psi(\rho_s) + A_p\psi(\rho_p)) \\ E_2 &= \frac{1}{2}(A_s\psi(\rho_s) + A_p\psi(\rho_p)). \end{aligned} \tag{7.4}$$

Image inversion, achieved by rotation along the x and y axis of the imaging plane, as well as phase offset of half the period modifies the electric field in the second arm to

$$E_2 = \frac{-1}{2}(A_s\psi(-\rho_s) + A_p\psi(-\rho_p)). \tag{7.5}$$

By centering at the star, $\rho_s = -\rho_s = 0$ and $\rho_p \neq -\rho_p \neq 0$, and the electric field produced at the two outputs, constructive (c) and destructive (d) ports, of the interferometer are:

$$E_c = \frac{1}{2}\big[2A_s\psi(0) + A_p\psi(\rho_p) + A_p\psi(-\rho_p)\big]$$
$$E_d = \frac{1}{2}\big[A_p\psi(\rho_p) - A_s\psi(-\rho_s)\big] \tag{7.6}$$

It is evident that the electric field from the star in the destructive port is canceled, leaving only the light emitted by the exoplanet; two PSFs, now parted by twice the original star-planet separation.

7.3.2 Coherence time and single photon detection

The measurable intensity at the detectors from the two arms of the interferometer can be described as the $I_{c,d} = E^*_{c,d}E_{c,d}$, the electric field multiplied by its complex conjugate. $A_s\psi(\pm\rho_s)$ terms are not canceled out yet, because perfect cancellation is unlikely to be achieved; this also allows for a model of "leaked light" in the following section.

Because the number of detectable photons is proportional to the intensity ($\bar{N} \propto I$), the average number of photons in both of the arms of the interferometers can be rewritten as:

$$\bar{N}_c(\rho) \propto \big[A_s^2\kappa_c(\rho_s) + A_p^2\kappa_c(\rho_p) + \xi\big]$$
$$\bar{N}_d(\rho) \propto \big[A_s^2\kappa_d(\rho_s) + A_p^2\kappa_d(\rho_p) + \xi\big]$$
$$\kappa_c(\rho) = \psi(\rho)^2 + \psi(-\rho)^2 + 2\psi(\rho)\psi(-\rho) \tag{7.7}$$
$$\kappa_d(\rho) = \psi(\rho)^2 + \psi(-\rho)^2 - 2\psi(\rho)\psi(-\rho).$$

The cross terms between the two amplitudes (ξ), is applicable when the number of photons per coherence time is much greater than one. In the majority of the cases, observations of stars at optical wavelengths will not satisfy this requirement. The number of photons, per area, per second (P) can be approximated for stars of

different magnitudes using the Bessel approximation Bessell (1979) as

$$P = 3640(10^{-0.4m_v})(1.51 \times 10^7)A\frac{\Delta\lambda}{\lambda}. \tag{7.8}$$

The value of 3640 was experimentally obtained, in units of Jy, m_v represents the apparent magnitude of the star, (1.51×10^7) is a conversion factor from Jy to photons per sec., per m^2, A is the area and λ is the wavelength.

Since the coherence time is inversely proportional to bandwidth

$$\tau_c = \frac{1}{\Delta\nu} = \frac{\lambda^2}{\Delta\lambda c}, \tag{7.9}$$

the average number of photons over the course of coherence time (P_c) is approximately, after combining constants,

$$P_c = 183(10^{-0.4m_v})A\lambda. \tag{7.10}$$

At wavelengths of 550 nm, using the brightest stars ($m_v = 0.0$) and observing using a 30 meter diameter class telescope, which has yet to be constructed, $P_c \approx 0.08$. It is therefore acceptable to assume that P_c will be significantly lower than 1, for optical observations, which allows us to drop the the cross terms from Equation (7.7) and simplify it to:

$$\begin{aligned} \bar{N}_c(\rho) &\propto \left[A_s^2\kappa_c(\rho_s) + A_p^2\kappa_c(\rho_p)\right] \\ \bar{N}_d(\rho) &\propto \left[A_s^2\kappa_d(\rho_s) + A_p^2\kappa_d(\rho_p)\right] \end{aligned} \tag{7.11}$$

With a single photon per coherence time entering the instrument, constructive and destructive interference will be done by the photon *with itself*. Furthermore, although expanding the bandwidth will increase the number of photons, the coherence time will contract by the same factor. Therefore, this approach allows for the instrument to operate at full bandwidth, so long as the probability of 2+ photons within the same coherence time is small.

7.3.3 *Associated Errors*

An initial estimate of the instrument performance based on the proposed setup can be derived theoretically and analytically if some assumptions about the system can be made. The centroid of the star-exoplanet system will set the center of the imaging plane ($\rho_c = [x, y]$) over which the inversion will be performed; higher contrast ratio will, therefore, move the ρ_c towards the true center of the star ρ_s, ensuring better alignment and higher photon cancelation. For simplicity, the assumption that the only misalignment in ρ_c is due to the centroid location, while the x-y dimensions in the imaging plane used to recombine the light is correctly aligned.

The optical alignment along the z-direction will set the path-length difference between the two light beams thereby determining how close to complete destructive interference the system is operating. Because of the ongoing efforts to achieve picometer optical alignment Keesey (2016), the value of δ_ϕ is approximated as $\frac{10^{-5}}{\lambda}$, with λ representing the observational wavelength in micrometers. The mismatch in system efficiency between the two arms is represented as attention ratio δ_a and is assumed to be induced by imperfections in the optical system. By introducing the δ_ϕ and δ_a terms into Equations (7.6-7.11), we obtained the modified value of κ_c and κ_d as

$$\begin{aligned} \kappa_c'(\rho) &= \psi^2(\rho) + \delta_a^2\psi^2(-\rho) + 2\cos(2\delta_\phi)\psi(\rho)\psi(-\rho) \\ \kappa_d'(\rho) &= \psi^2(\rho) + \delta_a^2\psi^2(-\rho) - 2\cos(2\delta_\phi)\psi(\rho)\psi(-\rho) \end{aligned} \tag{7.12}$$

The trigonometric term $2\cos(\delta_\phi) = e^{i\delta_\phi} + e^{-i\delta_\phi}$ used to convert complex phase components and represent them as real values.

Additional error such as 1) atmospheric turbulence "shaking" the image at ∼KHz rate 2) thermal fluctuations inducing expansion/contraction thereby changing and bending the arms of the interferometer 3) ambient photons not generated by the

star/exoplanet system, 4) asymmetry in the PSF of the star allowing for additional photon "leakage" are reserved for future analysis.

7.4 Photon Loss

As the separation between the point of image inversion and an exoplanet decreases, a portion of the PSF will begin to interfere with itself to a progressively higher degree. In order to understand how significant such an effect is, comparison of the number of photons from the exoplanet before (N_{p_o}) and after (N_p) image inversion has been made. This relationship was computed as a function of the separation (in units of σ, often referred to as full-width half-max in astrophysics) and the initial brightness ratio of N_{p_o}/N_{s_o}. Perfect alignment was assumed, to obtain the fundamental limitation of this technique.

By exploring the two dimensional parameter space N_{p_o}/N_{s_o} and σ, we can observe that the loss of photons occurs fairly rapidly. At the separation of $\sim 0.8\sigma$, only $\sim$50% of the original photons remain. This effect becomes even strong with only 25% and 10% remaining once σ is ~ 0.5 and ~ 0.3, respectively.

Additionally, when the star is brighter by about a factor of $\sim 10^2$ relative to the exoplanet, the center of image inversion is close enough to the actual center such that it has no noticeable effect. However, when the star and the companion, most likely a dimmer star or a brown dwarf at this point, are comparable in brightness, the centroid is misaligned which causes additional photon loss from the dark object. This implies that the **iii** method should preferentially be applied to high contrasting PSFs. These results are summarized in Figure 7.3.

While the photon loss is not ideal, being able to resolve objects past the limitations of standard single aperture imaging system is enticing. The computational outcome is obtained with the assumption that the probability of 2 photons arriving

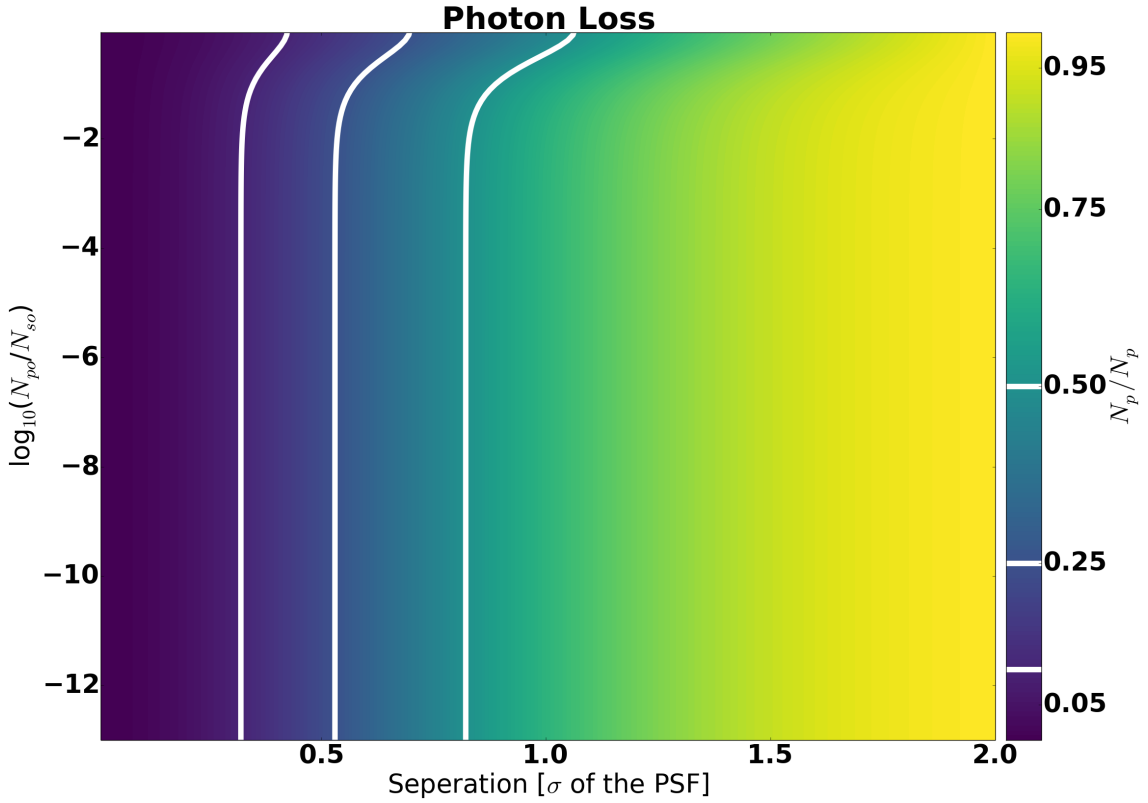

Figure 7.3: The x-axis is the separation between the bright and the dim source, in units of their PSF. The y-axis represents the contrast ratio of the exoplanet to star, on the $\log_{10}$ scale. The color bar represents the "efficiency" of the system. The white lines on the plot and the color bar represent a loss of 50, 75 and 90 % at of the original photons which occurs the separation between the exoplanet and the star is about 0.75, 0.5 and 0.25 σ. The deviation of the vertical line at contrast levels between -2 and 0 are due to the offset in the centroid position, thereby misaligning the two arms. This effect is also visible in Figure 7.4.

over the course of coherence time is significantly less than 1, which is the case for most astrophysical objects at optical and NIR wavelengths; otherwise, the statistical derivation would need to compensate for photon bunching, a topic beyond the scope of this paper.

7.5 Contrast Ratio

To compute the contrast ratio, an assumption was made that the attention between the separate arms of the interferometer was equally ($\delta_a = 1$), phase mismatch of $\delta_\phi = 10^{-5}$ and with the center of inversion set by the centroid location between the two sources. In order to determine the limiting magnitude for different bright-dark object configurations, a two dimensional parameter space of original contrast (N_{p_o}/N_{s_o}), the separation of the sources ($\rho_2 - \rho_1$), from which their antisymmetric image contrast ($\bar{N}_2/\bar{N}_1$) was derived.

Under this premise, the most significant reduction, in contrast, occurred for targets with an initial ratio of $\sim 10^{-5}$ and resulting ratio of $\sim 10^4$, an increase in 9 orders of magnitude! Albeit the calculation is simplified, the result is never the less, promising especially since the theoretically it is possible to remove the signal from the star completely.

In Figure 7.4, the area of interest is bounded by the red and white curve(s). The white boundary corresponds to 0, and the red represents -1. This value signifies that the variance in $N_p = N_s$ and $N_p = 10 \times N_s$, respectively. The upper bound appears due to centroid offset since the brightness of the star, and its companion are comparable.

It is generally approximated to the first order that Jupiter and Earth-like planets will have 10^{-8} and 10^{-10} contrast ratio relative to their host star Schworer and Tuthill (2015). Based on the preliminary estimates, image inversion could help single dish

instruments achieve the sensitivity required to obtain light from binary stars down Earth-like exoplanets. Observations at different wavelengths obtained either simultaneously with multiple detectors or by changing filters, would provide spectra and potentially, insight into their chemical composition.

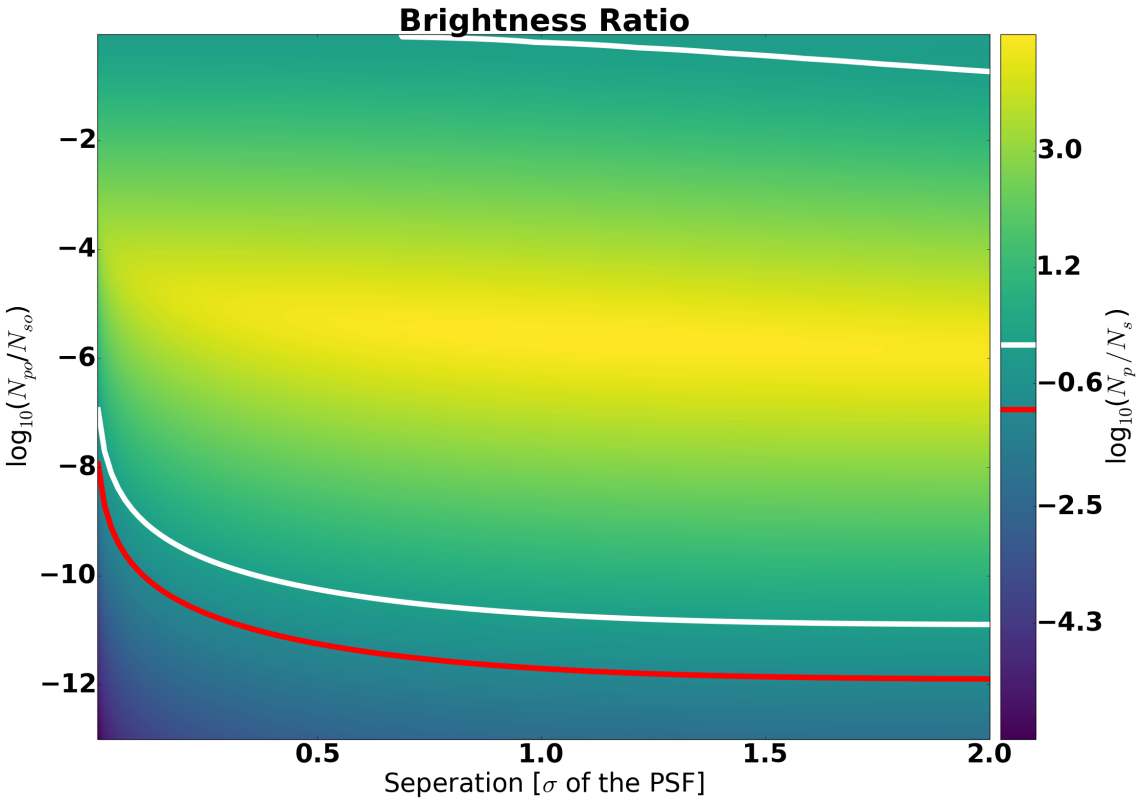

Figure 7.4: Comparing the brightness ratio of the two sources on the $\log_{10}$ scale in the normal imaging system (y-axis) and the inverse image (z-axis, color bar) as a function of the separation between the two sources, in units of their PSFs. The white boundary line is set at a value of 0, where $\log_{10} N_2/N_1$=1. The region in the middle of the figure is where a significant portion of the light from the dimmer source is observed while the brighter source is nulled at the maximum. The boundary on the upper right-hand side of the figure is due to the centroid being offset significantly from the center of the bright source since their initial ratio is on the order of 0.1 to 1. The lower boundary is created when the amount of "leaked" light due to phase mismatch in the phase of the recombined beams.

Chapter 8

FUTURE DEVELOPMENT

This chapter serves as a general review of the topics already discussed, in the reverse order of appearance, throughout the thesis. Extrapolations as to where the field may, or in-fact should go is made.

8.1 Image Inversion Interferometry

Image inversion interferometry method applied to far-field measurements, specifically exoplanets, provides an alluring scenario. *The ability to spatially resolve the PSFs beyond that is possible with the conventional method is especially intriguing.* Albeit it comes at the cost of valuable and scarce photons, the ability to resolve beyond the Rayleigh limit as well as 3- 4-times of what is offered with the coronagraph makes this method an inspirational pursuit.

However, additional steps are necessary to grasp how such a device would function in practice fully. To achieve this, laboratory tests need to be performed to fully understand and characterize the limitations of the system and sources of error. Construction of the prototype would allow a more robust error analysis to be performed which would identify the limiting factors and create a roadmap towards improving the instrument.

The advantages component of image inversion interferometry is the ability to significantly repress brightness of an observed star in order to obtain information about the exoplanet which would typically not be accessible. If the separation between the two is well known, then photon counting "below" the Rayleigh limit is possible. The instrument would function in a targeted fashion, as opposed to a survey mode.

With the primary function of going after known exoplanets, the separation between them and their host star will be a known parameter; Separation tends to be a known parameter for exoplanets found via photometry or radial velocity measurements which constitutes a significant portion of all known exoplanets.

With the high level of contrast suppression, it would appear as though observations of Jupiter and Earth-like planets is possible, assuming enough photons are collected. This task should be relatively easy to achieve with a wide-band observation.

The limiting brightness ratio was derived, with the model presented in Chapter 7, under the assumption that single pixel detectors were used. Of course, this may not be the case when such an instrument is constructed.

It is relatively easy to image a two-dimensional array placed at the imaging plane which would show residuals of destructive interference. Further investigation into what, if any, additional information could be obtained is necessary to understand if post-processing algorithms could be applied to improve the precision of the measurement. Observations at different times, days, weeks or even months, would allow for the system to change configuration and additional constraints could be applied to the orbital solution.

If the multi-PSF system is under the observation, with objects of uniform or randomly distributed brightnesses, the components will affect the measurements in unexpected ways. However, physically changing the locations of the centroid, in a single-pixel scanning fashion, should in principle allow for the observe to create a consistent set of equations, a full rank matrix. The feasibility should be explored as it may allow for full 2-dimensional imaging at sub-Rayleigh resolution.

Ultimately, such an instrument would be better suited for a space-based mission. The effects of the atmosphere, such as scintillation, would be none existing, allowing for better control of the optical setup and symmetry of the PSFs. Furthermore,

observations in the near-infrared could be better suited to studying the transmission spectrum of an exoplanet that has a similar composition to the Earths. With an exponential growth over the recent years in the number of known exoplanets, there exists no shortage of viable targets for investigating the elemental and chemical composition of these exotic worlds. The techniques under development have yet to probe these properties fully. Therefore, image inversion interferometry could be a viable technique, either as a stand-alone or a complimentary one, to add to our understanding of planetary evolution, composition, and habitability.

8.2 Additional signatures in the correlated dataset

The features presented in Section 6.5 are extremely puzzling for a multitude of reasons. Because of its absence in the uncorrelated data set, culprits such as software, firmware, and hardware can be completely ruled out. A claim can be made that the additional, symmetrical, peaks and troughs are correlated to the $\Gamma^{(2)}$ measurement. The difference is 1) the optical bandwidth used in the experiment and 2) the number of spacial modes present.

One obvious change and its effect on the signature is different wavelength filter, with different optical bandwidth. Commercially available options are relatively inexpensive, ranging from 10s to a few 100s of dollars. With the quantum efficiency of the detectors being $\geq$50% across 600$\pm$50 nm, multiple filters can be tested. Ideally, different pairs (or triples) of filters should be selected such that central wavelength can be held constant, while the bandwidth is varied, as well as the reverse of constant bandwidth but different central wavelength.

The experiment would be reasonably easy to set up and test, but the time duration would be long since each measurement requires $\sim$ 24 hour long integration and terabytes worth of data per measurement.

The second type of test would take equally long per measurement. The features of the noise dependency on the number of spacial modes can be explored with a variable aperture or a set of apertures. The photon rate should be held constant, which can be done by turning the power to the light source down as the number of spacial modes is increased.

The fact that the noise is only present when correlated photons are observed is troubling, as it defies the well-established photon statistics. What is even more confusing is that the noise features are *stronger* than that of the $\Gamma^{(2)}$. *This implies that if the noise is due to the correlated photons, it is further amplified by some external factor, which is either a troubling or an exciting prospective.* Exploring the dependency on the bandwidth and number of spacial modes should shed some light on the subject matter.

8.3 Readout electronics for single photon detectors

Intensity interferometry with single photon counting requires highly sensitive and precise instruments. Although some commercially available electronics are capable of achieving the required photon time tagging rates and precision, problems like duty cycle or high cost of the modules make it difficult to implement these systems in larger arrays. Custom readout electronics, based on open source hardware/firmware/software with relatively low fabrication cost is necessary if a dedicated optical interferometry array is to be built.

8.3.1 ROACH2 Upgrades

The advantages of the time to digital converter presented in Chapter 5 over the commercially available options is the cost, ability to have numerous channels, and continuous operation. The preliminary results of a time to digital converter based on

the ROACH2 platform is capable of obtaining timing resolution that is an order of magnitude better than the single photon detectors.

Further efforts should go towards modifying the firmware to increase the number of channels and optimizing the data transfer rates with a 10 Gb port. Although possible in theory, such a configuration has yet to be demonstrated. An implementation of +60 channels would require an overhaul of the firmware, but the fundamental principals established should remain the same. Tests would have to be performed to quantify what happens on the inside of the FPGA fabric when multiple pulses enter asynchronously and propagate through the delay line.

The drift of local oscillators, relative to one another, in these boards, will also need to be measured, quantified and mitigated, in order to achieve full decoupling of the telescopes. Once the rate of drift is well established, a proper solution can be implemented. If a GPS unit is a viable approach, then commercial units can easily be acquired and integrated into the system. However, if the drift of the onboard oscillators is too high, $\sim$ 500ps per second, then a more complicated approach using free space, line of sight, and a master clock system would need to be used.

Efforts to create +60 channel TDCs *with* continuous operation are already on the way. Applications extend beyond the proposed single-photon interferometry, and into the regime of quantum key distribution as well as optical communications.

Implementation of such a feat would be of enormous contribution to single photon and intensity interferometry.

8.3.2 Future Readout Electronics

Although the proposed readout electronics utilize the tapped delay line, the method will change as the technology continues to evolve. The current technological trends are driving innovation into a regime where multiple components will be placed on the

same chip. Recently, manufacturers like Xilinx, who designed Virtex 6 currently in use with ROACH2 board, started created a multiprocessor system-on-chip (MPSoC). The difference of MPSoC relative to the currently used FPGA is an addition of an analog to digital converter as well as a processor, on the same chip.

A high-speed ADC can be used to provide stamps of photon arrival time, and since 10+ GHz operational frequencies of these devices is not uncommon, a timing resolution on the order of tens to hundreds of picoseconds can be achieved. By multiplexing the output from single-photon detectors, it is possible to have the output from each transversing on a single line into the ADC.

Multiplexing would require that each SPD generates a unique signature. The most straightforward approach would be to create a voltage divider, such that each power output is different for each line. This action can be achieved with a single custom board, with multiple inputs and a single output. Thus, the pulses can be stacked on one another. The ADC would then need to be able to resolve this, without confusing pulses. The number of required bits would be set by the power produced by one of the SPDs, and the total range available.

Once this is achieved, the FPGA could be used as a discriminator, separating the pulses into appropriate channel bins, as well as the time of arrival obtained by the ADC. This near-future solution would be applicable not only to single photon interferometry, but also optical communication, quantum key distribution and other well-established fields that utilize similar technology including LIDAR and medical imaging. As of current time, to the best of the author's knowledge, no such commercially available system exists.

8.4 Single Photon Interferometry Array

Currently established optical observatories could, in principle, be retrofitted with single-photon devices. Multiple sites throughout the world can be turned into a telescope array. Although free space synchronization has yet to be demonstrated for this application, the path forward is bright and promising. However, a dedicated telescope array should be constructed.

As shown in Chapter 4, ideal telescopes will have a diameter of 2 meters or less. As has been shown, commercial telescopes can be used to measure the $\Gamma^{(2)}$ Weiss *et al.* (2018). This result gives significant flexibility in terms of designing the array.

Because the cost of telescopes scales non-linearly with the size, smaller, commercial units should be deployed. Their separation and therefore the projected baseline could easily be modified to optimize the UV-plane coverage based on the target that is being observed. Optimized configuration can be made to further constrain the derived $\Gamma^{(2)}$ function, being though sparser sampling along the curve or redundant baselines providing smaller error bars.

Introduction of additional telescopes will also increase the number of samples acquired, since the scalability of such an array is *favorable* to numbers over the collecting area. Such a feat would be difficult to achieve unless adequately funded, and the outstanding issue such as free space synchronization are resolved. Nevertheless, the future of single photon interferometry and quantum astronomy as a whole is looking brighter every night.

Baines, E. K., M. P. Döllinger, F. Cusano, E. W. Guenther, A. P. Hatzes, H. A. McAlister, T. A. ten Brummelaar, N. H. Turner, J. Sturmann, L. Sturmann, P. J. Goldfinger, C. D. Farrington and S. T. Ridgway, "Angular Diameters and Effective Temperatures of 25 K Giant Stars from the CHARA Array", ApJ **710**, 1365–1374 (2010).

Bakos, G., J. Lazar, I. Papp, P. Sari and E. M. Green, "System description and first light curves of the hungarian automated telescope, an autonomous observatory for variability search", Publications of the Astronomical Society of the Pacific **114**, 799, 974 (2002).

Basu, S., W. J. Chaplin and Y. Elsworth, "Determination of Stellar Radii from Asteroseismic Data", ApJ **710**, 1596–1609 (2010).

Beckers, J. M., "Adaptive optics for astronomy: principles, performance, and applications", Annual review of astronomy and astrophysics **31**, 1, 13–62 (1993).

Belikov, R., A. Give'on, B. Kern, E. Cady, M. Carr, S. Shaklan, K. Balasubramanian, V. White, P. Echternach, M. Dickie *et al.*, "Demonstration of high contrast in 10% broadband light with the shaped pupil coronagraph", in "Proc. SPIE", vol. 6693, p. 66930Y (2007).

Bergeron, H., L. C. Sinclair, W. C. Swann, C. W. Nelson, J.-D. Deschênes, E. Baumann, F. R. Giorgetta, I. Coddington and N. R. Newbury, "Tight real-time synchronization of a microwave clock to an optical clock across a turbulent air path", Optica **3**, 4, 441–447, URL `http://www.osapublishing.org/optica/abstract.cfm?URI=optica-3-4-441` (2016).

Bessell, M., "Ubvri photometry ii: the cousins vri system, its temperature and absolute flux calibration, and relevance for two-dimensional photometry.", Publications of the Astronomical Society of the Pacific **91**, 543, 589 (1979).

Bliven, S., "Airy Disk airy disk", (5 March 2014).

Borucki, W. J., D. Koch, G. Basri, N. Batalha, T. Brown, D. Caldwell, J. Caldwell, J. Christensen-Dalsgaard, W. D. Cochran, E. DeVore *et al.*, "Kepler planet-detection mission: introduction and first results", Science **327**, 5968, 977–980 (2010).

Boyajian, T. S., H. A. McAlister, G. van Belle, D. R. Gies, T. A. ten Brummelaar, K. von Braun, C. Farrington, P. J. Goldfinger, D. O'Brien, J. R. Parks, N. D. Richardson, S. Ridgway, G. Schaefer, L. Sturmann, J. Sturmann, Y. Touhami, N. H. Turner and R. White, "Stellar Diameters and Temperatures. I. Main-sequence A, F, and G Stars", ApJ **746**, 101 (2012a).

Boyajian, T. S., K. von Braun, G. van Belle, C. Farrington, G. Schaefer, J. Jones, R. White, H. A. McAlister, T. A. ten Brummelaar, S. Ridgway, D. Gies, L. Sturmann, J. Sturmann, N. H. Turner, P. J. Goldfinger and N. Vargas, "Stellar Diameters and Temperatures. III. Main-sequence A, F, G, and K Stars: Additional High-precision Measurements and Empirical Relations", ApJ **771**, 40 (2013).

Boyajian, T. S., K. von Braun, G. van Belle, H. A. McAlister, T. A. ten Brummelaar, S. R. Kane, P. S. Muirhead, J. Jones, R. White, G. Schaefer, D. Ciardi, T. Henry, M. López-Morales, S. Ridgway, D. Gies, W.-C. Jao, B. Rojas-Ayala, J. R. Parks, L. Sturmann, J. Sturmann, N. H. Turner, C. Farrington, P. J. Goldfinger and D. H. Berger, "Stellar Diameters and Temperatures. II. Main-sequence K- and M-stars", ApJ **757**, 112 (2012b).

Braunstein, S. L. and C. M. Caves, "Statistical distance and the geometry of quantum states", Phys. Rev. Lett. **72**, 3439–3443, URL `http://link.aps.org/doi/10.1103/PhysRevLett.72.3439` (1994).

Bronzi, D., F. Villa, S. Tisa, A. Tosi and F. Zappa, "Spad figures of merit for photon-counting, photon-timing, and imaging applications: A review", IEEE Sensors Journal **16**, 3–12, URL `http://ieeexplore.ieee.org/xpl/articleDetails.jsp?arnumber=7283534` (2016).

Brown, R. H. and R. Twiss, "A test of a new type of stellar interferometer on sirius", Nature **178**, 4541, 1046–1048 (1956a).

Brown, R. H. and R. Q. Twiss, "Correlation between photons in two coherent beams of light", Nature **177**, 4497, 27–29 (1956b).

Campins, H., G. Rieke and M. Lebofsky, "Absolute calibration of photometry at 1 through 5 microns", The Astronomical Journal **90**, 896–899 (1985).

CASPER, "Casper-collaboration for astronomy signal processing and electronics research", `https://casper.berkeley.edu/`. (2009).

CASPER, "Roach2 wiki", `https://casper.berkeley.edu/wiki/ROACH2` (2013).

Che, X., J. Monnier, M. Zhao, E. Pedretti, N. Thureau, A. Mérand, T. Ten Brummelaar, H. McAlister, S. Ridgway, N. Turner *et al.*, "Colder and hotter: Interferometric imaging of β cassiopeiae and α leonis", The Astrophysical Journal **732**, 2, 68 (2011).

Chelli, A., L. Bourges, G. Duvert, S. Lafrasse, G. Mella, J.-B. Le Bouquin and O. Chesneau, "A robust approach to estimate stellar angular diameters from photometry and spectral type", in "Optical and Infrared Interferometry IV", vol. 9146 of *Proc. SPIE*, p. 91462Z (2014).

Colavita, M., J. Wallace, B. Hines, Y. Gursel, F. Malbet, D. Palmer, X. Pan, M. Shao, J. Yu, A. Boden *et al.*, "The palomar testbed interferometer", The Astrophysical Journal **510**, 1, 505 (1999).

Cova, S., A. Longoni and A. Andreoni, "Towards picosecond resolution with single-photon avalanche diodes", Review of Scientific Instruments **52**, 408–412 (1981).

Davis, J., M. Ireland, J. North, J. G. Robertson, W. Tango and P. G. Tuthill, "The angular diameter and fundamental parameters of sirius a", Publications of the Astronomical Society of Australia **28**, 1, 58–65 (2011).

Deschênes, J.-D., L. C. Sinclair, F. R. Giorgetta, W. C. Swann, E. Baumann, H. Bergeron, M. Cermak, I. Coddington and N. R. Newbury, "Synchronization of distant optical clocks at the femtosecond level", Phys. Rev. X **6** (2016).

Dragomir, D., S. R. Kane, G. W. Henry, D. R. Ciardi, D. A. Fischer, A. W. Howard, E. L. Jensen, G. Laughlin, S. Mahadevan, J. M. Matthews *et al.*, "The hd 192263 system: planetary orbital period and stellar variability disentangled", The Astrophysical Journal **754**, 1, 37 (2012).

Dragomir, D., S. R. Kane, G. Pilyavsky, S. Mahadevan, D. R. Ciardi, J. Z. Gazak, D. M. Gelino, A. Payne, M. Rabus, S. V. Ramirez *et al.*, "Terms photometry of known transiting exoplanets", The Astronomical Journal **142**, 4, 115 (2011).

Dravins, D., T. Lagadec and P. D. Nuñez, "Optical aperture synthesis with electronically connected telescopes", Nature communications **6**, 6852 (2015).

Dravins, D. and S. LeBohec, "Toward a diffraction-limited square-kilometer optical telescope: Digital revival of intensity interferometry", in "Extremely Large Telescopes: Which Wavelengths? Retirement Symposium for Arne Ardeberg", vol. 6986, p. 698609 (International Society for Optics and Photonics, 2008).

Dravins, D., S. LeBohec, H. Jensen, P. D. Nuñez, C. Consortium *et al.*, "Optical intensity interferometry with the cherenkov telescope array", Astroparticle Physics **43**, 331–347 (2013).

Ducati, J. R., "VizieR Online Data Catalog: Catalogue of Stellar Photometry in Johnson's 11-color system.", VizieR Online Data Catalog **2237** (2002).

Erkmen, B. I., Z. W. Barber and J. Dahl, "Maximum-likelihood estimation for frequency-modulated continuous-wave laser ranging using photon-counting detectors", Applied optics **52**, 10, 2008–2018 (2013).

Excelitas, *Single Photon Counting Module*, Excelitas Technologies (2016).

Farnham, T. L., D. G. Schleicher and M. F. A'Hearn, "The hb narrowband comet filters: Standard stars and calibrations", Icarus **147**, 1, 180–204 (2000).

Foo, G., D. M. Palacios and G. A. Swartzlander, "Optical vortex coronagraph", Optics letters **30**, 24, 3308–3310 (2005).

Gao, W., D. Gao, C. Hu-Guo and Y. Hu, "Integrated high-resolution multi-channel time-to-digital converters (tdcs) for pet imaging", in "Biomedical Engineering, Trends in Electronics, Communications and Software", (InTech, 2011).

Gol'tsman, G. N., O. Okunev, G. Chulkova, A. Lipatov, A. Semenov, K. Smirnov, B. Voronov, A. Dzardanov, C. Williams and R. Sobolewski, "Picosecond superconducting single-photon optical detector", Applied Physics Letters **79**, 6, 705–707, URL `http://scitation.aip.org/content/aip/journal/apl/79/6/10.1063/1.1388868` (2001).

Gol'Tsman, G., O. Okunev, G. Chulkova, A. Lipatov, A. Semenov, K. Smirnov, B. Voronov, A. Dzardanov, C. Williams and R. Sobolewski, "Picosecond superconducting single-photon optical detector", Applied physics letters **79**, 6, 705–707 (2001).

Guerin, W., A. Dussaux, M. Fouché, G. Labeyrie, J.-P. Rivet, D. Vernet, F. Vakili and R. Kaiser, "Temporal intensity interferometry: photon bunching in three bright stars", Monthly Notices of the Royal Astronomical Society **472**, 4, 4126–4132 (2017).

Guerin, W., J.-P. Rivet, M. Fouché, G. Labeyrie, D. Vernet, F. Vakili and R. Kaiser, "Spatial intensity interferometry on three bright stars", arXiv preprint arXiv:1805.06653 (2018).

Guyon, O., "Phase-induced amplitude apodization of telescope pupils for extrasolar terrestrial planet imaging", Astronomy and Astrophysics **404**, 1, 379–387 (2003).

Hamamatsu, *Photomultiplier tube R13089 Datasheet*, Hamamatsu (2016).

Hanbury Brown, R., J. Davis and L. Allen, "The angular diameters of 32 stars", Monthly Notices of the Royal Astronomical Society **167**, 1, 121–136 (1974).

Hanbury Brown, R. and R. Q. Twiss, "Interferometry of the Intensity Fluctuations in Light. I. Basic Theory: The Correlation between Photons in Coherent Beams of Radiation", Royal Society of London Proceedings Series A **242**, 300–324 (1957).

Helstrom, C. W., *Quantum detection and estimation theory* (Academic press, 1976).

Henry, G. W., S. R. Kane, S. X. Wang, J. T. Wright, T. S. Boyajian, K. von Braun, D. R. Ciardi, D. Dragomir, C. Farrington, D. A. Fischer *et al.*, "Host star properties and transit exclusion for the hd 38529 planetary system", The Astrophysical Journal **768**, 2, 155 (2013).

Hicks, B. A., M. R. Bolcar, M. A. Helmbrecht, P. Petrone, E. Burke, J. Corsetti, T. Dillon, A. Lea, S. Pellicori, T. Sheets *et al.*, "Segmented aperture interferometric nulling testbed (saint) ii: component systems update", in "Techniques and Instrumentation for Detection of Exoplanets VIII", vol. 10400, p. 104001I (International Society for Optics and Photonics, 2017).

Hinkel, N. R., S. R. Kane, G. Pilyavsky, T. S. Boyajian, D. J. James, D. Naef, D. A. Fischer and S. Udry, "A new analysis of the exoplanet hosting system hd 6434", The Astronomical Journal **150**, 6, 169 (2015).

Hinkel, N. R., F. Timmes, P. A. Young, M. D. Pagano and M. C. Turnbull, "Stellar abundances in the solar neighborhood: the hypatia catalog", The Astronomical Journal **148**, 3, 54 (2014).

Hoffleit, D. and C. Jaschek, *The Bright star catalogue* (1991).

Homulle, H., "Implementing the tdc - delay line", `http://cas.tudelft.nl/fpga_tdc/TDC_basic.html` (2015).

Horch, E. P., "Cutting the cord: toward wireless optical intensity interferometry", URL `http://dx.doi.org/10.1117/12.2179146` (2015).

Horch, E. P., S. A. Weiss, J. D. Rupert, A. J. DiMaio, D. A. Nusdeo, P. Peronio, I. Rech, A. Gulinatti and A. Giudice, "Scsi: the southern connecticut stellar interferometer", in "Optical and Infrared Interferometry and Imaging V", vol. 9907, p. 99071W (International Society for Optics and Photonics, 2016).

Husser, T.-O., S. Wende-von Berg, S. Dreizler, D. Homeier, A. Reiners, T. Barman and P. H. Hauschildt, "A new extensive library of phoenix stellar atmospheres and synthetic spectra", Astronomy & Astrophysics **553**, A6 (2013).

Jiang, L. A. and J. X. Luu, "Heterodyne detection with a weak local oscillator", Applied optics **47**, 10, 1486–1503 (2008).

Keesey, L., "Nasa seeks picometer accuracy", URL `https://www.nasa.gov/feature/goddard/2016/nasa-seeks-picometer-accuracy` (2016).

Labeyrie, A., S. G. Lipson and P. Nisenson, *An introduction to optical stellar interferometry* (Cambridge University Press, 2006).

Le Bohec, S. and J. Holder, "Optical intensity interferometry with atmospheric cerenkov telescope arrays", The Astrophysical Journal **649**, 1, 399 (2006).

Le Coarer, E., A. Chalabaev and G. Duvert, "Prospects of optical heterodyne detection for astronomy and one photon interferometry", (????).

Ligi, R., O. Creevey, D. Mourard, A. Crida, A.-M. Lagrange, N. Nardetto, K. Perraut, M. Schultheis, I. Tallon-Bosc and T. ten Brummelaar, "Radii, masses, and ages of 18 bright stars using interferometry and new estimations of exoplanetary parameters", AAP **586**, A94 (2016).

Lyon, R. G., M. Clampin, R. Woodruff, G. Vasudevan, M. Shao, M. Levine, G. Melnick, V. Tolls, P. Petrone, P. Dogoda *et al.*, "Visible nulling coronagraphy for exo-planetary detection and characterization", Proceedings of the International Astronomical Union **1**, C200, 345–352 (2005).

Mach, L., "Ueber einen interferenzrefraktor", Zeitschrift für Instrumentenkunde **12**, 89–93 (1892).

Malvimat, V., O. Wucknitz and P. Saha, "Intensity interferometry with more than two detectors?", Monthly Notices of the Royal Astronomical Society **437**, 1, 798–803 (2013).

Matthews, N., O. Clarke, S. Snow, S. LeBohec and D. Kieda, "Implementation of an intensity interferometry system on the starbase observatory", in "Optical and Infrared Interferometry and Imaging VI", vol. 10701, p. 107010W (International Society for Optics and Photonics, 2018a).

Matthews, N., D. Kieda and S. LeBohec, "Development of a digital astronomical intensity interferometer: laboratory results with thermal light", Journal of Modern Optics **65**, 11, 1336–1344 (2018b).

McGaugh, S., G. Wirth, S. H and K. R, "Photon flux", (no-date).

Michelson, A. A. and E. W. Morley, "On the Relative Motion of the Earth and of the Luminiferous Ether", Sidereal Messenger, vol. 6, pp.306-310 **6**, 306–310 (1887).

Michelson, A. A. and E. W. Morley, "On the relative motion of the earth and of the luminiferous ether", Sidereal Messenger, vol. 6, pp. 306-310 **6**, 306–310 (1887).

Michelson, A. A. and F. G. Pease, "Measurement of the diameter of alpha-orionis by the interferometer", Proceedings of the National Academy of Sciences **7**, 5, 143–146 (1921).

Michelson, A. A. and F. G. Pease, "Measurement of the diameter of alpha Orionis with the interferometer.", ApJ **53** (1921).

Monnier, J., "CHARA stars chara stars", (2015).

Monnier, J., "CHARA Interferometer chara interferometer", (unknown).

Monnier, J. D., "Optical interferometry in astronomy", Reports on Progress in Physics **66**, 5, 789 (2003).

Monnier, J. D., M. Zhao, E. Pedretti, N. Thureau, M. Ireland, P. Muirhead, J.-P. Berger, R. Millan-Gabet, G. Van Belle, T. Ten Brummelaar *et al.*, "Imaging the surface of altair", Science **317**, 5836, 342–345 (2007).

Morgan, S., "Stellar temperatures", (no-date).

Nair, R. and M. Tsang, "Interferometric superlocalization of two incoherent optical point sources", Optics express **24**, 4, 3684–3701 (2016).

Naletto, G., Barbieri, C., Occhipinti, T., Capraro, I., Di Paola, A., Facchinetti, C., Verroi, E., Zoccarato, P., Anzolin, G., Belluso, M., Billotta, S., Bolli, P., Bonanno, G., Da Deppo, V., Fornasier, S., Germanà, C., Giro, E., Marchi, S., Messina, F., Pernechele, C., Tamburini, F., Zaccariotto, M. and Zampieri, L., "Iqueye, a single photon-counting photometer applied to the eso new technology telescope", A and A **508**, 1, 531–539, URL `http://dx.doi.org/10.1051/0004-6361/200912862` (2009).

Narasimman, R., A. Prabhakar and N. Chandrachoodan, "Implementation of a 30 ps resolution time to digital converter in fpga", in "Electronic Design, Computer Networks and Automated Verification (EDCAV), 2015 International Conference on", pp. 12–17 (IEEE, 2015).

Ngeyaabwe, V. K., "Coherent and Incoherent light coherent and incoherent light", (22 Dec 2014).

Nunez, P. D., S. LeBohec, D. Kieda, R. Holmes, H. Jensen and D. Dravins, "Stellar intensity interferometry: imaging capabilities of air cherenkov telescope arrays", in "Optical and Infrared Interferometry II", vol. 7734, p. 77341C (International Society for Optics and Photonics, 2010).

Osborn, J., D. Föhring, V. Dhillon and R. Wilson, "Atmospheric scintillation in astronomical photometry", Monthly Notices of the Royal Astronomical Society **452**, 2, 1707–1716 (2015).

Padula, S. S., "Hbt interferometry: historical perspective", Brazilian journal of physics **35**, 1, 70–99 (2005).

Perryman, M., *The exoplanet handbook* (Cambridge University Press, 2011).

PHASE, C., "Setting new standards with harps", The Messenger **114**, 20 (2003).

Pickles, A., "A stellar spectral flux library: 1150–25000 å", Publications of the Astronomical Society of the Pacific **110**, 749, 863 (1998).

Pilyavsky, G., S. Mahadevan, S. R. Kane, A. W. Howard, D. R. Ciardi, C. De Pree, D. Dragomir, D. Fischer, G. W. Henry, E. L. Jensen *et al.*, "A search for the transit of hd 168443b: Improved orbital parameters and photometry", The Astrophysical Journal **743**, 2, 162 (2011).

Pilyavsky, G., P. Mauskopf, N. Smith, E. Schroeder, A. Sinclair, G. T. van Belle, N. Hinkel and P. Scowen, "Single-photon intensity interferometry (spiify): utilizing available telescopes", Monthly Notices of the Royal Astronomical Society **467**, 3, 3048–3055 (2017).

Rakhmanov, M., "Demodulation of intensity and shot noise in the optical heterodyne detection of laser interferometers for gravitational waves", Applied optics **40**, 36, 6596–6605 (2001).

Ray, J. and K. Senior, "Geodetic techniques for time and frequency comparisons using gps phase and code measurements", Metrologia **42**, 4, 215, URL `http://stacks.iop.org/0026-1394/42/i=4/a=005` (2005).

Rayleigh, L., "Xxxi. investigations in optics, with special reference to the spectroscope", The London, Edinburgh, and Dublin Philosophical Magazine and Journal of Science **8**, 49, 261–274 (1879).

Ricarte, A. and J. Dexter, "The event horizon telescope: exploring strong gravity and accretion physics", Monthly Notices of the Royal Astronomical Society **446**, 2, 1973–1987 (2014).

Schneider, D., J. Gunn and J. Hoessel, "Ccd photometry of abell clusters. i-magnitudes and redshifts for 84 brightest cluster galaxies", The Astrophysical Journal **264**, 337–355 (1983).

Schworer, G. and P. G. Tuthill, "Predicting exoplanet observability in time, contrast, separation, and polarization, in scattered light", Astronomy and Astrophysics **578**, A59 (2015).

Ségransan, D., "Observability and UV coverage", New Astron. Rev. **51**, 597–603 (2007).

Semenov, A. D., G. N. Gol'tsman and A. A. Korneev, "Quantum detection by current carrying superconducting film", Physica C: Superconductivity **351**, 4, 349 – 356, URL `http://www.sciencedirect.com/science/article/pii/S0921453400016373` (2001a).

Semenov, A. D., G. N. Gol'tsman and A. A. Korneev, "Quantum detection by current carrying superconducting film", Physica C: Superconductivity **351**, 4, 349–356 (2001b).

Shipman, H. L., "Masses and radii of white-dwarf stars. iii-results for 110 hydrogen-rich and 28 helium-rich stars", The Astrophysical Journal **228**, 240–256 (1979).

Sinclair, A., G. Pilyavsky, E. Schroeder and P. Mauskopf, "Fpga-based tdc for single-photon intensity interferometry", Journal of Astronomical Instrumentation **5**, 04, 1641016 (2016).

Soni, Z., A. Patel, D. K. Panda and A. B. Sarbadhikari, "Comparative study of delay line based time to digital converter using fpga", (2017).

spaceblanket, "NPOI Interferometer npoi interferometer", (18 April 2009).

Stipčević, M., H. Skenderović and D. Gracin, "Characterization of a novel avalanche photodiode for single photon detection in VIS-NIR range", Optics Express **18**, 17448 (2010).

Street, R., D. Pollaco, A. Fitzsimmons, F. Keenan, K. Horne, S. Kane, A. Collier Cameron, T. Lister, C. Haswell, A. Norton *et al.*, "Superwasp: wide angle search for planets", in "Scientific Frontiers in Research on Extrasolar Planets", vol. 294, pp. 405–408 (2003).

Tan, P. K., A. H. Chan and C. Kurtsiefer, "Optical Intensity Interferometry through Atmospheric Turbulence", ArXiv e-prints (2015).

Tan, P. K., G. H. Yeo, H. S. Poh, A. H. Chan and C. Kurtsiefer, "Measuring Temporal Photon Bunching in Blackbody Radiation", ApJ letters **789**, L10 (2014).

Trauger, J., D. Moody, B. Gordon, J. Krist and D. Mawet, "A hybrid lyot coronagraph for the direct imaging and spectroscopy of exoplanet systems: recent results and prospects", (Society of Photo-Optical Instrumentation Engineers (SPIE), 2011).

Tsang, M., "Conservative error measures for classical and quantum metrology", arXiv preprint arXiv:1605.03799 (2016).

Tsang, M., R. Nair and X.-M. Lu, "Quantum theory of superresolution for two incoherent optical point sources", Physical Review X **6**, 3, 031033 (2016).

Underhill, A. B., L. Divan, M.-L. Prevot-Burnichon and V. Doazan, "Effective temperatures, angular diameters, distances and linear radii for 160 O and B stars", Monthly Notices of the Royal Astronomical Society **189**, 601–605 (1979).

Van Belle, G., M. Creech-Eakman and A. Hart, "Supergiant temperatures and linear radii from near-infrared interferometry", Monthly Notices of the Royal Astronomical Society **394**, 4, 1925–1935 (2009).

Van Belle, G. T., C. Paladini, B. Aringer, J. Hron and D. Ciardi, "The pti carbon star angular size survey: effective temperatures and non-sphericity", The Astrophysical Journal **775**, 1, 45 (2013).

van Cittert, P. H., "Die wahrscheinliche schwingungsverteilung in einer von einer lichtquelle direkt oder mittels einer linse beleuchteten ebene", Physica **1**, 1-6, 201–210 (1934).

van Leeuwen, F., "Validation of the new Hipparcos reduction", aap **474**, 653–664 (2007).

Verma, V. B., B. Korzh, F. Bussières, R. D. Horansky, S. D. Dyer, A. E. Lita, I. Vayshenker, F. Marsili, M. D. Shaw, H. Zbinden, R. P. Mirin and S. W. Nam, "High-efficiency superconducting nanowire single-photon detectors fabricated from mosi thin-films", Opt. Express **23**, 26, 33792–33801, URL `http://www.opticsexpress.org/abstract.cfm?URI=oe-23-26-33792` (2015).

von Braun, K., T. S. Boyajian, G. T. van Belle, S. R. Kane, J. Jones, C. Farrington, G. Schaefer, N. Vargas, N. Scott, T. A. ten Brummelaar, M. Kephart, D. R. Gies, D. R. Ciardi, M. López-Morales, C. Mazingue, H. A. McAlister, S. Ridgway, P. J. Goldfinger, N. H. Turner and L. Sturmann, "Stellar diameters and temperatures - V. 11 newly characterized exoplanet host stars", MNRAS **438**, 2413–2425 (2014).

Weiss, S. A., J. D. Rupert and E. P. Horch, "Stellar photon correlation detection with the southern connecticut stellar interferometer", in "Optical and Infrared Interferometry and Imaging VI", vol. 10701, p. 107010X (International Society for Optics and Photonics, 2018).

Wicker, K., S. Sindbert and R. Heintzmann, "Characterisation of a resolution enhancing image inversion interferometer", Optics express **17**, 18, 15491–15501 (2009).

Zadeh, I. E., J. W. Los, R. Gourgues, G. Bulgarini, S. M. Dobrovolskiy, V. Zwiller and S. N. Dorenbos, "A single-photon detector with high efficiency and sub-10ps time resolution", arXiv preprint arXiv:1801.06574 (2018).

Zampieri, L., G. Naletto, C. Barbieri, M. Barbieri, E. Verroi, G. Umbriaco, P. Favazza, L. Lessio and G. Farisato, "Intensity Interferometry with Aqueye+ and Iqueye in Asiago", ArXiv e-prints (2016).

Zampieri, L., G. Naletto, C. Barbieri, E. Verroi, M. Barbieri, G. Ceribella, M. D'Alessandro, G. Farisato, A. Di Paola and P. Zoccarato, "Aqueye+: a new ultrafast single photon counter for optical high time resolution astrophysics", in "Photon Counting Applications 2015", vol. 9504 of *SPIE*, p. 95040C (2015).

Zehnder, L., *Ein neuer interferenzrefraktor* (Springer, 1891).

Zernike, F., "The concept of degree of coherence and its application to optical problems", Physica **5**, 8, 785–795 (1938).

Zhang, M., H. Wang and Y. Liu, "A 7.4 ps fpga-based tdc with a 1024-unit measurement matrix", Sensors **17**, 4, 865 (2017).

Zhao, M., J. Monnier, E. Pedretti, N. Thureau, A. Mérand, T. Ten Brummelaar, H. McAlister, S. Ridgway, N. Turner, J. Sturmann *et al.*, "Imaging and modeling rapidly rotating stars: α cephei and α ophiuchi", The Astrophysical Journal **701**, 1, 209 (2009).

APPENDIX A

TEMPERATURE DERIVATION THROUGH SED FITTING

A.1 The PTI Project Overview

The Palomar Testbed Interferometer [1] (PTI) was located in Palomar Observatory, San Diago County, CA and was in operation between 1997 and 2008. It was composed of 3 telescopes with 0.4 m apertures, producing 85 to 110 m baselines, which provided an angular resolution of 0.75 mas for wavelengths 1.6 and 2.2 μm Colavita *et al.* (1999). This analysis contains data acquired during its lifespan.

The program undertaken at this facility involved observations of many evolved stars. The focus of the PTI Giants survey, for which photometry was acquired in order to obtain spectral energy density (SED) and ultimately, effective temperature (T_{eff}), involves objects that are believed to be Giant stars; Supergiants (Van Belle *et al.*, 2009) and carbon stars (Van Belle *et al.*, 2013) have already been published. The survey contains over 220 stars, with limiting apparent magnitude of $m_K < 5$.

A.2 Bolometric fluxes

In order to derive the stellar effective temperature (T_{eff}) bolometric fluxes (F_{BOL}) were needed along with the angular size (Ω) measured by the PTI interferometer. The effective temperature can be described in terms of F_{BOL} and Ω as

$$T_{EFF} = 2341(F_{BOL}/\Omega^2)^{1/4} \tag{A.1}$$

The value of F_{BOL} represents the total integrated flux, across the entire spectrum. However, the majority of the emitted energy resides at the ultraviolet, optical and infrared portion of the spectrum. There are two significant issues related to measuring F_{BOL}.

First, sources of extinction, which are wavelength dependent, will reduce the amounts of photons observed. The sources of absorption can be induced by the

[1] Built by Caltech and Jet Propulsion Laboratory

stellar atmosphere, circumstellar material, interstellar medium as well as the Earths atmosphere. The atmospheric effects can be mitigated by using other bright stars as references/calibrators, for which high precision bolometric flux has been measured, with near-simultaneous observations of the target.

The second issue with measuring the bolometric flux is that it is rarely done as a full, continuous spectrum. A much more accessible approach to the problem is to obtain the flux at different wavelengths, with narrow and broadband filters. The broadband photometry is easy to acquire due to high photon throughput. On the other hand, the narrowband photometry allows for disentangling the degeneracies in the T_{eff} solution due to interstellar, circumstellar or interstellar extinctions.

Once the photometry is in hand, a spectral template is fit to these data. The necessity of this step is to interpolate or extrapolate over the not sampled wavelength regimes; a secondary purpose of this step is to fit for interstellar/circumstellar extinction.

A.3 Filters and calibration stars

The filters selected for the acquisition of photometric data cover the range of about 300 to 900 nanometers. Standard filter set of [U, B, V, R, I, K] were used to obtain the photometric data, along with a more specialized set of [OH, NH, UV*c*, CN, C3, CO+, B*c*, C2, G*c*, H2O+, R*c*], where *c* is a stand-in for "continuum". The specialized filter-set is described in greater detail by Farnham *et al.*, as well as providing calibrated magnitudes at these wavebands for the reference stars used in this analysis.

The reference stars and the calibrated magnitude was obtained from multiple sources, to be fully cited in the complete release of the PTI dataset. The entire set of reference stars is shown in Table B.1 and B.2, in Appendix B.

A.4 Photometric analysis

The photometric data pipeline was developed in IDL, developed and maintained during the authors undergraduate and early graduate programs, utilizes the DAOPHOT routine. The "fits" image files from Lowell Observatory in Flagstaff, AZ, were analyzed in mostly autonomous manner, since the pipeline has been previously tested and demonstrated for *relative* photometry to monitor stars with known exoplanets Henry *et al.* (2013),Dragomir *et al.* (2012), Pilyavsky *et al.* (2011), Dragomir *et al.* (2011), and is described with some detail in Hinkel *et al.* (2015).

The standard procedure of image reduction through bias and flat-fielding is performed to reduce instrumental noise for each filter type. For each night, a list of target and reference stars is maintained, along with their associated RA and DEC coordinates. Additionally, each science frame has its own RA and DEC values. A wrapper for Astrometry.net is used on each science frame to match and transform pixel coordinates to appropriate RA and DEC values to obtain coarse coordinates of the targets. A centroid fitting algorithm obtains a more precise center, and aperture photometry is performed by optimizing the point spread function fit and removing the background "sky" pixel values. The photoelectron count is then stored, along with the information regarding the filter type, star name or identifier, file of origin, and other metadata.

Comparison of photoelectrons from target stars to the reference stars is made for all available optical bands. The ratio of the photoelectrons between the target and the reference star is equal to the actual flux ratio of the stars. Since the reference stars have well-documented flux values, the resulting flux for the target can be used to determine the best spectral model to describe the star and the associated bolometric flux. Multiple science frames of a target star per night per filter at different airmass

values allow for fitting of atmospheric extinction coefficient and removal.

A.5 SED Fitting

Two approaches to SED fitting were considered for this project. One approach would utilize empirical spectral template from the INGS library [2] which are updated templates from (Pickles, 1998), while the other would rely on the use of modeled spectra from PHOENIX [3] (Husser *et al.*, 2013).

The advantage of INGS library is that templates are mostly model-independent, as it is based on actual numerical measurements. However, it is somewhat sparsely available in stellar T_{eff} and luminosity class.

On the other hand, the PHOENIX models are significantly denser in available T_{eff} and luminosity class. These synthetic templates are also not susceptible to any uncorrected extinction that could be present in the INGS data set.

The solution was to use the best of the two datasets and utilized the PHOENIX models that have been calibrated against the INGS spectra data. The INGS data was used as input spectrophotometry in the code, and the best fir PHOENIX model spectra were matched to the appropriate INGS template. This approach allowed for interpolation of T_{eff} in the sparser INGS dataset while maintaining the basis of empirical data.

A.6 Preliminary results

The bulk of the results will be published in the near future, by Gerard T. Van Belle. However, the preliminary results are auspicious, with T_{eff} accuracy of ± 50 degrees Kelvin (Van Belle, private communication). The data release will be in a

[2] https://lco.global/user/apickles/dev/INGS/

[3] http://phoenix.astro.physik.uni-goettingen.de/

catalog format, containing over 220 stars. It will also contain the angular size of the stars, and absolute photometry used to derive F_{bol} (See Figure A.1), and the effective temperature.

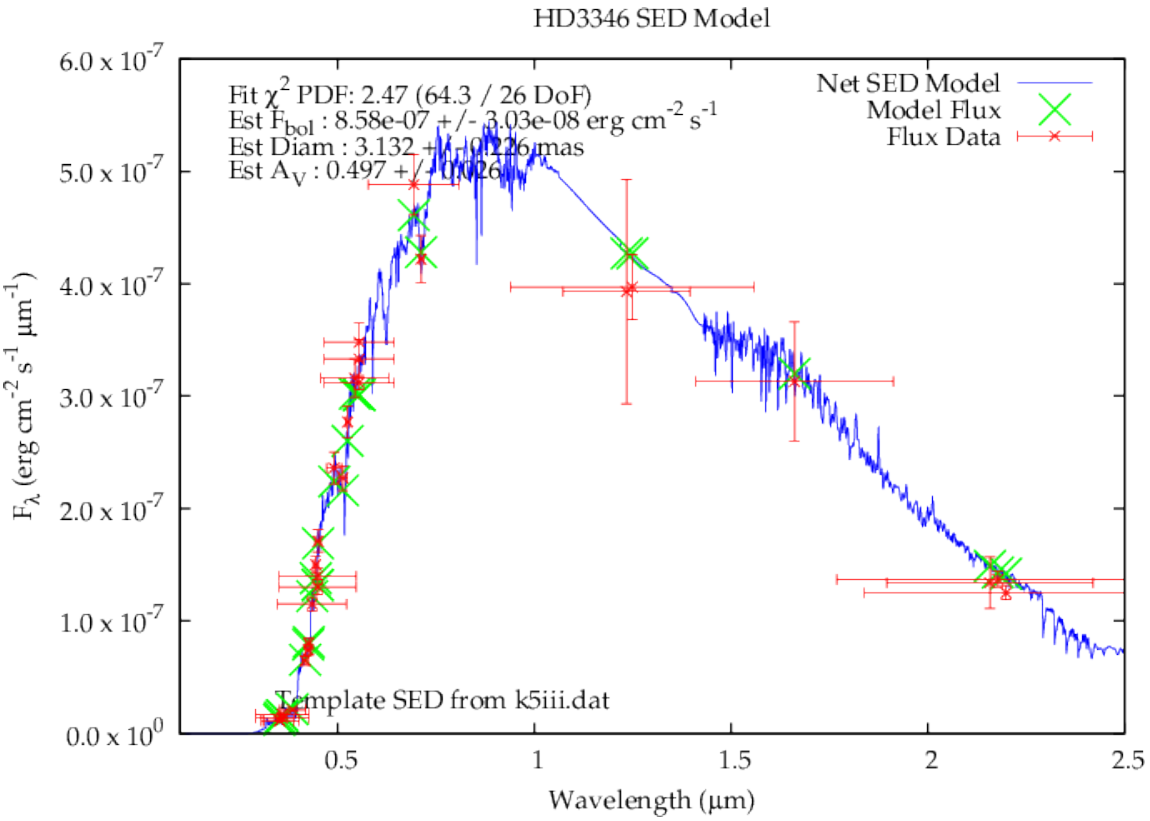

Figure A.1: Photometry at optical and near infrared wavelengths as collected by the PTI survey is shown in red, along with the error bars. The green exes denote the modeled flux, and the blue line corresponds to the SED model.

APPENDIX B

FULL TABLE OF REFERENCE STARS USED IN THE PTI GIANTS SURVEY

Identifier	U	B	V	R	I	K	OH	NH
BD+001237	13.24	12.151	10.787	10.013	9.287	7.346	nan	nan
BD+002580	nan	10.34	9.89	nan	nan	8.888	nan	nan
BD+002586	12.043	10.898	9.737	9.146	8.628	7.09	nan	nan
BD+002589	nan	10.39	9.97	nan	nan	8.885	nan	nan
BD+002717	10.822	10.567	9.903	9.537	9.206	8.432	nan	nan
BD+002854	nan	10.65	10.01	nan	nan	8.758	nan	nan
BD+002862	12.916	11.98	10.89	10.33	9.834	8.362	nan	nan
BD+00307	nan	9.98	9.55	nan	nan	8.489	nan	nan
BD+003222	12.729	11.15	9.786	9.056	8.412	6.548	nan	nan
BD+003224	12.132	10.647	9.341	8.665	8.073	6.324	nan	nan
BD+003552B	nan	nan	12.2	nan	nan	9.3	nan	nan
BD+004260	14.647	12.341	10.382	9.205	7.982	5.109	nan	nan
BD+004262	nan	11.4	10.6	nan	nan	8.442	nan	nan
BD+004265C	nan	nan	14.2	nan	nan	nan	nan	nan
BD+004763	nan	10.9	9.64	nan	nan	6.999	nan	nan
BD+004766	10.457	10.456	10.003	9.724	9.439	8.822	nan	nan
BD+004767	12.203	11.362	10.304	9.736	9.207	7.751	nan	nan
BD+004910	11.416	11.479	10.909	10.596	10.287	9.589	nan	nan
BD+005040	12.221	11.459	10.431	9.867	9.332	7.851	nan	nan
BD+00669p	13.802	12.509	11.216	10.524	9.905	8.14	nan	nan
BD+00669s	12.966	12.519	11.694	11.223	10.803	9.682	nan	nan
BD+041291B	nan	11.2	10.94	nan	nan	nan	nan	nan
BD+043508	nan	11.11	9.36	nan	nan	5.045	nan	nan
BD-001851	nan	10.31	9.62	nan	nan	7.59	nan	nan

Identifier	U	B	V	R	I	K	OH	NH
BD-001856	10.247	10.209	9.807	9.554	9.307	8.738	nan	nan
BD-002081	10.403	10.297	10.14	10.062	9.978	9.726	nan	nan
BD-002084	11.921	10.426	9.15	8.501	7.948	6.313	nan	nan
BD-002381	nan	10.36	9.89	9.66	9.493	8.683	nan	nan
BD-00288	nan	9.99	8.81	nan	nan	6.229	nan	nan
BD-00293	nan	10.26	9.83	nan	nan	8.519	nan	nan
BD-003152	11.064	10.882	10.702	10.602	10.493	10.131	nan	nan
BD-003353	12.387	10.798	9.333	8.546	7.839	5.862	nan	nan
BD-003356	11.189	10.962	10.353	9.977	9.584	8.719	nan	nan
BD-004069	nan	10.48	9.79	9.451	9.054	8.063	nan	nan
BD-004073	12.409	11.115	9.905	9.257	8.688	7.058	nan	nan
BD-004250	nan	10.62	9.48	nan	nan	6.879	nan	nan
BD-004251B	nan	9.76	9.14	nan	nan	7.581	nan	nan
BD-00454	nan	10.26	8.85	nan	nan	5.441	nan	nan
BD-004557	10.411	10.305	9.693	9.339	8.991	8.138	nan	nan
BD-00792	nan	10.2	9.68	nan	nan	8.159	nan	nan
BD-11162	9.987	11.102	11.184	11.133	11.039	10.62	nan	nan
EGGR70	11.851	12.847	13.012	13.138	13.278	13.833	nan	nan
GD246	11.578	12.772	13.09	13.238	13.418	14.075	nan	nan
GD71	11.675	12.783	13.032	13.169	13.337	14.115	nan	nan
GJ1142B	12.397	13.093	13.057	13.141	13.215	13.544	nan	nan
GSC00012-00675	13.672	12.828	11.782	11.22	10.699	9.263	nan	nan
GSC00048-00918	14.63	13.013	11.597	10.84	10.166	8.223	nan	nan
GSC00048-01015	12.136	12.028	11.725	11.549	11.363	10.942	nan	nan

Identifier	U	B	V	R	I	K	OH	NH
GSC00048-01221	13.704	12.423	11.204	10.545	9.959	8.284	nan	nan
GSC00085-00147	nan	12.36	11.92	11.6	nan	10.778	nan	nan
GSC00085-00158	14.203	13.057	11.719	10.984	10.287	8.413	nan	nan
GSC00511-01428	12.395	12.237	12.086	12.022	11.947	11.735	nan	nan
GSC00568-00830	13.003	12.828	12.095	11.674	11.271	10.237	nan	nan
GSC04737-00114	13.105	12.215	11.138	10.581	10.072	8.634	nan	nan
GSC04833-00591	12.989	12.157	11.152	10.621	10.145	8.803	nan	nan
GSC04833-00626	13.596	12.307	11.055	10.405	9.828	8.139	nan	nan
GSC04949-00865	nan	11.99	11.22	nan	nan	nan	nan	nan
GSC05048-00662	14.15	12.687	11.307	10.564	9.899	7.99	nan	nan
HD100340	8.906	9.881	10.115	10.219	10.353	10.801	nan	nan
HD103486	nan	8.75	8.36	nan	nan	7.322	nan	nan
HD103646	10.172	10.229	9.859	9.629	9.394	8.883	nan	nan
HD110281	12.628	10.962	9.37	8.538	7.779	5.775	nan	nan
HD110411	nan	4.951	4.872	nan	4.8	4.678	nan	nan
HD110572	10.146	10.181	9.705	9.417	9.126	8.455	nan	nan
HD11131	7.49	7.39	6.75	6.39	6.04	5.15	8.87	8.298
HD111397	nan	5.727	5.702	nan	nan	5.566	nan	nan
HD111469	nan	5.804	5.756	nan	nan	5.617	nan	nan
HD115735	nan	5.08	5.15	nan	nan	5.244	nan	nan
HD116160	nan	5.735	5.693	nan	5.64	5.509	nan	nan
HD118246	7.31	7.88	8.01	nan	nan	8.479	nan	nan
HD118280	nan	10.22	8.82	8.054	7.379	5.445	nan	nan
HD118290	nan	9.88	8.32	nan	nan	4.638	nan	nan

Identifier	U	B	V	R	I	K	OH	NH
HD118330	nan	7.59	7.04	6.749	6.438	5.69	nan	nan
HD118390	nan	9.38	8.35	nan	nan	5.94	nan	nan
HD1185	nan	6.2	6.15	nan	nan	6.022	nan	nan
HD118526	nan	9.05	8.72	nan	nan	7.831	nan	nan
HD118579	nan	9.39	9.18	nan	nan	8.508	nan	nan
HD118850	nan	10.38	9.44	nan	nan	7.076	nan	nan
HD11983	nan	9.7	8.21	nan	nan	4.62	nan	nan
HD120086	6.92	7.65	7.82	nan	nan	8.41	7.414	7.444
HD12021	nan	8.79	8.85	nan	nan	9.145	nan	nan
HD120934	nan	6.144	6.098	nan	nan	5.956	nan	nan
HD121968	9.16	10.071	10.256	10.33	10.429	10.774	nan	nan
HD121996	nan	5.753	5.756	nan	nan	5.704	nan	nan
HD122365	nan	6.062	5.981	nan	nan	5.697	nan	nan
HD124224	nan	4.89	5.01	nan	nan	5.285	nan	nan
HD12471	nan	5.555	5.516	nan	nan	5.335	nan	nan
HD126129	nan	5.1	5.12	nan	nan	nan	nan	nan
HD1280	nan	4.679	4.619	nan	nan	4.416	nan	nan
HD128866	nan	9.76	9.09	8.6	nan	7.501	nan	nan
HD129002	nan	5.423	5.395	nan	nan	5.26	nan	nan
HD129230	nan	9.15	8.12	7.6	nan	5.688	nan	nan
HD129727	9.803	9.855	9.477	9.244	9.009	8.524	nan	nan
HD129956	nan	5.66	5.67	nan	nan	5.6	6.637	6.523
HD129988	nan	5.2	5.12	nan	nan	nan	nan	nan
HD13295	nan	6.03	6.1	nan	nan	6.609	nan	nan

Identifier	U	B	V	R	I	K	OH	NH
HD135502	nan	5.339	5.281	nan	nan	5.11	nan	nan
HD139197	9.591	9.435	9.036	8.804	8.578	8.021	nan	nan
HD139287	nan	9.04	8.44	nan	nan	6.83	nan	nan
HD139308	nan	9.06	7.76	nan	nan	4.809	nan	nan
HD139513	12.042	10.74	9.446	8.734	8.081	6.182	nan	nan
HD139840	nan	9.18	8.09	nan	nan	5.352	nan	nan
HD140159	nan	4.567	4.509	nan	nan	4.31	nan	nan
HD1404	nan	4.57	4.52	nan	nan	4.464	nan	nan
HD140729	nan	6.148	6.144	nan	nan	6.131	nan	nan
HD140850	nan	10.47	8.86	nan	nan	4.501	nan	nan
HD14191	nan	5.584	5.575	nan	nan	5.39	nan	nan
HD14212	nan	5.318	5.314	nan	nan	5.271	nan	nan
HD145122	nan	6.125	6.129	nan	nan	6.084	nan	nan
HD146233	nan	6.15	5.5	nan	nan	4.19	7.736	7.145
HD149363	6.94	7.75	7.77	nan	nan	7.73	7.536	7.517
HD149382	7.518	8.661	8.943	9.07	9.205	9.418	nan	nan
HD149506	9.671	9.588	9.208	8.983	8.759	8.223	nan	nan
HD14951	4.88	5.37	5.47	nan	nan	5.76	5.63	5.606
HD149616	nan	8.75	8.23	nan	nan	6.815	nan	nan
HD149825	10.639	10.023	9.059	8.537	8.039	6.643	nan	nan
HD149845	nan	9.26	7.96	nan	nan	4.935	nan	nan
HD149933	nan	8.829	8.053	7.6	7.2	6.29	nan	nan
HD151862	nan	5.94	5.91	nan	nan	5.855	nan	nan
HD154445	5.13	5.74	5.64	nan	nan	5.29	5.822	5.729

Identifier	U	B	V	R	I	K	OH	NH
HD156729	nan	4.663	4.624	nan	nan	4.438	nan	nan
HD157198	nan	5.125	5.126	nan	nan	nan	nan	nan
HD157778	nan	5.45	5.42	nan	nan	nan	nan	nan
HD159480	nan	5.833	5.793	nan	nan	5.634	nan	nan
HD160181	5.93	5.9	5.76	nan	nan	5.343	nan	nan
HD161304	nan	8.74	8.48	nan	nan	7.545	nan	nan
HD161427	nan	9.79	9.03	nan	nan	7.031	nan	nan
HD161833	5.65	5.64	5.61	nan	nan	5.452	nan	nan
HD161961	7.29	7.93	7.79	nan	nan	7.334	nan	nan
HD164577	nan	4.473	4.439	nan	nan	4.233	nan	nan
HD164852	4.57	5.15	5.25	nan	nan	5.49	5.207	5.2
HD165358	nan	6.282	6.238	nan	nan	6.088	nan	nan
HD16811	5.64	5.71	5.74	nan	nan	5.722	nan	nan
HD169111	6.08	6.03	5.98	nan	nan	5.767	nan	nan
HD169985	nan	5.71	5.21	nan	nan	3.39	nan	nan
HD170493	10.187	9.11	8.004	7.374	6.871	5.484	nan	nan
HD170783	nan	7.92	7.73	nan	nan	7.26	8.645	8.477
HD170878	nan	5.81	5.76	nan	nan	5.479	nan	nan
HD172651	nan	8.945	7.476	nan	nan	4.079	nan	nan
HD172652	10.457	10.333	10.025	9.854	9.671	9.233	nan	nan
HD172829	12.741	10.449	8.447	7.261	4.955	3.164	nan	nan
HD173495	nan	5.87	5.83	nan	nan	5.66	nan	nan
HD173637	8.97	9.45	9.29	nan	nan	7.652	nan	nan
HD174240	nan	6.274	6.236	nan	nan	6.04	nan	nan

Identifier	U	B	V	R	I	K	OH	NH
HD174262	nan	5.914	5.894	nan	nan	5.82	nan	nan
HD175544	6.81	7.45	7.35	nan	nan	7.227	nan	nan
HD179648	6.19	6.11	6.04	nan	nan	5.685	nan	nan
HD180782	nan	6.206	6.181	nan	nan	nan	nan	nan
HD181383	nan	6.12	6.023	nan	nan	5.767	nan	nan
HD18286	nan	9.22	8.79	nan	nan	7.501	nan	nan
HD182919	nan	5.596	5.594	nan	nan	5.613	nan	nan
HD183324	nan	5.876	5.793	nan	nan	5.525	nan	nan
HD18411	nan	4.754	4.685	nan	nan	4.418	nan	nan
HD184875	nan	5.404	5.348	nan	nan	5.045	nan	nan
HD18496	nan	10.13	9.08	nan	nan	6.653	nan	nan
HD184965	nan	8.93	8.55	8.293	8.046	7.503	nan	nan
HD185003	nan	9.83	9.75	nan	nan	9.23	nan	nan
HD185025	8.959	9.174	8.965	8.844	8.7	8.439	nan	nan
HD185297	nan	7.51	7.27	nan	nan	6.475	nan	nan
HD185378	nan	10.04	8.33	nan	nan	4.196	nan	nan
HD186408	nan	6.6	5.96	5.5	5.2	4.43	8.267	7.661
HD186427	nan	6.86	6.2	5.8	5.4	4.65	8.558	7.937
HD186440	nan	6.081	6.079	nan	nan	6.042	nan	nan
HD187350	7.53	8.2	8.14	nan	nan	7.41	8.27	8.153
HD188385	nan	6.179	6.139	nan	nan	5.995	nan	nan
HD188934	nan	11.6	9.3	nan	nan	4.97	nan	nan
HD191263	5.53	6.2	6.33	nan	nan	6.71	6.19	6.19
HD191639	5.42	6.288	6.445	nan	nan	6.947	nan	nan

Identifier	U	B	V	R	I	K	OH	NH
HD191854	nan	8.14	7.45	nan	nan	nan	9.755	9.128
HD192425	nan	5.013	4.947	nan	nan	4.767	nan	nan
HD192640	nan	5.096	4.955	nan	nan	4.422	nan	nan
HD193369	nan	5.626	5.573	nan	5.51	5.492	nan	nan
HD193702	nan	6.29	6.23	nan	nan	nan	nan	nan
HD196573	nan	9.54	7.9	nan	nan	3.825	nan	nan
HD19712	nan	7.32	7.35	nan	nan	7.41	8.215	8.11
HD197120	6.3	6.19	6.03	nan	5.87	5.451	nan	nan
HD197232	nan	9.516	9.092	nan	nan	8.02	nan	nan
HD198069	nan	5.6	5.612	nan	nan	5.449	nan	nan
HD199280	nan	6.488	6.562	nan	nan	6.718	nan	nan
HD20150	nan	4.874	4.88	nan	nan	4.825	nan	nan
HD204414	nan	5.435	5.389	nan	nan	5.29	nan	nan
HD205130	nan	7.78	7.85	nan	nan	8.02	8.375	8.314
HD205314	nan	5.734	5.766	nan	nan	5.788	nan	nan
HD205811	nan	6.212	6.178	nan	nan	6.112	nan	nan
HD206404	nan	8.12	7.68	nan	nan	6.418	nan	nan
HD206488	nan	9.3	8.83	nan	nan	7.712	nan	nan
HD206538	nan	6.143	6.08	nan	nan	5.831	nan	nan
HD206644	nan	5.784	5.733	nan	nan	5.544	nan	nan
HD207203	nan	5.641	5.631	nan	nan	5.479	nan	nan
HD207650	nan	5.08	5.071	nan	nan	5.07	nan	nan
HD208565	nan	5.589	5.544	nan	nan	5.359	nan	nan
HD209008	5.31	5.88	5.99	nan	nan	6.24	6.003	5.991

Identifier	U	B	V	R	I	K	OH	NH
HD210894	nan	10.54	9.17	nan	nan	6.131	nan	nan
HD211211	5.68	5.72	5.72	nan	nan	5.659	nan	nan
HD211287	nan	6.219	6.195	nan	nan	6.086	nan	nan
HD215044	nan	9.53	8.51	nan	nan	6.113	nan	nan
HD215093	nan	7.258	6.979	nan	nan	6.133	nan	nan
HD215110	nan	8.6	7.74	7.2	6.8	5.534	nan	nan
HD215141	12.577	10.724	9.239	8.439	7.718	5.734	nan	nan
HD216135	9.374	9.992	10.111	10.163	10.23	10.479	nan	nan
HD216735	nan	4.908	4.906	nan	nan	4.84	nan	nan
HD217014	nan	6.16	5.46	5	4.7	3.99	7.817	7.202
HD219188	nan	6.9	7.06	nan	nan	7.45	6.481	6.516
HD222133	nan	5.491	5.482	nan	nan	5.419	nan	nan
HD222732	nan	10.07	8.91	nan	nan	6.104	nan	nan
HD222733	nan	9.65	8.6	nan	nan	6.089	nan	nan
HD23258	nan	6.109	6.082	nan	nan	6.031	nan	nan
HD24401	10.229	10.157	10.01	9.931	9.836	9.559	nan	nan
HD24537	nan	9.21	8.77	nan	nan	7.494	nan	nan
HD24538	nan	10.04	9.58	nan	nan	8.267	nan	nan
HD24817	nan	6.145	6.082	nan	nan	5.925	nan	nan
HD25680	nan	6.52	5.9	5.5	5.2	4.38	8.063	7.495
HD26912	3.74	4.21	4.28	nan	nan	4.43	4.407	4.376
HD28099	nan	8.76	8.1	nan	nan	6.55	10.419	9.805
HD2892	12.096	10.682	9.36	8.668	8.039	6.218	nan	nan
HD290984	10.072	9.98	9.779	9.655	9.515	9.141	nan	nan

Identifier	U	B	V	R	I	K	OH	NH
HD290985	nan	9.83	9.26	nan	nan	7.805	nan	nan
HD292561	11.277	11.183	10.574	10.226	9.905	9.173	nan	nan
HD292574	10.851	10.739	10.537	10.427	10.306	9.946	nan	nan
HD292575	12.362	11.202	10.026	9.412	8.875	7.297	nan	nan
HD292582	nan	10.34	9.2	nan	nan	6.53	nan	nan
HD29461	nan	8.59	7.95	7.59	7.25	6.44	10.254	9.654
HD29526	nan	5.649	5.648	nan	nan	5.649	nan	nan
HD29646	nan	5.742	5.726	nan	nan	5.705	nan	nan
HD29722	nan	5.328	5.301	nan	nan	5.203	nan	nan
HD30246	nan	8.95	8.28	7.91	7.57	6.74	10.647	10.054
HD30739	nan	4.372	4.353	nan	nan	4.166	nan	nan
HD31073	nan	9.53	9.34	nan	nan	8.789	nan	nan
HD31295	nan	4.737	4.656	nan	nan	4.416	nan	nan
HD31331	nan	5.86	5.98	nan	nan	6.25	6.018	6.004
HD315	5.81	6.313	6.43	nan	nan	6.736	nan	nan
HD31647	nan	5.008	4.989	nan	nan	4.922	nan	nan
HD3379	5.06	5.73	5.86	nan	nan	6.28	5.65	5.673
HD36395	10.626	9.443	7.968	6.996	5.913	nan	nan	nan
HD36777	nan	5.388	5.332	nan	5.25	5.075	nan	nan
HD37112	nan	7.93	8	nan	nan	8.16	8.167	8.147
HD40588	6.36	6.28	6.19	nan	nan	5.887	nan	nan
HD43525	nan	5.499	5.399	nan	nan	5.109	nan	nan
HD46056	7.64	8.36	8.16	8.16	8.09	7.82	nan	nan
HD46553	nan	5.257	5.266	nan	nan	5.147	nan	nan

Identifier	U	B	V	R	I	K	OH	NH
HD47575	nan	6.048	5.979	nan	nan	5.74	nan	nan
HD47761	8.22	8.83	8.72	nan	nan	8.233	nan	nan
HD48097	nan	5.27	5.21	nan	nan	5.011	nan	nan
HD49908	nan	5.275	5.265	nan	nan	5.165	nan	nan
HD50167	nan	9.52	7.88	nan	nan	4.413	nan	nan
HD50188	9.436	9.535	9.538	9.528	9.521	9.452	nan	nan
HD50209	8.05	8.37	8.36	nan	nan	7.997	nan	nan
HD50973	nan	4.935	4.9	nan	nan	4.793	6.838	6.85
HD52266	6.32	7.22	7.23	nan	nan	7.27	nan	nan
HD52533	6.66	7.57	7.68	nan	nan	7.936	nan	nan
HD5267	5.62	5.76	5.79	nan	nan	5.796	nan	nan
HD5319	nan	9.03	8.05	nan	nan	5.699	nan	nan
HD5505	nan	10.18	9	nan	nan	6.487	nan	nan
HD55111	nan	6.053	6.072	nan	nan	6.004	nan	nan
HD57744	6.17	6.17	6.17	nan	nan	6.163	nan	nan
HD5788	5.62	5.68	5.69	nan	nan	6.784	nan	nan
HD57884	nan	11.7	9	nan	nan	3.774	nan	nan
HD60107	nan	5.32	5.269	nan	nan	4.995	nan	nan
HD60357	nan	5.811	5.83	nan	nan	5.738	nan	nan
HD60826	nan	11.7	8.9	nan	nan	3.091	nan	nan
HD61219	6.24	6.2	6.18	nan	nan	6.081	nan	nan
HD61887	nan	5.923	5.955	nan	nan	5.918	nan	nan
HD6456	5.26	5.319	5.317	nan	nan	5.265	nan	nan
HD6457	nan	5.484	5.532	nan	nan	5.61	nan	nan

Identifier	U	B	V	R	I	K	OH	NH
HD64633	nan	9.66	8.41	nan	nan	5.765	nan	nan
HD64652	nan	9.49	8.36	nan	nan	5.777	nan	nan
HD64747	nan	9.49	9.43	nan	nan	9.491	nan	nan
HD64854	8.512	9.243	9.398	9.457	9.539	9.846	nan	nan
HD64887	9.131	9.351	9.419	9.45	9.492	9.6	nan	nan
HD66664	nan	5.162	5.146	nan	nan	5.099	nan	nan
HD68099	5.54	5.97	6.08	nan	nan	6.35	6.366	6.325
HD6815	nan	7.25	7.3	nan	nan	7.47	7.935	7.869
HD72055	nan	8	8.12	nan	nan	8.307	nan	nan
HD72524	nan	5.803	5.755	nan	nan	5.544	nan	nan
HD72526	nan	7.94	7.93	nan	nan	7.86	9.004	8.879
HD74280	3.38	4.1	4.3	nan	nan	4.8	3.934	3.963
HD75137	nan	4.327	4.343	nan	nan	4.36	nan	nan
HD75914	nan	8.72	8.65	nan	nan	8.517	nan	nan
HD76082	nan	9.53	8.42	nan	nan	5.839	nan	nan
HD76151	nan	6.67	6	nan	nan	4.46	8.339	7.717
HD76242	nan	9.72	8.9	nan	nan	6.893	nan	nan
HD77104	6.03	5.94	5.87	nan	nan	5.718	nan	nan
HD79097	nan	9.23	7.62	nan	nan	3	nan	nan
HD79108	nan	6.135	6.137	nan	nan	6.119	nan	nan
HD81809	nan	6.02	5.4	nan	nan	3.57	7.671	7.063
HD84971	7.76	8.48	8.64	nan	nan	9.082	nan	nan
HD85990	nan	9.1	7.99	nan	nan	5.404	nan	nan
HD86135	nan	9.36	7.88	nan	nan	4.29	nan	nan

Identifier	U	B	V	R	I	K	OH	NH
HD86408	10.266	10.135	9.874	9.728	9.577	9.199	nan	nan
HD88960	nan	5.509	5.49	nan	nan	5.387	nan	nan
HD89688	5.9	6.54	6.64	nan	nan	6.93	6.592	6.563
HD90470	nan	6.152	6.014	nan	nan	5.532	nan	nan
HD91365	5.64	5.61	5.58	nan	nan	5.348	nan	nan
HD93702	nan	5.348	5.314	nan	nan	5.075	nan	nan
HD94516	nan	10.28	9.22	nan	nan	6.735	nan	nan
HD94538	nan	9.77	8.74	nan	nan	6.393	nan	nan
HD94601	nan	4.51	4.5	nan	nan	nan	nan	nan
HD94603	nan	9.43	9.35	9.31	9.651	9.277	nan	nan
HD94616	nan	9.41	8.91	nan	nan	7.554	nan	nan
HD94808	nan	8.21	7.92	nan	nan	7.162	nan	nan
HD97859	8.695	9.238	9.352	9.387	9.441	9.621	nan	nan
HD97991	6.28	7.18	7.39	nan	nan	8.08	6.718	6.779
HD99787	nan	5.373	5.354	nan	nan	5.307	nan	nan
HIP107968	11.942	12.732	12.743	12.839	12.938	13.397	nan	nan
HIP12031	11.027	12.209	12.412	12.325	11.968	10.557	nan	nan
HIP13800	9.572	10.193	10.304	10.352	10.412	10.635	nan	nan
HIP22591	nan	9.99	8.98	nan	nan	6.463	nan	nan
HIP3013	9.848	10.686	10.885	10.98	11.089	11.453	nan	nan
HIP33837	nan	9.2	8.71	nan	nan	6.943	nan	nan
HIP3678	10.15	11.43	11.78	nan	nan	nan	nan	nan
HIP53383	12.172	11.154	10.074	9.429	8.905	7.508	nan	nan
HIP57058	12.012	10.818	9.585	8.802	8.133	6.425	nan	nan

Identifier	U	B	V	R	I	K	OH	NH
HIP66673	11.601	11.832	11.451	11.184	10.892	10.208	nan	nan
HIP66872	9.504	10.206	10.369	10.441	10.537	10.865	nan	nan
HIP8952	nan	10.18	9.44	nan	nan	7.292	nan	nan
MGC37338	nan	13.1	nan	nan	nan	nan	nan	nan
MGC66878	nan	12.77	nan	nan	nan	nan	nan	nan
SA92-	nan	nan	nan	nan	nan	nan	nan	nan
SA94-149	nan	15.45	14.06	nan	nan	nan	nan	nan
SA94-276	nan	13.72	12.89	nan	nan	nan	nan	nan
SA94-317	nan	13.45	12.68	nan	nan	nan	nan	nan
SA94-407	nan	13.18	12.32	nan	nan	nan	nan	nan
SA94-444	nan	14.51	13.69	nan	nan	nan	nan	nan
SA94-574	nan	14.13	13.16	nan	nan	nan	nan	nan
SA94-580	nan	14.95	13.31	nan	nan	nan	nan	nan
SA94-599	nan	15.13	14.34	nan	nan	nan	nan	nan
TYC117-895-1	12.481	12.382	11.735	11.366	11.01	10.11	nan	nan
TYC12-1097-1	12.957	12.485	11.63	11.141	10.699	9.536	nan	nan
TYC12-214-1	12.007	12.05	11.615	11.35	11.078	10.453	nan	nan
TYC30-108-1	13.278	12.842	12.009	11.54	11.117	10.07	nan	nan
TYC30-78-1	11.981	12.034	11.546	11.253	10.954	10.261	nan	nan
TYC30-820-1	13.631	12.702	11.619	11.066	10.563	9.128	nan	nan
TYC350-676-1	14.285	12.535	10.939	9.797	8.365	5.558	nan	nan
TYC351-60-1	12.757	12.479	11.713	11.271	10.85	9.772	nan	nan
TYC447-527-1	13.212	12.529	11.583	11.034	10.408	9.148	nan	nan
TYC447-98-1	11.788	11.678	11.122	10.797	10.462	9.769	nan	nan

Identifier	U	B	V	R	I	K	OH	NH
TYC4688-87-1	12.41	12.397	12.405	12.412	12.409	12.361	nan	nan
TYC4718-375-1	13.343	12.657	11.531	10.931	10.366	8.815	nan	nan
TYC4736-1132-1	10.954	10.836	10.589	10.456	10.318	10.099	nan	nan
TYC4737-114-1	nan	11.93	11.03	nan	nan	nan	nan	nan
TYC4737-23-1	12.105	11.9	11.719	11.627	11.53	11.245	nan	nan
TYC478-1348-1	14.511	12.489	10.748	9.783	8.885	6.401	nan	nan
TYC4833-591-1	nan	11.46	11.19	nan	nan	nan	nan	nan
TYC4833-626-1	nan	13.81	10.79	nan	nan	nan	nan	nan
TYC4865-384-1	12.291	12.292	11.799	11.504	11.211	10.569	nan	nan
TYC4896-1223-1	12.806	12.388	11.576	11.123	10.712	9.628	nan	nan
TYC4914-700-1	nan	11.14	10.09	nan	nan	nan	nan	nan
TYC4932-246-1	nan	12.02	11.16	nan	nan	nan	nan	nan
TYC4949-1017-1	13.637	12.586	11.478	10.811	10.264	8.848	nan	nan
TYC4949-865-1	nan	12.02	11.22	nan	nan	nan	nan	nan
TYC5048-662-1	nan	12.65	11.01	nan	nan	nan	nan	nan
TYC5081-142-1	12.657	12.435	11.731	11.304	10.869	9.912	nan	nan
TYC5081-2166-1	11.97	11.816	11.49	11.303	11.081	10.698	nan	nan
TYC511-1680-1	14.944	12.953	11.352	10.454	9.551	7.296	nan	nan
TYC511-1749-1	13.461	12.578	11.548	10.99	10.488	9.086	nan	nan
TYC511-2229-1	11.888	11.878	11.424	11.151	10.877	10.212	nan	nan
TYC543-1357-1	14.163	12.943	11.744	11.123	10.577	8.994	nan	nan
TYC568-1069-1	11.512	11.879	11.916	11.889	11.906	12.055	nan	nan
TYC568-1298-1	14.529	12.961	11.601	10.863	10.214	8.378	nan	nan
TYC568-1417-1	13.53	12.307	11.101	10.456	9.893	8.279	nan	nan

Identifier	U	B	V	R	I	K	OH	NH
TYC586-717-1	11.602	11.627	11.16	10.872	10.579	9.927	nan	nan
TYC66-839-1	12.392	12.224	11.487	11.068	10.656	9.624	nan	nan
TYC66-860-1	12.823	12.512	12.067	11.804	11.521	10.817	nan	nan
V*IPVir	12.016	11.931	11.599	11.403	11.209	10.769	nan	nan
AKS95 116	nan	9.059	8.442	nan	nan	nan	nan	nan
AKS95 125	nan	8.064	7.524	nan	nan	nan	nan	nan
GTJ2000 5-162	nan	nan	18.982	nan	nan	nan	nan	nan

Identifier	UVc	CN	C3	CO+	Bc	C2	Gc	H2O+	Rc
HD11131	8.207	8.068	7.692	7.537	7.22	6.802	6.724	5.981	5.96
HD120086	7.46	7.619	7.664	7.669	7.68	7.698	7.702	7.764	7.766
HD129956	6.476	5.808	5.652	5.612	5.573	5.546	5.544	5.44	5.431
HD146233	7.048	6.972	6.465	6.313	5.98	5.558	5.476	4.732	4.708
HD149363	7.504	7.748	7.858	7.822	7.784	7.658	7.638	7.474	7.448
HD14951	5.594	5.411	5.364	5.358	5.344	5.344	5.346	5.324	5.327
HD154445	5.708	5.813	5.841	5.791	5.754	5.556	5.52	5.203	5.191
HD164852	5.188	5.166	5.149	5.144	5.133	5.144	5.108	5.052	5.054
HD170783	8.428	8.029	7.979	7.925	7.861	7.656	7.624	7.303	7.285
HD186408	7.565	7.463	6.946	6.792	6.459	6.039	5.957	5.217	5.191
HD186427	7.842	7.783	7.225	7.075	6.725	6.302	6.214	5.476	5.441
HD187350	8.11	8.252	8.317	8.278	8.241	8.078	8.037	7.72	7.703
HD191263	6.19	6.19	6.19	6.19	6.19	6.19	6.19	6.19	6.19
HD191854	9.026	8.963	8.413	8.272	7.909	7.486	7.394	6.642	6.614

Identifier	UVc	CN	C3	CO+	Bc	C2	Gc	H2O+	Rc
HD19712	8.039	7.505	7.321	7.283	7.208	7.228	7.248	7.133	7.135
HD205130	8.286	7.868	7.799	7.78	7.752	7.742	7.74	7.682	7.684
HD209008	5.981	5.872	5.876	5.876	5.862	5.85	5.848	5.813	5.815
HD217014	7.117	7.075	6.454	6.291	5.943	5.523	5.434	4.683	4.668
HD219188	6.514	6.82	6.956	6.947	6.932	6.917	6.909	6.885	6.884
HD25680	7.406	7.305	6.859	6.704	6.377	5.96	5.883	5.152	5.13
HD26912	4.357	4.239	4.231	4.224	4.204	4.155	4.145	nan	nan
HD28099	9.736	9.673	9.113	8.944	8.603	8.173	8.09	7.338	7.312
HD29461	9.579	9.503	8.957	8.787	8.451	8.03	7.945	7.205	7.17
HD30246	9.976	9.924	9.362	9.197	8.847	8.411	8.323	7.561	7.527
HD31331	6.003	5.875	5.856	5.848	5.838	5.837	5.836	5.807	5.81
HD3379	5.68	5.716	5.714	5.713	5.717	5.728	5.727	5.749	5.748
HD37112	8.134	7.976	7.914	7.899	7.881	7.867	7.863	7.814	7.803
HD50973	6.833	7.129	7.246	7.219	7.195	7.093	7.073	6.933	6.917
HD68099	6.297	5.986	5.948	5.947	5.921	5.931	5.931	5.898	5.901
HD6815	7.838	7.383	7.233	7.205	7.172	7.173	7.167	7.119	7.124
HD72526	8.821	8.121	7.913	7.87	7.822	7.796	7.793	7.689	7.679
HD74280	3.967	4.047	4.078	4.093	4.09	4.125	4.131	nan	nan
HD76151	7.63	7.614	7.012	6.847	6.501	6.074	5.983	5.236	5.212
HD81809	6.889	6.767	6.316	6.187	5.866	5.432	5.346	4.587	4.559
HD89688	6.556	6.532	6.577	6.567	6.556	6.515	6.507	6.463	6.463
HD97991	6.796	7.081	7.164	7.173	7.186	7.225	7.23	7.317	7.311